ABSTRACT

Application of Direct Current Resistivity Method to Environmental and Hydrological Problems

Tian Xu, Ph.D.

Committee Chair: John A. Dunbar, Ph.D.

The direct current resistivity (DCR) method is a well-established geophysical method that is widely used in environmental, civil engineering, and hydrological investigations. DCR has the advantage of producing spatial and temporal images of the subsurface in two and three dimensions at relatively high resolution compared to those produced by other electrical methods. In the past few decades, DCR method has been applied in a variety of "conventional" near surface land and marine environments.

This dissertation addresses approaches to expanding the utility of DCR in conventional environments and to applying it in three different unconventional and challenging environments. Following an introduction to the research in chapter one, results of a binning method applied to continuous resistivity profiling data in water reservoirs are presented in chapter two. Results reveal that the method is computationally efficient and suitable for lacustrine environments. In chapter three, the application of the DCR method on a deep-marine, near-bottom environment is evaluated. This study shows that it is possible to collect valid DCR data in deep-marine settings to detect shallow

resistivity anomalies and to map their distribution within 100 m of the seafloor. In chapter four, an application of a time-lapse azimuthal DCR method to monitor bedrock joints and soil cracking on a vertisol-shale terrain is evaluated. It is demonstrated that vertical profiles of anisotropy have the potential to quantify the density and orientation of both soil cracks and bedrock joints. Chapter five presents a brief summary and conclusions of the research.

Application of Direct Current Resistivity Method to Environmental and Hydrological Problems

by

Tian Xu, B.S.

A Dissertation

Approved by the Department of Geosciences

_____

Stacy C. Atchley, Ph.D., Chairperson

Submitted to the Graduate Faculty of
Baylor University in Partial Fulfillment of the
Requirements for the Degree
of

Doctor of Philosophy

Approved by the Dissertation Committee

_____

John A. Dunbar, Ph.D., Chairperson

_____

Peter M. Allen, Ph.D.

_____

Robert J. Pulliam, Ph.D.

_____

Joe C. Yelderman, Ph.D.

_____

Ronald Morgan, Ph.D.

Accepted by the Graduate School

May 2016

_____

J. Larry Lyon, Ph.D., Dean

*Page bearing signatures is kept on file in the Graduate School.*

TABLE OF CONTENTS

LIST OF FIGURES

LIST OF TABLES

Table Page

# ACKNOWLEDGMENTS

First, I would like to thank my parents, Youhai Xu and Wei Cheng for all the love, guidance and financial support throughout my entire college career in United States. Eight year ago, when I reached the lowest point of my life, they helped me get through and encourage me to pursue my dream in USA. Their patient and encouragement push me farther than I thought I could achieve.

I would also like to express my sincere gratitude to my advisor Dr. John A. Dunbar, who has been supportive since the first day I began studying in Baylor in the summer of 2012. The four-year invaluable research and field work experience I had with him help me to achieve my long-term career goals. The journey I have taken in these past four years has changed my life and I have experienced nothing but positive times.

My sincere thanks also go to Dr. Peter Allen who provided me opportunities to participate different researches and gave me access to the laboratory facilities. I am indebted to Dr. Jay Pulliam, who has been a constant source of knowledge and inspiration in past four years. I would like to also thank the rest of my committee, Dr. Joe Yelderman and Dr. Ron Morgan, for the time, effort and insightful comments they put into my research project.

Finally, and most importantly, I would like to extend my gratitude to my wife Zheng, who always offers unwavering support and encouragement. To my beloved son Adam, I would also like to express my thanks for being such a good boy in past three years.

# DEDICATION

To my parents, Youhai Xu and Wei Cheng,

Your encouragement and support enable me to pursue and finish this research

And

To my wife Zheng Wang and my son Adam Xu

Your unyielding love enriched my soul

# CHAPTER ONE

## Introduction

The direct current resistivity (DCR) method is a well-established geophysical method that is widely used in environmental, civil engineering, and hydrological investigations. DCR has the advantage of producing relatively high resolution spatial and temporal images of the subsurface in two- and three-dimensions at various scales compared to those produced by other electrical methods. The goal of the DCR is to measure the Earth's voltage response to near-DC electrical current and then image the distribution of subsurface resistivity in both lateral and vertical directions. The DCR method involves the injection of artificially-generated, near direct current (DC) between two current electrodes and the simultaneous measurement of the electric potential between two or more pairs of receiver electrodes. Rather than true DC source currents, low frequency square wave currents are used, in order to avoid the generation of polarized ionization fields near the electrodes and to cancel noise due to telluric currents.

In the past few decades, DCR method has been applied for different "conventional" near surface land and marine environment for environmental and hydrological studies. This dissertation address approaches for expand the utility of DCR to different "unconventional" and challenging environments. In chapter two, a binning method is developed to solve a challenging problem that building 3D inverted resistivity models for shallow marine environment. As an emerging DCR method, continuous resistivity profiling (CRP) is widely used to image the resistivity distribution of riverine,

lacustrine and marine environments to explore a relative large survey area. However, it is generally not possible to precisely control the spacing and orientation of profiles during CRP data acquisition, resulting in irregularly distributed data. Three dimensional inversion of CRP data set is challenging since most commercial inversion codes require data on a regular grid. Therefore, most inverted models for shallow aquatic environment are limited to 2D. In this chapter, we develop a technique for binning irregularly distributed 2D CRP data onto a regular grid, making the binned data sets suitable for most commercial 3D inversion codes. We evaluate the method on synthetic data sets, as well as field CRP data sets collected from two water reservoirs on Maui Island, Hawaii. The results of numerical modeling demonstrate the binning method can be a practical and useful method for converting densely spaced 2D CRP profiles into a 3D survey. The 3D inverted resistivity volumes of the binned field CRP data sets also show good agreement with independently collected 2D profiles, resolving the same subsurface features. This chapter has been published in *Journal of Environmental and Engineering Geophysics* (Xu and Dunbar, 2015)

In the third chapter, the application of conventional near surface shallow water DCR method is extended to unconventional deep-marine, near-bottom environment. A conventional engineering-scale DCR survey system is adapted to characterize shallow gas-hydrate deposits beneath Woolsey Mound, Mississippi Canyon Block 118 (MC118), Gulf of Mexico. The objective of the study is to: (1) explore the possibility of the DCR method to collect valid data on the deep-marine environment and detect shallow resistivity anomalies, (2) characterize the shallow gas-hydrate distribution at the study site and monitor changes in the distribution over time. The results from Woolsey Mounds

demonstrate that the seafloor DCR method provides valid data to image resistivity anomalies and characterize the distribution of shallow gas hydrate. The time-lapse resistivity survey also proves that it can be an effective tool for long-term near-bottom sediment monitoring. This chapter has been published in *The Leading edge* (Xu et al., 2015)

The fourth chapter explores the potential of using the DCR method to evaluate the bedrock fracture and soil cracking on a Vertisol-shale terrain. Cracks within Vertisols soils and joints in underlying bedrock play a crucial role in the water budget of Vertisols-shale terrains. Subvertical joint sets within the bedrock with preferred orientation also result in an anisotropic distribution of electrical resistivity. Cracked soil, on the other hand, exhibits the anisotropy as well as heterogeneous electrical resistivity. Better knowledge of seasonal soil cracking as well as the joints within the bedrock allow better estimates of runoff, storage and recharge, and better agricultural and engineering practices in the expensive soil terrains. This study demonstrates that surface azimuthal resistivity surveys are an efficient method for quantifying shallow bedrock joints and for monitoring seasonal change in soil cracking. A positive relationship between the measured crack volume and the coefficient of anisotropy in the soil layer area is observed during drying and wetting periods. Corroborating information for existence and vertical extent of soil cracks is provided by the homogeneity index, which has previously been used only as an indicator of azimuthal resistivity data quality. This indicates the potential of using azimuthal DC resistivity surveys to quantify the soil crack volume. This work is currently in review in Vadose Zone Journal (Xu et al., in review).

# CHAPTER TWO

## Binning Method for Mapping Irregularly Distributed Continuous Resistivity Profiling Data onto a Regular Grid for 3-D Inversion

This chapter published as: Xu, T., & Dunbar, J. A. (2015). Binning Method for Mapping Irregularly Distributed Continuous Resistivity Profiling Data onto a Regular Grid for 3-D Inversion. *Journal of Environmental and Engineering Geophysics*, *20*(1), 1-17.

*Abstract*

Continuous resistivity profiling (CRP) is an emerging direct current (DC) resistivity method that is increasingly used in shallow fresh water and marine environments to support hydrogeological and near surface geophysical studies. CRP is popular, because it allows efficient data acquisition. However, it is generally not possible to precisely control the spacing and orientation of profiles during CRP data acquisition, resulting in irregularly distributed data. For 2D profiles, the irregular distribution is handled by extracting relatively straight segments for inversion and using either interpolation or irregular element widths in the inversion process to account for uneven data spacing along the profiles. 3D inversion of CRP data sets is more challenging, because most commercial inversion codes are applicable only to parallel or sub-parallel survey lines, requiring data on a regular grid. In this research, we develop a technique for binning irregularly distributed CRP data onto a regular grid, suitable for most 3D inversion codes. The method uses the GPS track line of the survey vessel as the assumed path of the electrode array to reconstruct the electrode locations through time during the survey. Individual apparent resistivity readings are assigned geographic locations at the center of each four-electrode array configuration. Apparent resistivity of like-array

configurations within a spatial bin around a grid point is then interpolated to the center of the bin. The interpolation is repeated for each grid point and each array configuration. Finally, a set of binned readings is generated with each array configuration centered at the regular grid points and written to a standard input file type for a commercial 3D inversion code. We evaluate the method on synthetic data sets as well as field CRP data sets collected from two water reservoirs on Maui Island, Hawaii. Numerical results of the synthetic data inversion show that 20% and 10% model misfit between a "control group" and binned data can be achieved with data densities of 5 and 15 measurements in each bin, respectively. Also, the 3D inverted resistivity volumes of the binned field CRP data sets show good agreement with independently collected 2D profiles, resolving the same subsurface features.

## *Introduction*

Continuous resistivity profiling (CRP) is a DC resistivity data acquisition technique that is widely used by hydrologists and environmental geophysicists to image the resistivity distribution in riverine, lacustrine and marine environments (Day-Lewis et al, 2006). Instruments that collect data in the CRP mode have been commercially available since the 1990s and have become popular since the method lends itself to rapid data acquisition and dense data coverage. Recently, the CRP technique has been carried out for the investigation of coastal submarine ground-water discharge, characterization of aquifers, determination of canal leakage potential and the study of seasonal salinity variations (Snyder and Wightman, 2002; Belaval et al, 2003; Ball et al, 2006; Dunbar et al, 2008).

The instruments used in CRP are normally modified forms of conventional land-based resistivity survey instruments. They consist of a multi-channel resistivity meter and multiple electrodes mounted on a streamer, combined with a GPS navigation system. Rather than connecting the electrodes to conducting metal stakes as in land-based resistivity surveys, the streamer with floats spaced along its length is towed behind a survey vessel to make measurements. Every few seconds, the resistivity data are acquired by simultaneously measuring the potential between electrodes in response to direct current injected into the water, while pulling the array continuously through the water and recording the geographic position of the survey vessel using the GPS navigation system. The CRP technique makes it possible to collect resistivity data at least an order of magnitude faster than in land-based surveying. However, in contrast to land-based surveying, it is impracticable to precisely control profile spacing and orientation during CRP data acquisition due to the water movement, wind, wave action and survey vessel navigation errors, resulting in non-parallel survey lines and irregularly distributed data points. For 2D CRP surveys, the off-line data on the profile can be processed by extracting relatively straight segments, stacking closely-spaced measurements before inversion and using either interpolation or irregular element widths in the inversion process to account for uneven data spacing along the profile. 3D inversion of CRP data sets is more challenging since most current commercial resistivity inversion programs are applicable only to parallel or sub-parallel survey lines, requiring data on a regular grid. This compounds the difficulties of both acquiring and inverting 3D CRP data in the conventional way. Previously proposed methods of treating this problem include nudging irregularly distributed 2D CRP data to orthogonal cross-lines and building quasi

3D models by interpolating sub-parallel 2D lines (Rucker et al., 2009, 2011; Dahlin and Loke, 1997).

In this paper, we develop a technique for binning irregularly distributed 2D CRP data onto a regular grid, making the binned data sets suitable for most commercial 3D inversion codes. The technique of binning can convert a series of closely spaced 2D CRP profiles into a quasi-3D CRP survey, collected in various aquatic environments through binning scattered data points onto regular grids and then conducting 3D inversion and interpretation. The technique of binning has traditionally been applied to marine 3D seismic surveys (Xu et al., 2005). For 3D seismic surveys, the survey area is divided into multiple rectangular horizontal zones called ‘bins’ on the surface and each seismic trace is assigned to a bin according to the midpoint between the source and the receiver. Seismic traces within bins are successively combined to generate the output traces at the bin nodes at the centers of the bins, to form a regular grid. The grid of bin nodes can be generated on a Cartesian coordinate system, such as Universal Transverse Mercator coordinate system (UTM) (Fomel, 2001).

Apparent resistivity measurements obtained from DC resistivity surveys tend to be spatially smooth, because they represent a weighted average resistivity over large, overlapping volumes. As is the case with potential field measurements, nearby subsurface properties contribute more to the average than the properties further away. Gridding methods are commonly used to generate maps from irregularly spaced gravity and magnetic field measurements (e.g., Lam, 1983; Guo, 2012). For example, the minimum surface curvature method (Briggs, 1974), has been a popular algorithm for potential field data gridding for years. However, the results are degraded when dealing with the sparse

data sets with spacing larger than the grid spacing (Li and Gotze 1999). The equivalent source method (Dampney, 1969; Cordell, 1992) generates grids from two-dimensional data similarly but with less aliasing; however it requires the solution of a large-scale linear system. Kriging is another data gridding algorithm developed by Matheron (1971) based on the paper of Krige (1951); however, it can be computationally expensive and requires fitting a variogram interactively. An appropriate interpolation method for CRP data needs to be accurate, flexible, and computationally efficient, since the number of the data points in CRP surveys can be fairly large. In this paper, we propose a so called "binning" method similar to the binning technique used in 3D seismic surveying. This key distinction between the binning process and gridding processes is that in binning grid values are estimated based only on measurements that fall within a rectangular bin surround the grid point and those measurements do not factor into the estimation of neighboring grid points. Gridding usually involves a degree of overlap in the data used to estimate neighboring grid points.

The binning technique we propose for 3D inversion of CRP data in this paper can be regarded as an analogy of the 3D seismic data binning. Since the DC resistivity and seismic data have in common that both data types are generated using discrete source and receiver locations at different offsets and the resulting measurements are dominated by the subsurface properties between the two. The 3D seismic binning method involves sorting traces based on the locations of the middle points between their sources and receivers into rectangular grid cells (bins). In the analogous DC resistivity binning technique, resistivity measurements are sorted into bins based on the center points of each four-electrode array configuration used to make each measurement.

In this study, we evaluate the proposed binning technique by applying the method to synthetic data sets and field CRP data sets. After the irregularly distributed data are converted to data on regular grids, 3D inversions are conducted for both the synthetic data and field data examples. To demonstrate the efficiency of the method on synthetic data, we also generate synthetic data sets that are already on regular grids, rather than scattered data sets, to simulate a conventional 3D survey to function as a "control" case. After inverting the synthetic data sets, we first compute the root-mean-squared (RMS) error between the input apparent-resistivity data and the resistivity values predicted from the inverted model. Next we compare the inverted model misfit with the results from the scattered synthetic data sets and the control case.

The binning method is also validated using a case study in two agricultural reservoirs on Maui Island, Hawaii, the goal of which was to identify isolated leakage pathways through the reservoir bottoms. As well as collecting CRP data sets for the two reservoirs, fixed 2D DC resistivity profiles across reservoirs are also collected. After obtaining the 3D inversion results, we extract 2D profiles from the 3D resistivity volumes to compare to the inversions of independently acquired 2D profiles along the same lines.

### *Methodology*

The proposed method of processing the CRP data consists of 1) filtering the original CRP data to remove bad readings, 2) converting GPS latitude and longitude data to Universal Transverse Mercator (UTM) coordinates and combining the filtered CRP data with the survey vessel geographic position, 3) tracking backward from the vessel position to find the position of the electrodes during the survey, 4) dividing the data into subgroups based on their array type and electrode separation, 5) applying straight-array

filtering to reject non-linear array configurations for all the subgroups and calculating the geographic centers of all the arrays, 6) sorting the readings into the geographic bins in which the array center points fall and interpolating the points within each bin to the center of the bin independently for each array subgroup for all the subgroups, 7) generating virtual locations for the electrodes of all the array subgroups, and combining all the subgroups to create a standard resistivity file that can be read by commercial 3D inversion code. After these steps, the binned data set is ready to be inverted using a commercial 3D inversion code. In principle, it would be possible to perform each step above separately, in a step-by-step mode. However, this would be time consuming and cumbersome. One of the goals of this study is to produce an automated approach that integrates all of the steps into one program to process the original data files into a formatted and ready-to-inverse data file, streamlining the procedures to one operation.

Initial data filtering and editing is applied to the raw CRP data to remove bad measurements. In addition to the normal sources of error in making DC resistivity measurements, marine CRP measurement are subject to error due to: 1) off-line electrode movement induced by shifting wind direction and boat navigation, 2) variable near-electrode resistance due to the formation of cavitation bubbles and vegetation entrainment (Day-Lewis, 2006), 3) invalid readings as a result of one or more electrodes breaking electrical contact with the water during a reading due to wave action (Dunbar et al., 2008). Therefore, initial data filtering is necessary to remove outlier values from measured apparent resistivity data.

During the survey, the GPS on the survey vessel creates a file containing geographic locations in terms of longitude and latitude versus time of day. To apply the

binning method, the longitude and latitude need to be converted to position on a Cartesian map coordinate system. One of the most widely used map projection is UTM system, which we used in this study. After the geographic location information conversion is accomplished, the navigation information is merged with the filtered CRP data by matching the time-of-day entries in both data sets. Thus the position of the GPS antenna on the survey vessel at the time of each reading along the survey track can be assigned UTM coordinates in terms of each measurement time. We assume that the electrodes along the streamer cable follow the curved path of the survey vessel throughout the survey, under gentle maneuvering (Snyder, 2002). Therefore, using the UTM coordinate of the GPS antenna and the geometry of electrode array, the geographic location of each electrode can be computed by finding each electrode offset along the vessel track at the time each reading is made.

Most modern DC resistivity instruments take advantage of multichannel capability to make multiple simultaneous measurements with different depth of investigation. Figure 2.1 shows a schematic of the towed resistivity streamer cable and the arrangement of electrodes behind a boat. The inter-electrode spacing (distance between current electrode pair and potential electrode pair) increases by a factor n to obtain a good 2D image of subsurface. Since the center and the depth of investigation (as a function of n) of the electrode array are different for those simultaneous measurements, we have to apply the binning method to readings with different depth of investigation separately. Therefore the readings are sorted into n subgroups and the UTM locations for the centers of electrode arrays in each of subgroups are calculated.

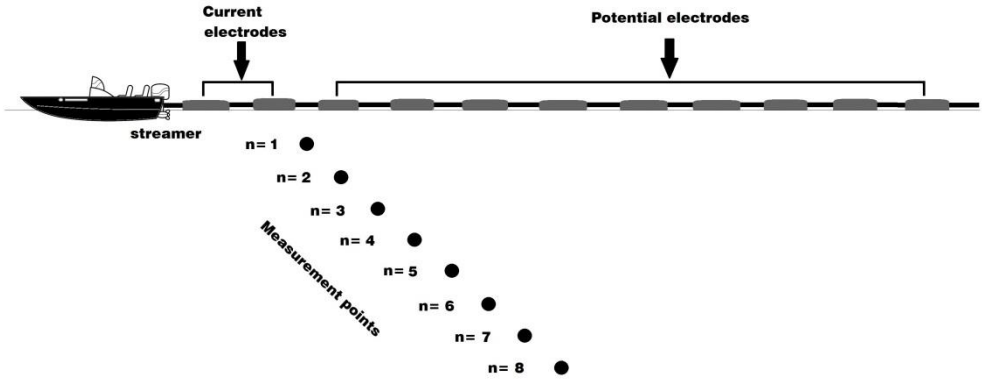


Figure 2.1 Schematic diagram showing data acquisition of a CRP survey with 11-electrode streamer, assuming a dipole-dipole configuration. First two electrodes serve as current electrode and the rest serve as potential electrodes, with the increasing inter-electrode spacing as a factor of n. The multichannel resistivity meter collects multiple measurements with different depth of investigation simultaneously.

Since our intent is to interpolate resistivity readings made with similar electrode configurations, we filter the non-linear array geometries by computing the intersection angle between the line segment between the two potential electrodes and the line segment between two current electrodes.

Measurements having intersection angles larger than 5 degrees are removed at this stage so that bad readings made during turns and off-line readings are filtered. In order to bin the distributed CRP data efficiently, we choose to interpolate the data points using the inverse-distance weighted method (IDW). The inverse-distance weighted method is versatile, easy to program and widely used by earth scientists (e.g., Bartier, 1996; Tomczak, 1998). The basic form for inverse distance weighted interpolation is Shepard's method (Shepard, 1968), and the general equation is given by:

$$Z_{x,y} = \frac{\sum_{i=1}^{n}\left(\frac{z_i}{D_i^{\alpha}}\right)}{\sum_{i=1}^{n}\left(\frac{1}{D_i^{\alpha}}\right)} \qquad (2.1)$$

The $Z_{x,y}$ is the estimated value of interpolant at node *(x, y)*; $z_i$ is *i*th of *n* control points within the bin to be interpolated; $D_i$ is the distance from *i*th control point to the location *(x, y)*; $\alpha$ is the power parameter defined by the user.

Equation (2.1) means that the points closer to the node have more influence on the interpolated value than more distance points based on the inverse of distance to a power. When α is set equal to zero, the method is identical to the simple average of the control points, taking no account for distance. As α becomes larger, the weights applied to neighboring point weights become greater relative to more distant points (Watson and Philip, 1985). The inverse distance weighted method can be local or global. Global method utilizes all the scattered point to estimate the value on node. The local method is based on the assumption that each point can influence the value on node only to a certain distance (Mitas and Mitasova, 1999). Our binning method is a subset of the local method for which there is no overlap between data contributing to the estimation of the values of adjacent nodes. For the choice of the value for the power parameter, one can consider the density and distribution of data points, the maximum distance of points allowed to influence the interpolated value, and the degree of smoothing desired. To deal with densely distributed CRP data for large areas, more influence on global data points may distort the result. Hence, in this paper, we restrict influence to the data points within the local bin and only use data within the bin to estimate the value at the bin center. The weighting parameter α is chosen to be 2 in this study.

The CRP readings are assigned to rectangular bins on a 2D surface based on the UTM coordinates of the center point of the four electrode array when the measurement was made. The bin size is selected, giving consideration to the data density, the required resolution of the 3D inversion, and the time required to complete the resulting 3D inversion. The length of a bin's side is designed to be proportional to the data density in that dimension. The size of a bin must be an even multiple of the minimum inter-electrode spacing (when n=1) so that virtual electrode locations can fall on grid nodes. For this study, since the data points are almost equally distributed on x and y direction, a square-shape bin with sides equal to twice the minimum inter-electrode spacing was chosen as the best compromise.

Apparent resistivity of measurements within each bin is then interpolated to the grid point location at the center of the bin. After the interpolation is applied, the scattered data sets are converted to regularly distributed data sets on a rectangular grid. Then to convert these values into a form useable by most 3D inversion codes, the locations of virtual electrodes for each subgroup are generated based on their original array type and electrode separation, centered at the each of the regular grid nodes and spaced so that they fall on other grid nodes in line with one of the grid axes. Finally, a standard input file type combining all the array configurations is written for a commercial 3D inversion code. Commercial 3D inversion programs such as EarthImager 3D™ and EarthImager 3DCL™ by Advanced Geosciences Inc. are able to read the standard input file and conduct the resistivity 3D inversion.

*Synthetic Model Study*

We conducted a synthetic model study as an initial evaluation of the effectiveness of the proposed binning method. For the study we constructed a synthetic 3D resistivity model containing two localized regions of anomalous resistivity. We then generated synthetic data over the model to simulate different DC resistivity surveys. We used a 3D finite element forward modeling program that solves Poisson's equation for voltages at arbitrary receiver electrode locations in response to current injected between arbitrary source electrode locations. Groups of virtual source and receiver locations were generated to simulate a conventional, parallel-line, land survey and four CRP surveys with measurements made at differing spatial densities.

The synthetic model contained two 3D bodies of 10 Ohm-m material within a background of 100 Ohm-m material (Figure 2.2). The two anomalous regions were both rectangular prisms, but were given different sizes and aspect ratios, in order to test the resolution of the results from the binning method. The dimensions of the first anomalous region were 10m ×20m ×4m, whereas the dimensions of the second were 20m ×20m ×5m. The mesh was designed with small elements near the anomalous regions in the center of the model and increasingly larger elements further away from the center to ensure the numerical accuracy, without excessive computational run times (Figure 2.2). The synthetic forward model was composed of 133 ×133 ×24 elements in the X, Y and Z direction, respectively. The smallest elements were 1 m on a side in the region in which the source electrodes are located.

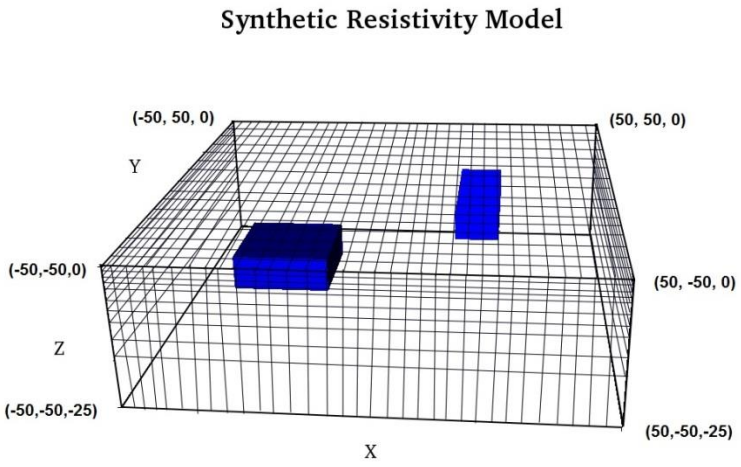


Figure 2.2 Synthetic 3D model. A synthetic 3D model used in the synthetic study, showing two low resistivity bodies (10 ohm-m) each embedded in a higher resistivity background (100 ohm-m). The two anomaly bodies (blue color blocks) are buried 2.5m deep in Z direction. The figure only shows the central part of the model. The total number of the meshes in the model is 133(X direction) × 133(Y direction) × 24(Z direction).

The synthetic apparent-resistivity data for the 3D model were generated assuming that the measurements were made on the model surface. For the parallel-line synthetic survey, the electrodes were arranged in parallel lines to simulate a conventional 3D DC resistivity land survey by using a dipole-dipole array configuration with n = 1 and 5 meter electrode separation (Figure 2.3(a)). The parallel-line synthetic survey acted as a "control group" for the other synthetic surveys. Precisely located, parallel lines are the "optimal condition" for a conventional 3D survey, which can be inverted directly, with no binning applied to the synthetic model response.

The remaining four synthetic surveys were generated assuming the electrodes were irregularly distributed on the surface of the synthetic model to simulate field CRP survey, using the same synthetic resistivity model and finite element forward modeling program. However, the location and density of the electrodes was different for each case

(Figure 2.3). For the low-density synthetic survey (Figure 2.3(b)), the locations of 407 electrode arrays were cropped from electrode locations from an actual CRP field survey. For the other three synthetic surveys, the positions of 600, 1200 and 2400 electrode arrays were randomly generated over the central model region. We evaluated the proposed binning method by comparing the results after inversion of the four synthetic CRP surveys, which required the binning method, to the results of the parallel-line synthetic survey.

The electrode positions for the parallel-line synthetic survey were generated on parallel lines, thus the synthetic data were ready for a 3D inversion, without binning. For the remaining four synthetic surveys, the binning method had to be applied before inversion due to the irregular distribution of the electrodes' location. Hence, before the 3D inversions were performed, the output files of remaining four synthetic surveys from the forward modeling were processed using the proposed binning process. The scattered data sets were converted to data sets on rectangular grids, with the same line and electrode location as the parallel-line survey. After the binning method was applied, a total of 81 10m-by-10m square bins were created, with 9 bins on both X and Y direction. The data density for the four synthetic surveys averaged 5, 7, 15, and 30 measurements per bin, respectively. However, the number of measurements within individual bins varied.

Then binned electrode locations were regenerated for the low-density synthetic survey through the high-density synthetic surveys, at the same electrode positions and with the same array configurations as the parallel-line synthetic survey. The final 3D inverted resistivity volumes for the low-density synthetic survey through the high-density

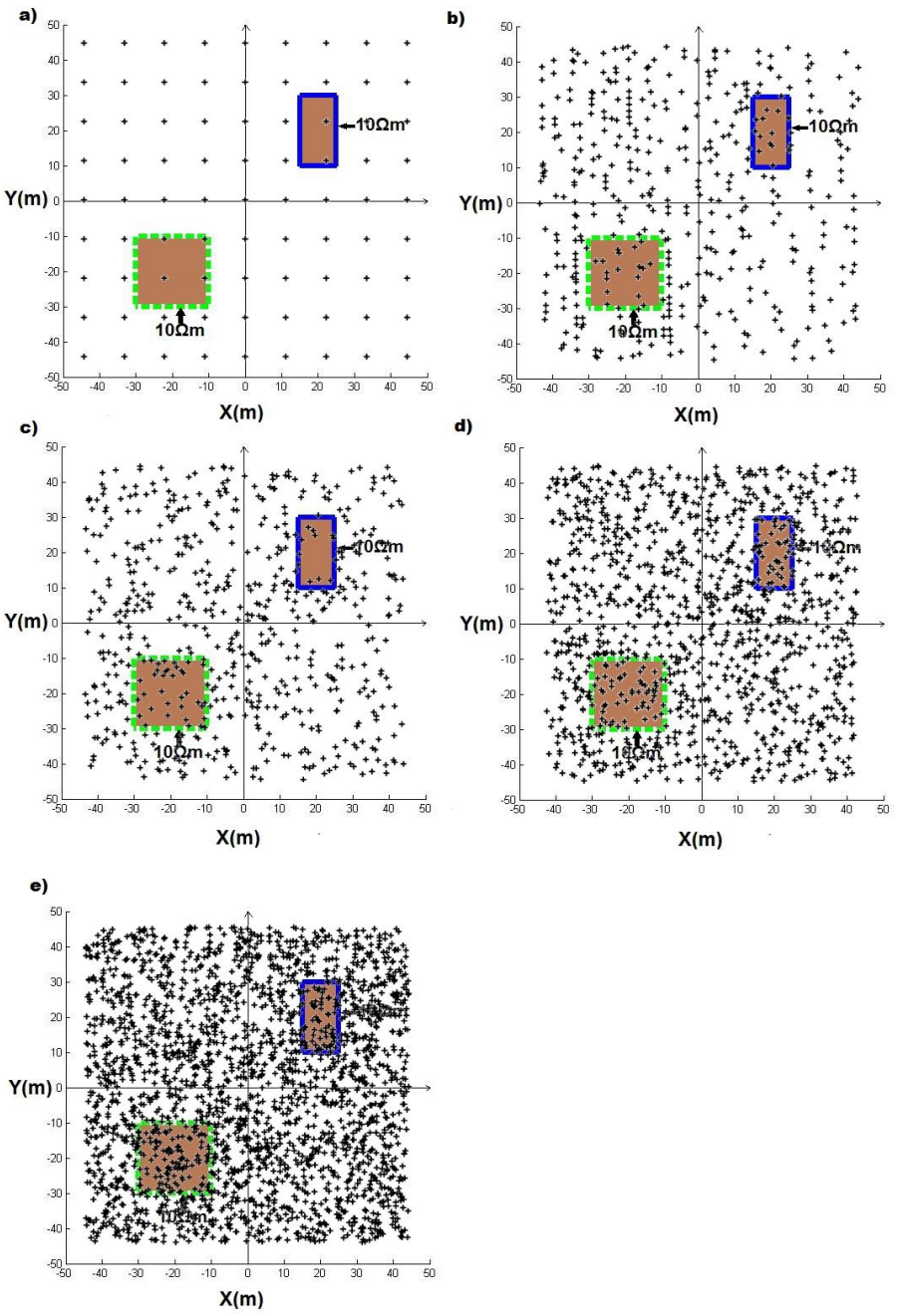


Figure 2.3 Plan view of the synthetic model at depth of 2.5m. The black cross shows the positions of electrode arrays' centers on the model surface during the synthetic survey. a) Electrodes are arranged in parallel lines in parallel-line synthetic survey. b) In low-density synthetic survey, locations of 407 electrode arrays were cropped from a field survey. c) Positions of 600 electrode arrays for medium-low-density synthetic survey. d) Positions of 1200 electrode arrays for medium-high-synthetic survey. e) Positions of 2400 electrode arrays for high-density synthetic survey.

synthetic survey were then quantitatively compared to the parallel-line synthetic survey and the actual resistivity distribution in the input synthetic forward model, for assessment.

We used the EarthImager 3DCL™ program to carry out the inversion of the synthetic resistivity surveys. The 3D inverted models were calculated from the synthetic surveys using the smoothness-constrained, least-square optimization. The program automatically divides the subsurface into a number of rectangular-prism elements and attempts to determine the resistivity of the elements that produces agreement with the measured apparent resistivity values within a specified tolerance, by an iterative forward modeling and correction scheme. No attempt was made to match the finite element mesh used in the inversion with that used in the forward modeling. The inversions of the synthetic surveys were carried out to 8 iterations. For each of the iterations, the root-mean-squared (RMS) error between the input apparent-resistivity data and the apparent-resistivity values generated from the inverted model for the 5 synthetic surveys were calculated in order to pick the optimal inversion result. The RMS measure of error is defined by:

$$RMS = \sqrt{\frac{\sum\left(\frac{\rho_{calc} - \rho_{inp}}{\rho_{inp}}\right)^2}{N}} \times 100\% \qquad (2.2)$$

where $N$ is the number of the apparent resistivity values, $\rho_{calc}$ is the apparent resistivity calculated from the inversion model, and $\rho_{inp}$ is the input apparent resistivity value. The RMS error was calculated for each of the iteration during the 3D inversion of the synthetic surveys.

To evaluate the quality of our binning technique, we calculate the model-misfit ($M_{misfit}$) value using the inverted model of the parallel-line survey as the control group, compared to the inversion models for the binned synthetic CRP surveys. The measure of misfit is expressed as:

$$M_{misfit} = \sqrt{\frac{\sum\left(\frac{\rho_{calc} - \rho_{con}}{\rho_{con}}\right)^2}{N}} \times 100\% \qquad (2.3)$$

where $N$ is the number of independent subsurface resistivity values, $\rho_{calc}$ is the inverted resistivity model for the second through the fifth synthetic survey, $\rho_{con}$ is the inverted resistivity model for "control group" the parallel-line survey.

## *Field Study*

### *Site Description*

To further test the proposed binning method, we applied the method to two field CRP surveys collected as part of a groundwater investigation and water budget research on Maui Island, Hawaii. The groundwater investigation included CRP surveys as well fixed 2D resistivity profiles within water reservoirs. The goal of the surveys was to identify areas in which water was flowing into or out of the reservoir bottoms.

The first study site was Waiale Reservoir (Figure 2.4(a)) on Maui Island, Hawaii, which is an agricultural reservoir belonging to Hawaiian Commercial & Sugar Company (HC&S). The reservoir is about 610 m long, 150 m wide and has a surface area of about 8 hectares. Waiale Reservoir is one of 43 reservoirs that provide temporary storage for irrigation water for the 14,400 hectare HC&S sugarcane plantation on Maui Island. The

reservoir is underlain by a thin sedimentary section between the two major volcanoes that form the island. The water stored in the reservoir is fresh water transferred from neighboring mountains by canals.

The second study site was HC&S Reservoir 50 (Figure 2.4(b)), which is another one of HC&S irrigation reservoir on Maui Island. Reservoir 50 is about 200m long, 75m wide, with a surface area of about 1.32 hectares. Unlike Waiale Reservoir, Reservoir 50 is underlain by fractured and weathered basalt.

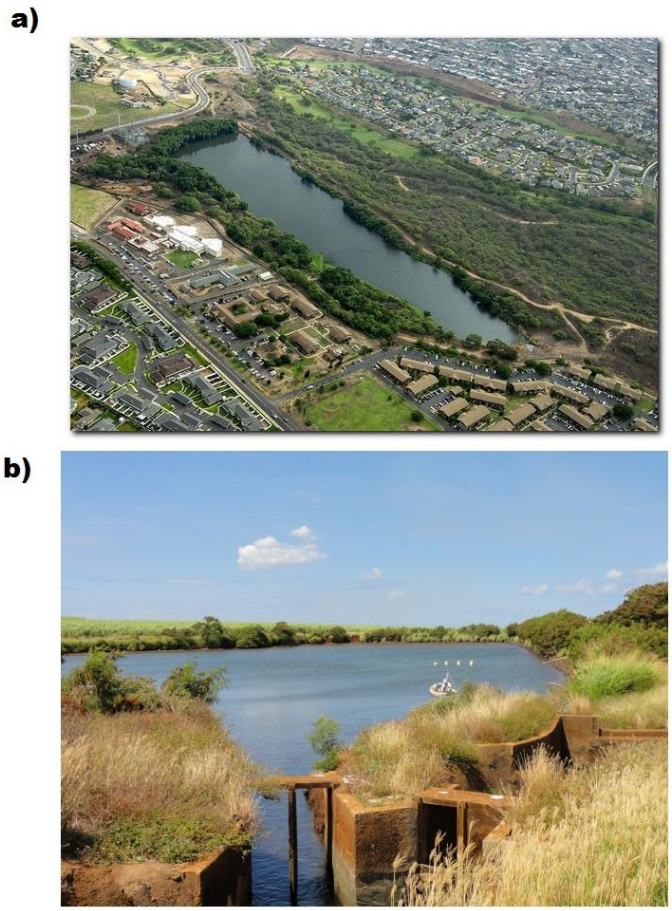


Figure 2.4 Study sites. A) Waiale Reservoir (Reservoir 73), Maui, Hawaii. B) HC&S Reservoir 50, Maui, Hawaii.

*Field Data Acquisition*

The resistivity surveys within the two water reservoirs were carried out in July, 2012. The surveys were conducted with a Marine Supersting R8-IP™ multi-channel resistivity system by Advanced Geosciences Inc. The CRP surveys were carried out using the dipole-dipole array implemented on a streamer cable with 11 addressable graphite electrodes spaced 5 m apart. An onboard GPS was used to navigate the survey vessel and to record geographic location of the vessel during the surveys.

Before starting collecting CRP data, the streamer was towed for a distance until it was straight. During the CRP data acquisition, the injected current ranged from 97 mA to 180 mA at the first study site and 662 mA to 1309 mA at the second study site. For the dipole-dipole array configuration, the first two of eleven electrodes, were current electrodes and the other nine were potential electrodes, producing a maximum electrode offset of 50 m. We assumed that the electrodes along the streamer cable follow the survey vessel track during the whole survey under gentle maneuvering and speed of 3 km/hr (Snyder, 2002). During the surveys, the survey vessel was driven along lines directly up and down the current wind direction to prevent the sideways deflection of the array, away from the vessel track. This resulted in irregular line orientations during the surveys as the wind direction changed.

To produce 3D inverted volumes of with enough resolution to satisfy the study objectives, we acquired data at sufficient density to have multiple readings within 10 m × 10 m bins over the reservoir surfaces. To achieve this density, we collected 16,408 data points at the first study site and 8,344 data points for the second site, with the measurement points irregularly spread over the two reservoirs (Figure 2.5). In the field

surveys conducted for this study, the average data density was about 1 data point per 50 $m^3$, or about 40 measurements per bin after combining all the subgroups. Since the system can make 8 measurements every 15 second, it was possible to collect data at this density over the 80,000 $m^2$ reservoir at the first site in three to four hours with a vessel speed of 3 km/hr (Advanced Geosciences Inc., 2006; Day-Lewis et al., 2006). Proportionally less time was required at the second site.

In addition to the CRP surveys, we conducted fixed 2D DC resistivity profiles across both of the reservoirs (Figure 2.5). Conventional fixed 2D DC resistivity profiles across water bodies have been done in the past, by installing electrodes on the bottom of reservoir or streambed (Nyquist, 2008; Goto, 2008). However it requires a lot of effort and time to install the electrodes and it is hard to layout the electrodes on a straight line. Thus during this survey, we carried out fixed 2D "floating" DC resistivity surveys for Waiale Reservoir and Reservoir 50. The same instrumentation was used as in the CRP surveys, but with a 135m 28-electrode cable designed for marine and water-reservoir surveys. This cable is long enough to span the whole reservoir during the survey. Rather than installing the electrode on the water bottom, we floated the electrodes, wrapped by plastic buoys, on the water surface as in the CRP surveys. The two ends of the electrode array were attached to stakes on opposite shores to keep the array fixed and straight before the measurements were made (Figure 2.6). We collected two 2D DC resistivity profiles at the first study site and one profile for at the second study site. The 2D profiles were used to qualitatively compare with the 2D lines extracted from the inverted 3D model produced from the binned CRP data.

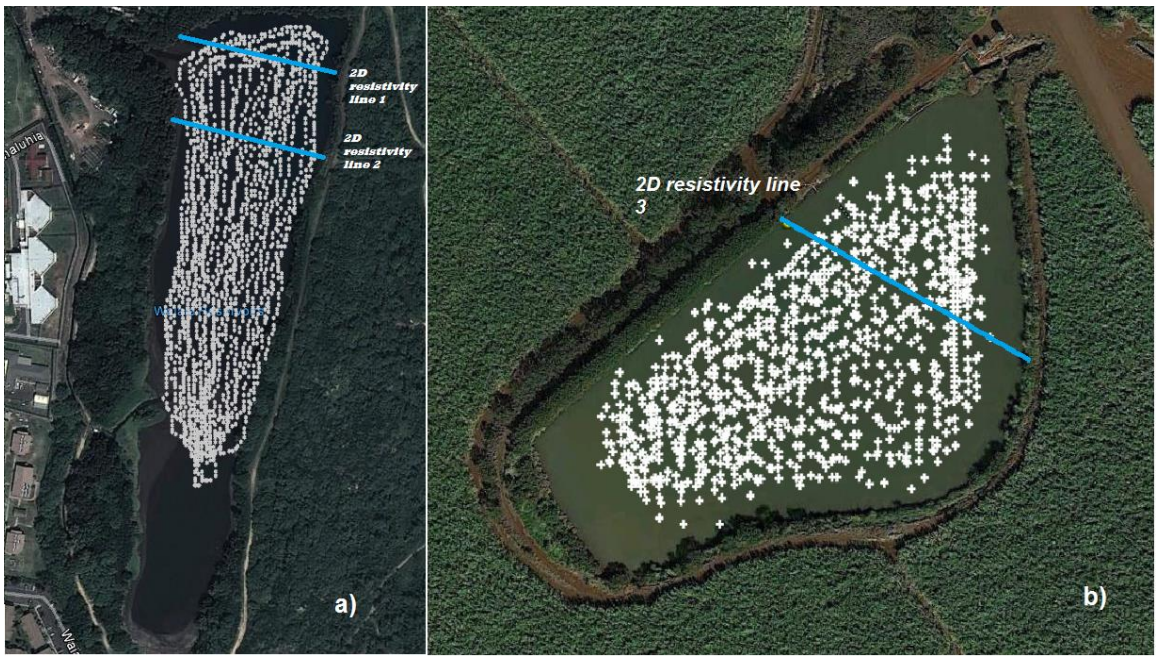


Figure 2.5 CRP survey and fixed 2-D DC resistivity survey of Waiale Reservoir and Reservoir 50. a) The white dot symbols show the position of data measurement for channel 1 in the Waiale Reservoir. Raw data has a total number of 16,408 measurements. The two blue lines show the locations of fixed 2-D resistivity survey lines. b) The white cross symbols show the position of data measurement for channel 1 in Reservoir 50. Raw data has a total number of 8,344 measurements. The blue line shows the location of the fixed 2-D resistivity survey line.

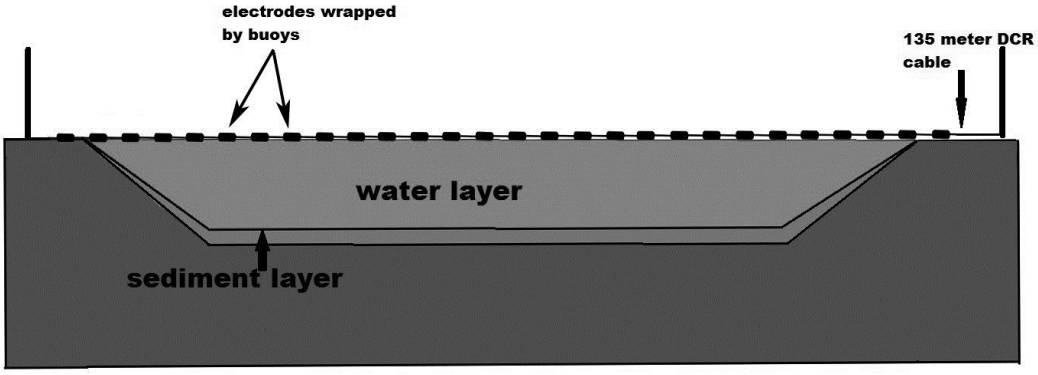


Figure 2.6 Field setup for fixed 2-D resistivity survey. A 135-m, 28-electrode cable was attached to metal stakes on opposite shores, and 28 electrodes were floated on the water surface during the data acquisition.

*Field Data Processing*

After the data were collected, 1.55% of the points were removed in the initial filtering process described above for Waiale Reservoir. The average value for the apparent resistivity after editing was 155.2 ohm-m, with a range from 24.01 ohm-m to 565.8 ohm-m. The binning method was then used to generate virtual readings on a regular grid and combined into a standard stg file (Advanced Geosciences, 2006). For each data subgroup, the centers of the electrode arrays for each measurement were binned into 465 bins and each of them has a size of 10 m ×10 m. (Figure 2.7). The empty bins within the reservoir were filled with the average value of surrounding bins. For those bins outside the reservoir area, we assigned the resistivity value based on a land resistivity survey near study reservoir. Thus a dataset with a total number of 5616 data points was created.

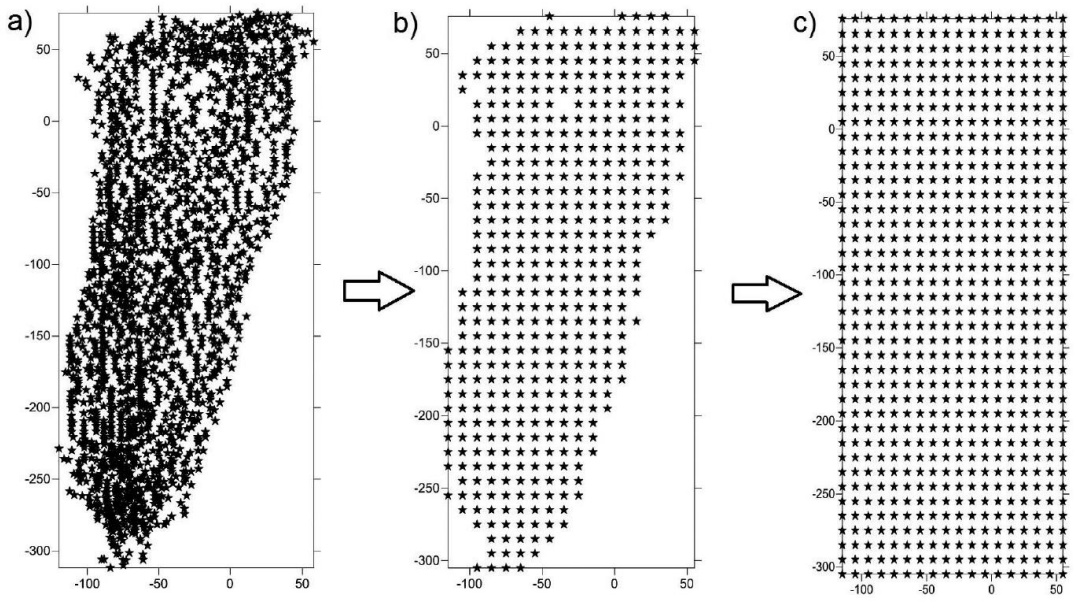


Figure 2.7 Binning of irregularly distributed CRP data in Waiale Reservoir. a) Raw CRP points for channel 1 within Waiale Reservoir. b) The data were binned on a regular grid with 10 3 10 m bin size using the proposed binning method (Figure 2.1). c) The empty bins are filled based on a priori data or surrounding data values.

The data collected from the Reservoir 50 was edited and processed by the same method. In the initial data filtering, about 1% of data points were removed from the original data set. The average value of the apparent resistivity for the filtered data set was 38.9 ohm-m, ranging from 14.042 ohm-m to 129.27 ohm-m. Since the area of the Reservoir 50 is smaller than Waiale reservoir, the data points in each subgroup were binned into 145 bins with 10m×10m individual bin size, with a total data point of 1106 after assigning resistivity value outside the reservoir area.

After the standard AGI stg files were created by the binning methods, EarthImager3DCL was used to conduct 3D inversion for both of the reservoirs with parallel computing. For the first study site, the inversion process required 82 hours of CPU time working in parallel on a work station with two, 6-core processors and 144 gigabytes of RAM. For the smaller Reservoir 50, it took 30 hours to conduct the 3D inversion on the same computer. Beside the RMS error, the L2 norm is also calculated as a measure of goodness of fit:

$$L2norm = \sum_{i=1}^{N} \left( \frac{\rho_i^{calc} - \rho_i^{inp}}{w_i} \right)^2 \qquad (2.4)$$

where $N$ is the number of the apparent resistivity values, $\rho_i^{inp}$ is the input (measured) apparent resistivity value, $\rho_i^{calc}$ is the calculated apparent resistivity computed from the inversion model, and $W_i$ is the data weight.

Similar to the 3D data processing, the methodology adopted for inverting the 2D fixed DC resistivity profiles consisted of 1) manual editing to remove outlier values, 2) formatting the original data file, 3) 2D inversion of apparent-resistivity data by

EarthImager 2D. Compare to 3D CRP data, the number of outlier readings in 2D data files were significantly lower, totaling less than 3% for all the three profiles.

## *Results*

### *Synthetic Model Results*

In the inversion of the synthetic survey data, the root-mean-squared (RMS) errors between the input apparent-resistivity data, and the apparent-resistivity values generated from the inverted models for the 5 synthetic data sets decreased significantly with the first several iterations. The RMS error decreased about 50% in the first iteration for all synthetic surveys and dropped dramatically after the second iteration. After 4 iterations, the RMS error of all the five synthetic surveys dropped to below 7%, and then stopped significant improvement. Although we aimed to reduce the data misfit between the input apparent resistivity data and the generated apparent resistivity value, the inverted model with the lowest RMS error might not be the best model due to the numerical errors and round off errors (Advanced Geosciences Inc., 2006). Thus stopping the iteration at the point the RMS error not dropping significantly is a prudent approach for this study. Based on the results, we stopped the inversion process after iteration number 4 for all the five synthetic surveys.

The 3D inverted volumes of all five synthetic surveys shows relatively accurate locations for the centers of the two low resistivity anomalies at depth of 2.5m after four iterations (Figure 2.8). However, for the low-density synthetic survey, the shape of the smaller anomaly is distorted in comparison to causal body in the forward synthetic model. Moreover, compared to the inversion of the parallel-line survey, the remaining four

binned surveys produced smoother inverted volumes, with lower amplitude resistivity anomalies, especially for the square-shaped anomalous body in the third quadrant. The agreement between the forward model input and the inversion results was also improved with increased data density: compared to the low-density and medium-low-density synthetic surveys, the inverted volumes of the fourth and fifth synthetic surveys had resistivity values closer to the input forward model.

Table 2.1 summarizes the variation of Model misfit(*Mmisfit*) between the low-density synthetic survey through high-density synthetic survey to the "control group" parallel-line survey. At iteration 4, the *Mmisfit* is 19.87%, 12.38%, 9.49% and 10.90% for inverted result of the second through the fifth synthetic surveys, respectively. This means, compared to the parallel-line and low-density synthetic surveys, the inverted results of the medium-high-density and high-density synthetic surveys were qualitatively closer to the inverted result form the parallel-line survey, which is consistent with general appearance of the inverted volumes. Not surprisely, the binned results more closely reproduced results from the straightline survey as the CRP data density increased.

*Field Study Results*

*Study site 1.* A 3D inverted volume of Waiale Reservoir was produced by the binning method applied to field CRP data with a 10m-by-10m bin size (Figure 2.9(e)). The RMS error between the input apparent-resistivity data and the resistivity values computed from the inverted model was 6.56% and the L2 norm was 0.35. Abrupt changes in resistivity were observed near the top of the 3D inverted volume. We attribute this feature to the presents of a metallic object on the reservoir bottom or in the shallow

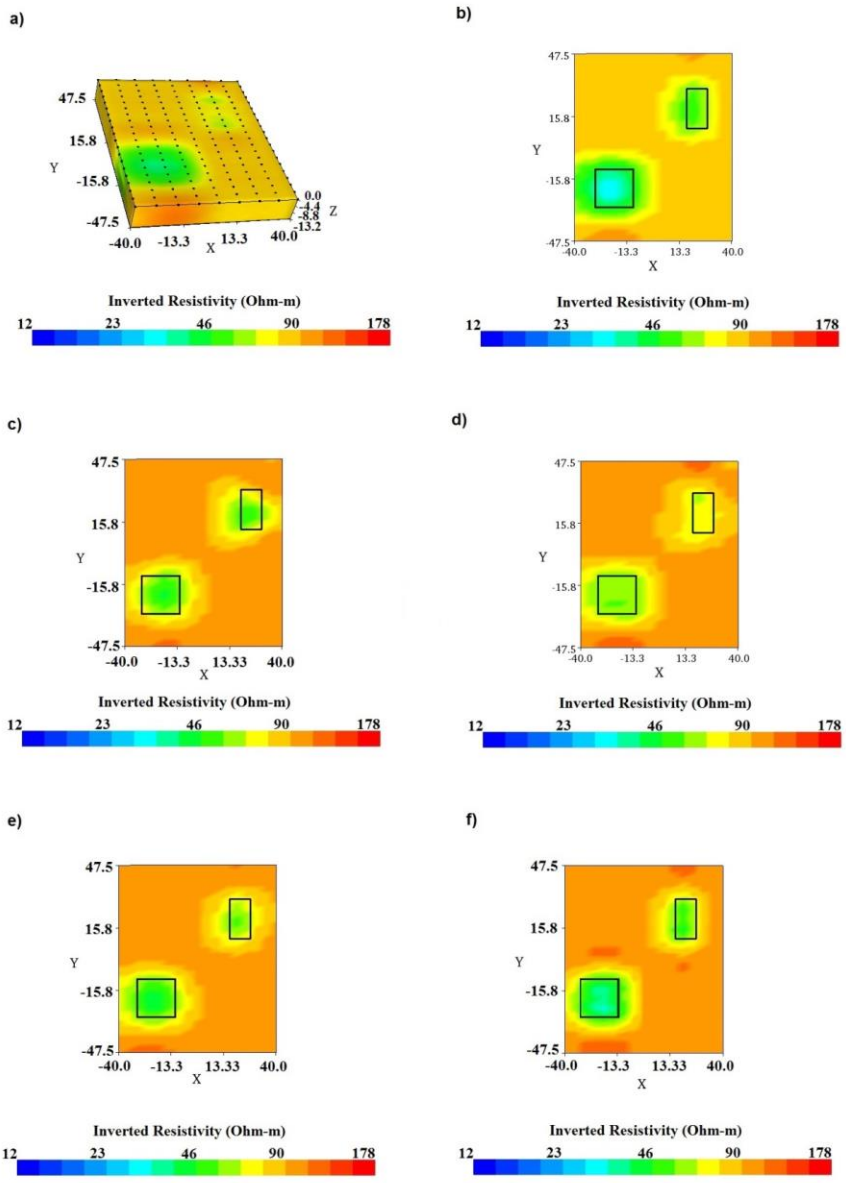


Figure 2.8 3-D inverted volume and horizontal slices of 3-D inverted volume for synthetic surveys. The black frames show the position of the two low resistivity anomalies in the original synthetic model shown in Figs. 1 and 2. a) 3-D inverted volume for parallel-line synthetic survey. b) Horizontal slice of the 3-D inverted volume at a depth of 2.5 m for the parallel- line synthetic survey. c) Horizontal slice of the 3-D inverted volume at a depth of 2.5 m for the low density synthetic survey. d) Horizontal slice of the 3-D inverted volume at a depth of 2.5 m for the medium-low-density synthetic survey. e) Horizontal slice of the 3-D inverted volume at a depth of 2.5 m for the medium-high-density synthetic survey. f) Horizontal slice of the 3D inverted volume at depth of 2.5m for high-density synthetic survey.

sub-bottom. The water in the reservoir had a resistivity value of 200 Ohm-m and averaged between 1 and 2 m in depth. At the depth between 7m and 11m below the water surface, a continuous low resistivity value layer was observed.

The inverted 2D resistivity profiles across Waiale Reservoir explain the observed resistivity values with a RMS error values between observed and computed resistivity data of 3.94%, 10.6% and L2 norms of 3.59, 14.63 after the eighth iteration for the Line 1 and Line 2, respectively (Figure 2.9 (a) and (b)). The larger average misfit for the second profile is due to large errors in one small part of the profile, near the water bottom on the northwest side of the reservoir. Just like the 3D inverted volume, abrupt changes in resistivity were observed on CRP profiles crossing this part of the reservoir. At the time of the survey, the water in the reservoir had a resistivity of 180 Ohm-m and averaged between 1 and 2 m in depth. The profiles also show a continuous, sub-bottom, low resistivity layer, which extends from 7 to 11 m below the water surface, with resistivity values ranging from 6.2 to 15.7 ohm-m.

For a more direct comparison, we extracted two 2D lines from the 3D inverted model at the same positions of the 2D lines (Figure 2.9 (c) and (d)). Although the resolution of the 2D profiles extracted from the 3D volume is lower than the 2D inversion profiles based on the fixed 2D field data, the extracted profiles show the same continuous, sub-bottom, low resistivity anomaly at the depth of 7 to 11m, with resistivity values ranging from 13 to 34.5 ohm-m. The low resistivity layer is interpreted as being the result of higher-salinity pore fluid within the sediments beneath the reservoir than the relatively fresh water within the reservoir. If the high-resistivity water contained in the reservoir was flowing out through the reservoir bottom in parts of the profile, those flow paths

should be manifest by high resistivity breaks in this low resistivity layer. No such breaks are observed on either profile.

Neither the fixed 2D profiles nor the inverted 3D image show the evidence of concentrated water flow in or out on the bottom of this reservoir, possibly due to the seal formed by fine grained sediments deposited on the reservoir bottom since impoundment, although a small amount of dispersed inflow might exist, such as the pattern displayed on the profiles of second survey line at around point (105, -3.68) (Figure 2.9 (b) and (d)). However, if there were pathways of concentrated flow, local high resistivity anomalies in the shallow sub-bottom of the reservoir should be observed on either horizontal slices through inverted 3D volume (Figure 2.9 (f)) or fixed 2D profiles (Figure 2.9 (a) and (b)). None are visible. Hence, we conclude that if there are areas of inflow or outflow through the reservoir bottom, they must be small relative to the 10 m by10 m bin size. However, this does not rule out the possibility of flow through the dam face at higher reservoir water levels.

Table 2.1. The Mmisfit values between the inverted result of parallel-line (control group) synthetic survey and low-density through high-density synthetic surveys.

| Groups | Measurement points of binned synthetic surveys | *Mmisft* Value (%) |
|---|---|---|
| *Mmisfit* value between the inverted result of control group and low-density synthetic survey | 407 | 19.87 |
| *Mmisfit* value between the inverted result of control group and medium-low-density synthetic survey | 600 | 12.38 |
| *Mmisfit* value between the inverted result of control group and medium-high-density synthetic survey | 1200 | 9.49 |
| *Mmisfit* value between the inverted result of control group and high-density synthetic survey | 2400 | 10.90 |

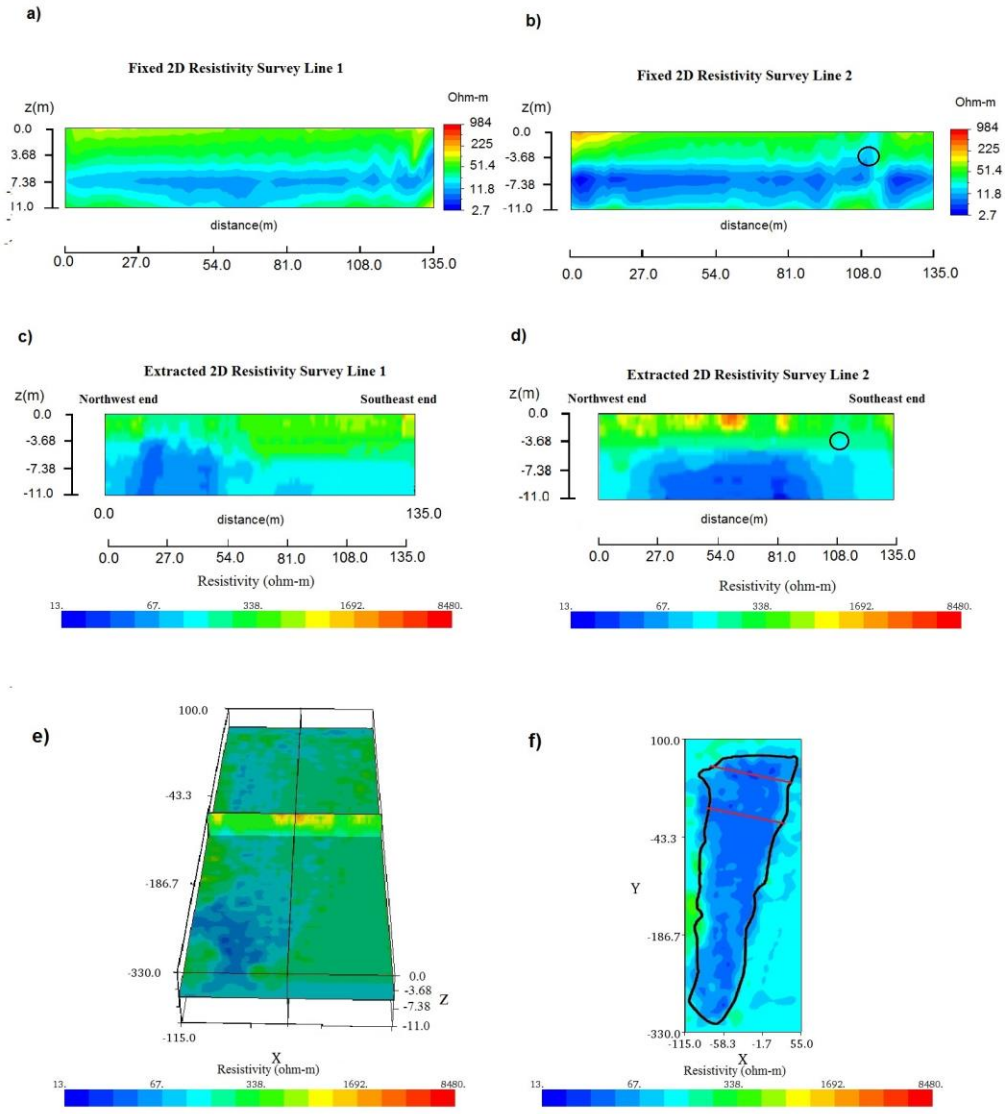


Figure 2.9: Inverted results of CRP data in study site 1, Waiale Reservoir. A) The inverted result of fixed 2D DC resistivity survey 1. B) The inverted result of fixed 2D DC resistivity survey 2. The black circle shows the position of possible dispersed flow on the bottom of Waiale Reservoir. C) Extracted 2D line from the 3D inverted model of binning method with the same position of 2D resistivity survey line 1. D) Extracted 2D line from the 3D inverted model of binning method with the same position of 2D resistivity survey line 2. The black circle shows the position of possible infiltration of groundwater into Waiale Reservoir from below. E) 3D inverted volume produce using the binning method applied to the CRP data of first field study site. The image has a vertical exaggeration of 4 on Z direction. b) A horizontal slice of the 3D inverted volume at depth of 11m (-11m on Z direction). The black line shows the border of the lake, and two red lines show the position of extracted 2D line.

*Study site 2.* The 3D inverted volume of Reservoir 50 was produced by binning method applied to the field data with a 10m-by-10m bin size (Figure 2.10(c)). The RMS error between the input apparent-resistivity data and the resistivity values computed from the inverted model was 7.1% and the L2 norm was 0.5. Due to the addition of more saline well water, the water in Reservoir 50 was approximately 20 Ohm-m. The 3D volume shows that the zone of low resistivity extends 100 m parallel to the northwest, along the down-slope shore of the reservoir, adjacent to the dam and cross to the up-slope side in the southern end of the reservoir. The "low-resistivity hole" is interpreted as potential leakage pathway in the background higher-resistivity bottom of Reservoir 50. The horizontal slice through the 3D inverted volume (Figure 2.10 (d)) allows us to estimate the aerial extent of the leakage pathway, which was identified on the 2D profile. The low-resistivity within this zone could be due to increased moisture due to leakage of reservoir water through the reservoir bottom, increased clay content associated with preferential weathering of the underlying basalt within the zone, or a combination of both factors.

The fixed 2D resistivity profiles across Reservoir 50 had a RMS error 4.29% and L2 norms of 4.49 after the eighth iteration (Figure 2.10 (a)). From the fixed 2D resistivity profile (Figure 2.10 (a)), we observe a shallow low-resistivity layer that extends from the surface to a depth of 3 to 4 m. This layer is likely associated with the reservoir water and saturated, fine grained sediments on the bottom of the reservoir. Over most of the reservoir, this low-resistivity layer is underlain by high resistivity interval that extends to the base of the 2D profile. However, near the point (-10, 30) on the 2D profile, the low-resistivity layer appears to extend through the underlying high-resistivity interval.

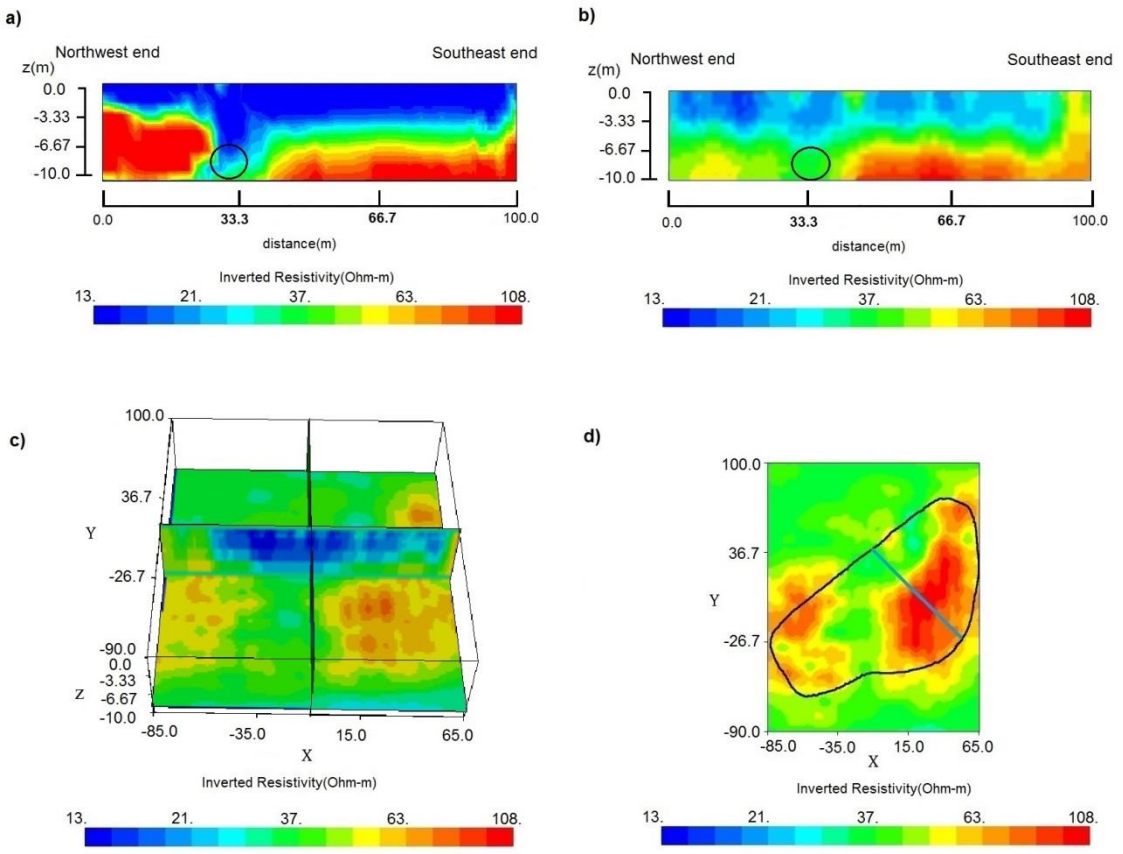


Figure 2.10 Inverted results of study site 2, Reservoir 50. A) Inverted result of fixed 2D survey 3. B) Extracted 2D line from the 3D inverted model of binning method with the same position of 2D resistivity survey line 3. C) 3D inverted volume produce using the binning method applied to the CRP data of second field study site (Reservoir 50). The image has a vertical exaggeration of 4 on Z direction. D) A horizontal slice of the 3D inverted volume at depth of 10m (-10m on Z direction). The black line shows the border of the lake and the blue line shows the position of extracted 2D line.

We extracted a 2D line (Figure 2.10(b)) from our 3D inverted volume at the same position of fixed 2D resistivity Line 3, a similar resistivity pattern was observed: a higher resistivity layer, with resistivity values larger than 100 ohm-m, under a lower resistivity layer ranging from 35 to 60 ohm-m under the reservoir. Similar to fixed 2D resistivity Line 3, near the point (-10, 30) on the extracted 2D profile, the low-resistivity layer also appears to extend through the underlying high-resistivity interval. That pattern shows

potential leakage pathway out of the reservoir and its extension downslope through to the underlying fractured basalt.

### *Discussion*

Synthetic and field studies used to evaluate the proposed binning method applied to irregularly distributed CRP data show that the technique produces results similar to those of parallel-line surveys. Based on the synthetic study results, inverted volumes produced from binned data can be expected to be smoother, with lower amplitude anomalous regions, and less edge resolution than, than results from parallel-line surveys. The accuracy achieved with the binning method is a function of the measurement density. In general, a higher measurement density of irregularly spaced CRP measurements is required to achieve comparable result through binning to regularly space measurements. This result is not unexpected, because uniform sampling produces the best representation of a function possible for a given number of samples (Jerri, 1977). We found that synthetic CRP surveys with a data density of 15-30 measurements per bin yielded inverted volumes that agreed with that of a parallel-line survey within an RMS misfit of about 10%, whereas results for densities of 5-7 measurements per bin were substantially worse. The resolution of the inversion volumes based on the higher-density CRP surveys was also better than that produced by the low-density surveys. Even so, the binned data set with as few as 5 measurements per bin were sufficient to detect anomalous regions larger than the bin size. For many applications, this may be all that is needed.

The high-density synthetic survey with higher data density appears to have a little higher *Mmisfit* value than the medium-high-density synthetic survey with lower data density (Table 2.1). Possible explanations for this is that the imperfection of our mesh

design during finite element forward calculation, or it could be the fact that the randomly created data points made the data density unevenly distributed among the bins. That might also suggest that when the data density of a survey reaches a specific level, improvement in the model misfit will reach a limit.

The results of the field study indicate that the binning method can be a practical and useful method for converting densely-spaced 2D CRP profiles into a 3D survey. Rather than carrying out a quantitative evaluation in synthetic survey, we qualitatively compared the inversion results from the binned data to the 2D inverted profiles. In 3D inverted volumes from study sites 1 and 2, the resistivity patterns (horizontal low resistivity layer and possible flow pathway) agree well with the inverted volume of fixed 2D lines.

Although far greater data density is required to produce inversion results reasonably close to those produced by conventional straight, parallel-line 3D surveys, in aquatic environments, collecting a higher density CRP survey and binning the data is more practical. Collecting straight, parallel-line 3D DC resistivity data in aquatic environments is limited by the length of the resistivity cable and the data acquisition time. For example, to conduct a conventional 3D DC resistivity survey in Waiale Reservoir, a minimum of seven days would have been needed to collect 60 2D profiles across the reservoir to achieve 10m resolution. In contrast, using a CRP survey of sufficient density to achieve comparable resolution in the larger Waiale Reservoir was acquired in just four hours. What is more, for 3D features such as a leakage pathway, the 3D inverted volumes from the binning method gave us a reasonable expectation of detecting all localized pathways larger than the bin size. A comparable field effort devoted to collecting sparse

2D profiles by stretch the electrode array from shore-to-shore, would have resulting in profiles spaced 100 m or more apart. Surveys of this kind could have missed small leakage pathways. These results demonstrate that the binning method can be a viable technique for aquatic surveys. The method is by no means a substitute for convention 3D DC resistivity survey due to the limit of quality of the inverted volume. However, the efficiency of the method makes it practical to conduct a 3D survey under conditions in which conventional acquisition and post-survey analysis is not practical.

The previously proposed methods of treating the problem of irregularly distributed 3D data by nudging or interpolating measurement locations onto straight lines, work best when the data are approximately regularly spaced to start with and only require minor adjustments (Rucker et al., 2009, 2011; Dahlin and Loke, 1997). However, even collecting resistivity profiles that are approximately parallel and regularly spaced is difficult in some case. In the field surveys conducted for this study, approximately the same amount of time was spent collecting the three 2D profiles used for comparison as was spent collecting all of the CRP data for the 3D surveys. Collecting a sufficient number of 2D profiles to cover surface area of the reservoirs at a 10m spacing, even allowing for some deviation from regular spacing, would have been cost-prohibitive. In such cases, the binning method we propose offers an alternative method for obtaining 3D coverage, rather than limiting the survey to a few, sparsely spaced 2D profiles.

This study was initially predicated on the fact that commercially available 3D inversion programs require data to be collected on regular grids. This is not a theoretical limitation, and in fact, there are open source 3D DC resistivity inversion programs that allow irregularly spaced source and receiver electrodes (Pidlisecky, 2007). In such

programs, irregularly spaced source electrodes are treated by using finite element interpolation functions to distribute current injected at arbitrary points within a finite element mesh between adjacent elemental nodes in the same way arbitrarily located point loads are treated in elastic deformation problems (e.g. Becker et al., 1981). After solving the resulting finite element problem for the voltages at elemental nodes, voltages at irregularly spaced receiver electrodes are determined using the same interpolation functions to interpolate the known voltages at neighboring nodes to the locations of the receiver electrodes. It would be possible to directly invert irregularly spaced measurements made using the CRP data with such programs, without resorting to binning. However, this approach would be far less computationally efficient. The increased data density requirement for irregularly spaced measurement is a result from sampling theory. Hence, the same increase in sample density is required to produce comparable results, regardless of how the data are processed. However, the computational effort to invert resistivity data sets grows linearly with the number of resistivity readings. In the binning process, many irregularly spaced measurements are used to estimate the values of a much smaller number of regularly spaced measurements, prior to inversion. This is done using an efficient interpolation scheme at low computational cost. Once this reduction is made, the inversion of the binned data requires the same computational effort as that of regularly space field samples of the same density. This is true regardless of which inversion program is used. The alternative approach of treating the large number of irregularly spaced samples directly in the inversion process would require a much larger computational effort. For example, the computational time for the binning process and 3D inversion is approximately 2 minutes for a 2400-measurements synthetic survey on a

4-core computer, with 3.40 GHz CPU and 8 Gb of RAM. However, direct inversion of the same synthetic survey would require 15 to 30 times the computation effort to achieve the same level of RMS misfit. Hence, the development of widely available 3D DC resistivity inversion programs that treat irregularly spaced readings directly would not completely negate the usefulness of the binning method proposed here.

### *Conclusion*

CRP is a popular DC resistivity acquisition method, because of its efficiency; however the conventional CRP method is limited to 2D profiling due to the lack of precise control in profile spacing and orientation during data acquisition. To solve this problem, we propose a binning method for irregularly spaced CRP data, based on the inverse-distance weighted interpolation method. The binning method provides a 2-D interpolator for the irregularly distributed data sets and combines multiple 2D CRP profiles to produce a data set suitable for 3D inversion using widely available programs. Compared to the traditional sparse-profile 2D CRP survey, the 3D inversion with the help of binning technique has clear advantages, gleaning more information about the water body and sub-bottom. The resistivity model obtained from the 3D inverted volume shows the potential to resolve more complex geological structure and provides more options for quantitative interpretation when compared to the 2D inverted models.

Since 3D inversion of CRP facilitated by the binning technique does not require data points on the regular grid as the conventional 3D inversion, it can greatly reduce difficulties of data acquisition and data collection time, in aquatic environments. The performance on the field CRP examples shows that the method is computationally

efficient and suitable for lacustrine environment. It should also work in other environments, such as riverine and marine environments.

We conclude that there is still a work ahead to make this binning technique an efficient and practical tool for 3D marine resistivity surveying. Future research will involve testing the technique in different environments such as marine seafloor, correlating the inverted volumes produced from binned data sets with corroborative data, such as temperature, conductivity and bathymetry data, to produce a more accurate model, and testing other interpolation methods to determine if a more suitable interpolator for DC resistivity data exists.

## *Acknowledgments*

We thank Peter Allen and Justin Lau provided assistance with planning and field work. This work was supported in part of grants from U.S. Department of Agriculture: 58-6206-1-051.

## *References*

Advanced Geosciences Incorporated, 2006, *Instruction manual for EarthImager 2D*. Advanced Geosciences, Inc., Austin, Texas.

Advanced Geosciences Incorporated, 2006, *Instruction manual for EarthImager 3DCL*. Advanced Geosciences, Inc., Austin, Texas.

Amidu, S., and Dunbar, J., 2008, An evaluation of the electrical-resistivity method for water-reservoir salinity studies. *Geophysics*, 73(4), G39-G49.

Ball, L. B., W. H. Kress, and J. C. Cannia., 2006, Determination of canal leakage potential using continuous resistivity profiling techniques in western Nebraska and eastern Wyoming. In *Proceedings of SAGEEP*, Seattle.

Bartier, P. M., and Keller, C. P., 1996, Multivariate interpolation to incorporate thematic surface data using inverse distance weighting (IDW). *Computers & Geosciences*, 22(7), 795-799.

Becker, E. B., Carey, G. F., and Oden, J. T., 1981, *Finite Elements, An Introduction, Volume 1*. Prentice Hall, Englewood Cliffs, New Jersey, 107-109.

Belaval, M., Lane Jr, J. W., Lesmes, D. P., and Kineke, G. C., 2003, Continuous-resistivity profiling for coastal groundwater investigations: three case studies. In *Proceedings of SAGEEP*, San Antonio, 397-410.

Briggs, I. C. 1974, Machine contouring using minimum curvature. *Geophysics*, 39(1), 39-48.

Cordell, Lindrith E., 1992, A scattered equivalent-source methods for interpolation and gridding of potential-field data in three dimensions. *Geophysics*, 57(4), 629-636.

Dahlin, T., and Loke, M. H., 1997, Quasi-3D resistivity imaging-mapping of three dimensional structures using two dimensional DC resistivity techniques. *3rd EEGS Meeting*.

Dampney, C. N. G., 1969, The equivalent source technique. *Geophysics*, 34(1), 39-53.

Day-Lewis, F. D., White, E. A., Johnson, C. D., Lane Jr, J. W., and Belaval, M., 2006, Continuous resistivity profiling to delineate submarine groundwater discharge—Examples and limitations. *The Leading Edge*, 25(6), 724-728.

Dey, A., and Morrison, H. F., 1979, Resistivity modeling for arbitrarily shaped three-dimensional structures. *Geophysics*, 44(4), 753-780.

Dunbar, J. A., S. A. Amidu, and P. M. Allen., 2008, A Study of Seasonal Salinity Variation in Lake Whitney, Texas using Continuous Resistivity Profiling. In *Proceedings of SAGEEP*, Philadelphia.

Fomel, S., 2001, *Three-dimensional seismic data regularization*. Stanford University, Stanford, California.

Goto, T. N., Kasaya, T., Machiyama, H., Takagi, R., Matsumoto, R., Okuda, Y., Satoh, M., Watanabe, T., Seama, N., Mikada, H., Sanada, Y., Kinoshita, M., 2008, A marine deep-towed DC resistivity survey in a methane hydrate area, Japan Sea. *Exploration Geophysics*, 39(1), 52-59.

Guo, L., Meng, X., and Shi, L., 2012, Gridding aeromagnetic data using inverse interpolation. *Geophysical Journal International*, 189(3), 1352-1360.

Jerri, A. J., 1977, The Shannon sampling theorem—Its various extensions and applications: A tutorial review. *Proceedings of the IEEE*, 65(11), 1565-1596.

Krige, D. G., 1951, *A statistical approach to some mine valuation and allied problems on the Witwatersrand*, University of the Witwatersrand, South Africa.

Lam, N. S. N., 1983, Spatial interpolation methods: a review. *Cartography and Geographic Information Science*, 10(2), 129-150.

Li, X., and Goetze, H.J., 1999, Comparison of some gridding methods. *The Leading Edge*, 18(8), 898-900.

Li, Y., and Spitzer, K., 2002, Three-dimensional DC resistivity forward modeling using finite elements in comparison with finite-difference solutions. *Geophysical Journal International*, 151(3), 924-934.

Loke, M. H., and Barker, R. D., 1996, Practical techniques for 3D resistivity surveys and data inversion. *Geophysical Prospecting*, 44(3), 499-523.

Matheron, G., 1971, *The theory of regionalized variables and its applications*. École national supérieure des mines, 211.

Mitas, L., and Mitasova, H., 1999. Spatial interpolation, *Geographical Information Systems: Principles, Techniques, Management and Applications, vol. 1*., Wiley, London, 481– 492.

Nyquist, J. E., Freyer, P. A., and Toran, L., 2008, Stream bottom resistivity tomography to map ground water discharge, *Groundwater*, 46(4), 561-569.

Pidlisecky, A., Haber, E., and Knight, R., 2007, RESINVM3D: A 3D resistivity inversion package. *Geophysics*, 72(2), H1-H10.

Rucker, D. F., Levitt, M. T., and Greenwood, W. J., 2009, Three-dimensional electrical resistivity model of a nuclear waste disposal site. *Journal of Applied Geophysics*, 69(3), 150-164.

Rucker, D. F., Noonan, G. E., & Greenwood, W. J., 2011, Electrical resistivity in support of geological mapping along the Panama Canal. *Engineering Geology*, 117(1), 121-133.

Shepard, D., 1968, A two-dimensional interpolation function for irregularly-spaced data. *Proceedings of the 23rd ACM national conference*, 517-524.

Snyder, D. D., and Wightman, E., 2002, Application of continuous resistivity profiling to aquifer characterization. In *Proceedings of the SAGEEP*, Las Vegas, Nevada

Spitzer, K., 1995, A 3-D finite-difference algorithm for DC resistivity modelling using conjugate gradient methods. *Geophysical Journal International*, 123(3), 903-914.

Tomczak, M., 1998, Spatial interpolation and its uncertainty using automated anisotropic inverse distance weighting (IDW)-cross-validation/jackknife approach. *Journal of Geographic Information and Decision Analysis*, 2(2), 18-30.

Watson, D. F., and Philip, G. M., 1985, A refinement of inverse distance weighted interpolation. *Geo-Processing*, 4(2), 315-327.

Xu, S., Y. Zhang, D. Pham, and G. Lambare, 2005, Antileakage Fourier transform for seismic data regularization. *Geophysics*, 70(4), 87-95.

Zhang, J., Mackie, R. L., & Madden, T. R., 1995, 3-D resistivity forward modeling and inversion using conjugate gradients. *Geophysics*, 60(5), 1313-1325.

# CHAPTER THREE

## Seafloor Direct-Current Resistivity Techniques for Deep-Marine, Near-Bottom Gas-Hydrate Investigation

This chapter published as: Xu, T., Dunbar, J., Gunnell, A., Lutken, C., Higley, P., & Lagmanson, M. (2015). Seafloor direct-current resistivity techniques for deep-marine, near-bottom gas-hydrate investigation. *The Leading Edge*, *34*(2), 180-188.

*Abstract*

Geophysical investigations of the first 100 m below the seafloor in deep-marine environments are done to assess drilling hazards, to plan routes for pipelines and cables, and to study benthic organism communities. The tool of choice for these investigations is subbottom profiling, which uses acoustic signals in the range of 1 to 25 kHz to image near-bottom stratigraphy. An existing engineering-scale, direct-current resistivity (DCR) system for use in deep-marine, near-bottom environments has been adapted. It is potentially useful in settings in which the presence of free gas, gas hydrates, coarse sediment, cemented carbonate, or highly deformed sediment limits the effectiveness of the subbottom-profiling method. The adapted DCR system was used to survey Woolsey Mound, Mississippi Canyon Block 118 (MC118), Gulf of Mexico, to characterize the shallow gas hydrate system. Three conventional modes of DCR data acquisition—continuous-resistivity profiling (CRP), static array, and time lapse with a fixed array — were evaluated on the deep seafloor. High-resistivity anomalies likely associated with high concentration of hydrate deposits were imaged with all three modes of acquisition.

## *Introduction*

Although both academic research and industry exploration have benefited from complementary seismic and electrical methods to characterize deep marine sediments to depth approaching 10 km, a complementary electrical method has not been widely available for investigations of the upper most 100 m. For the past decades, engineering and geological investigation for the deep marine, near-bottom environment has become an emerging research topic, since such environments are of particular interest in assessing drilling hazards, planning routes for underwater pipelines and study the benthic organism communities.

The tool of choice for investigations of first 100 m below bottom is sub-bottom profiling, which is a non-invasive, marine-based technique that uses acoustic signals in the 1 to 25 kHz range to image near-bottom stratigraphy. However, the occurrence of free gas, gas hydrates, course sediment, cemented carbonate, or highly deformed sediment, limits the effectiveness of sub-bottom profiling, by showing only chaotic returns or abrupt termination of returns. A complementary geophysical tool is needed to image the near-bottom for investigation in settings in which sub-bottom profiling alone does not provide sufficient information.

For engineering- and environmental-scale investigations on land and in shallow marine settings, direct current resistivity profiling (DCR) provides just such a complementary tool to shallow reflection seismology or shallow sub-bottom profiling. The DCR method has been widely used to image the near-surface resistivity distribution in land, riverine, lacustrine and coastal environments by 2D, 3D and time-lapse methods.

Compared with other electrical methods, DCR offers cost, logistical, and computation advantages for investigation at engineering and environment scale.

Conventional waterborne DCR surveys have been performed in two modes: (1) the continuous-resistivity profiling (CRP) mode, in which a floating electrode array is towed by a survey vessel, and (2) the static-array profiling mode, in which electrodes are deployed in fixed positions on land or on the water bottom. The CRP mode has the advantage of large spatial coverage for reconnaissance surveys to identify resistivity anomalies. The static-resistivity mode potentially provides better resolution and inversion results because readings at a larger number of different electrode offsets can be acquired at each ground location, and the locations of the fixed electrodes can be determined more accurately. In addition, if the static array is left in place, multiple recordings can be made over the same profile without moving any equipment in time-lapse in situ monitoring.

In this study, we adapt a conventional engineering-scale DCR survey system for use on the deep seafloor. As an example application, we use the adapted system to characterize shallow gas-hydrate deposits beneath Woolsey Mound, Mississippi Canyon Block 118 (MC118), Gulf of Mexico. Because pure hydrate is essentially an electrical insulator, sediment containing hydrate or massive hydrate blocks is expected to stand out as high-resistivity anomalies in electrical resistivity data.

The goal of the study is to characterize the shallow gas hydrate distribution at the site and to monitor changes in the distribution over time. To this end, the DCR system is used first in CRP mode to conduct a reconnaissance survey of the mound and its surroundings. Next, the system is used in the static-array mode to identify targets for long-term monitoring. Then the array is left in place for a two-week test of the system in long-term

monitoring mode. High-resistivity anomalies, likely associated with high concentrations of gas hydrate, are imaged in inversion sections of data collected in all three acquisition modes.

The new seafloor DCR system is intended to fill a niche in near-bottom investigations, analogous to use of industry-scale controlled-source electromagnetics (CSEM) in combination with multichannel reflection seismology. Although subbottom profiling is the natural choice for investigation of shallow sediment, our seafloor DCR system satisfies the need for a noninvasive method to investigate sites with characteristics such as the presence of free gas, coarse sediments, gas hydrates, or consolidated carbonates, which limits the effectiveness of subbottom profiling. In addition, our system is designed to satisfy the particular need for a method that could be adapted easily to long-term monitoring of near-bottom sediment.

### *Seafloor DCR System*

We use a simple analytical model of the electrical properties of the deep-marine environment to assess the requirements for an engineering-scale seafloor DCR system. We approximate conventional DCR land data acquisition by the injection of current and by measuring voltages at points on the surface of a resistive half-space. We approximate DCR data acquisition on the deep seafloor by the injection of current and by measuring voltages at points on the interface between two half-spaces of differing resistivity, with an upper half-space of seawater and a lower half-space of shallow-marine sediments.

Compared with seawater, the seafloor sediments have at least three times larger resistivity. Hence, current injected into the near-bottom environment preferentially flows through seawater and not into the sediment. Towing or placing the electrodes directly on

the seafloor provides the best possible coupling of current into the bottom. The solution of this problem for a four-electrode resistivity measurement on the seafloor can be solved using the method of images, as was done for the conventional half-space problem (Roy, 2008):

$$\Delta V = \frac{\rho_w \rho_s I}{2\pi(\rho_w + \rho_s)}\left(\frac{1}{AM} - \frac{1}{AN} - \frac{1}{BM} + \frac{1}{BN}\right), \qquad (3.1)$$

where $\Delta V$ is the voltage difference between potential electrodes *M*, *N*, *I* is the injected current between electrodes *A* and *B*, *AM*, *AN*, *BM*, and *BN* are the respective distances between the current electrodes *A*, *B* and the potential electrodes *M*, *N*; and $\rho_w$ and $\rho_s$ are the resistivity values of seawater and shallow marine sediments, respectively.

For given seawater and sediment resistivities, along with knowledge of the falloff in injected current versus A-B offset, the voltage between M-N electrodes for different array types and lengths can be predicted from equation 1. Predicted voltages are compared with the background and system noise levels and the desired minimum signal-to-noise ratio to predict the maximum useful lengths of different array configurations (Figure 3.1).

Array configurations such as dipole-dipole and gradient array that allow full use of multichannel capability of the system are preferred for data acquisition. Regardless of the performance parameters of the DCR system used, offsets achievable with the gradient array (Figure 3.1b) are greater than for dipole-dipole arrays (Figure 3.1a). In our case, the CRP survey is conducted as a reconnaissance survey without a priori information of the depth of the gas hydrate. Therefore, the gradient array is applied for the CRP survey to obtain larger depth of investigation. Based on the CRP results, we combine a short-offset dipole-dipole array with a range of gradient-array lengths for the static and time lapse to better image the uppermost 50 m.

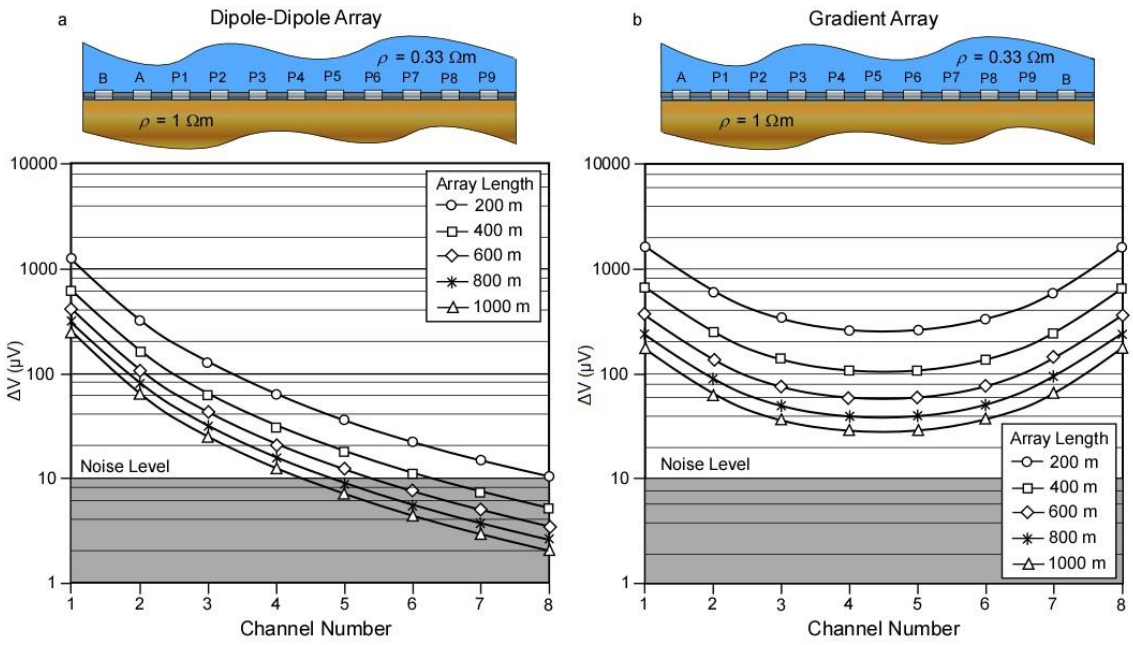


Figure 3.1 Predicted performance of the seafloor DCR system. a) Dipole-Dipole array. b) Gradient array. The total noise level on the seafloor was estimated by computing the root-mean-square voltage in the last of six 200ms IP windows, after a 2 s charge cycle. This noise estimated includes system noise, electrode noise, residual IP effects from the previous reading, as well as any ambient noise present on the seafloor.

Rather than developing new DCR instrumentation from the ground up, the seafloor DCR system (Figure 3.2(a)) takes advantage of a commercially available resistivity instrument used for near-surface applications, which we adapted for use on the deep marine environment. The resistivity instrument has peak output current of 2 A and a peak output voltage 400 V, limited by a maximum output power of 200 watts. In seawater, current coupling occurs at low voltage. Hence, the system is always current limited, rather than voltage limited. The instrument has eight recording channels to record received voltages between up to eight receiver pairs simultaneously and 56 automated switches to address 56 electrodes. During DCR acquisition, DC current is injected

between two source electrodes for a period of 1 to 2 seconds, while electrical potential is simultaneously measured between multiple receiver pairs.

Based on the Equation 3.1, for a maximum current output of 2 A, an estimated system noise level of 10 μV, and a 10-to-1 desired signal-to-noise ratio, the maximum useful offset for an eight-channel gradient array is about 660 m. An electrode array 1100 m long with 56 electrodes spaced 20 m apart is suitable for use in all three survey modes (Figure 3.2b). However, only the first 660 m is used in CRP mode. The array is constructed from high pressure, multiconductor cable combined with internal water-blocking material and graphite electrodes to prevent seawater intrusion and corrosion damage, respectively.

The seafloor resistivity system could be deployed in two configurations: (1) The instrument could be deployed on or near the seafloor in a pressure housing or (2) the instrument could remain on a surface vessel, and a long lead-in cable could be used to connect the instrument to the electrode array on the seafloor. A disadvantage of having the instrument on the surface vessel is that the DC signal would drop in power along the lead-in cable. In addition, the expense of having the surface vessel remain at the site for long periods would make time-lapse data collection impractical using this configuration. Therefore, we chose to place the instrument on the seafloor for data acquisition.

The resistivity instrument is installed in an aluminum pressure housing, which is rated as high as 1800 PSI for a maximum depth of investigation of as much as 1000 m. Operations at greater water depths would require stronger housing. The electrode array is connected to two 30-pin high-pressure underwater connectors that penetrate the pressure housing.

During the CRP and 2D static-resistivity surveys, the pressure housing containing the resistivity instrument is attached to the frame of a remotely operated vehicle (ROV) (Figure 3.2c) and communicates with the ROV through a third 24-pin connector that also penetrates the housing. The ROV provides power from its onboard battery as well as remote-control communication via a fiber-optic connection through its tow cable. This allows a person to operate the instrument remotely on the surface vessel in the same way the instrument is operated in normal land surveys. In addition, an acoustic beacon mounted on the ROV emits signals received by an acoustic array mounted on the survey vessel to provide the geographic position of the ROV.

For the time-lapse resistivity-survey mode, the pressure housing of the resistivity instrument, along with independent timing and control units, is attached to a seafloor lander platform (Figure 3.2d). The timing unit and control computer work together to operate the DCR system autonomously without a human operator to collect repeat resistivity data sets on a preprogrammed schedule.

The timing unit is an ultralow-power-demand device programmed to turn on and turn off power to the control unit and DCR instrument on a set schedule and to manage communication with the survey vessel via an acoustic modem. The low-power-demand control computer provides automated instructional control of the resistivity instrument, taking the place of a human controller. A camera platform is attached temporarily to the lander to provide live video feed from the seafloor and real time positioning data for navigating the seafloor lander during its deployment.

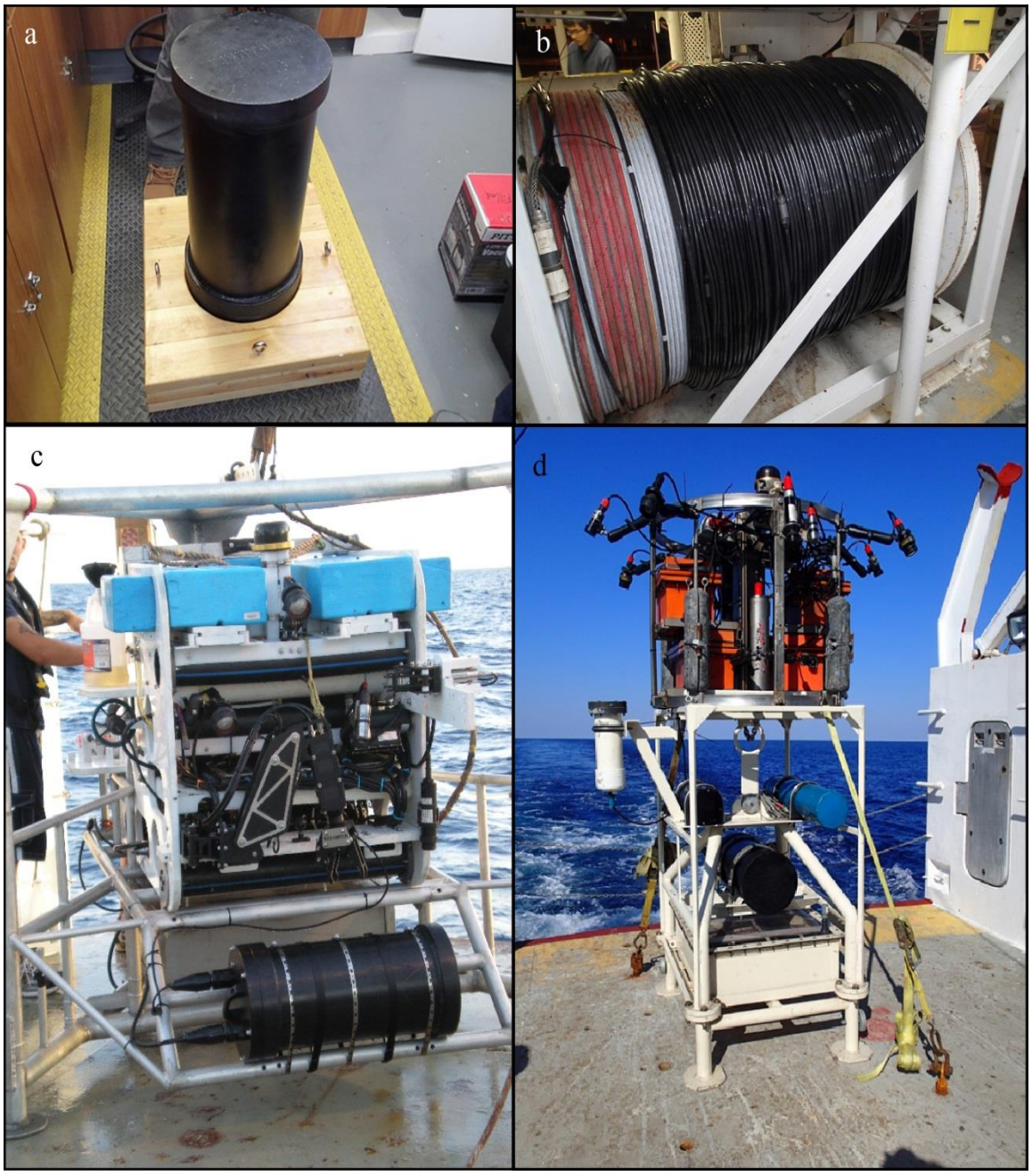


Figure 3.2 Seafloor DCR system. a) Electronic components of the resistivity instrument are contained in a cylindrical pressuring housing. b) 1100-m, 56-electrode array spooled on a winch. c) The pressure housing of the resistivity instrument is attached to the cage of a ROV for the CRP and 2D static survey. d) The pressure housing of the resistivity instrument is installed on the cage of a seafloor lander, with a camera platform attached to the top, for the time-lapse seafloor resistivity survey.

*Study Site*

Woolsey Mound is a gas-hydrate complex 1 km in diameter in the south-central part of Mississippi Canyon Block 118 (MC118), Gulf of Mexico (Figure 3.3). For the past decade, the site has been photographed and sampled by gravity coring, near-bottom multibeam bathymetric profiling, and acoustic subbottom profiling. It also has been investigated by industry 3D seismic data and unconventional surface-source deep-receiver (SSRD) data. The base of the hydrate stability zone (BHSZ) is believed to be shallow (~ 100 m) at this site because of the elevated geothermal gradient caused by focused heat flow above the salt dome and the vertical movement of water from depth.

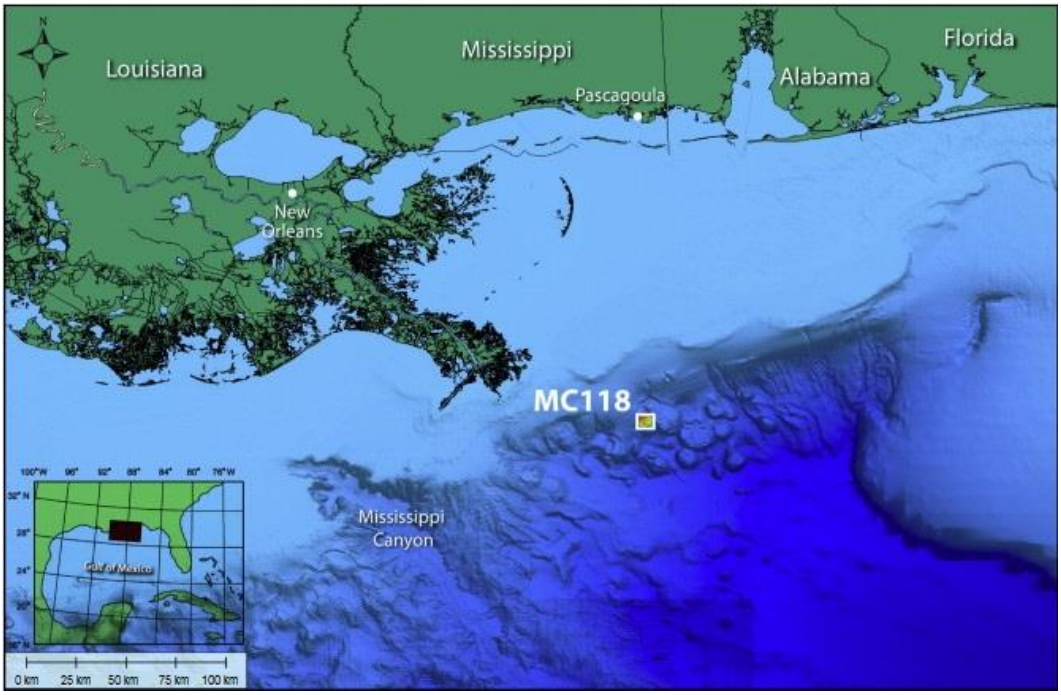


Figure 3.3 Geographic location of Mississippi Canyon Block 118 (MC 118), Gulf of Mexico. Woolsey Mound is located in the south-central portion of MC 118 in 900 m water depth.

*Seafloor CRP Survey*

Seven resistivity profiles totaling 26.4 km in length, spaced approximately 200 m apart, were collected by CRP over Woolsey Mound and adjacent areas in MC 118 in 2009 (Figure 3.4 (a)). Field procedures for collecting seafloor resistivity data using the CRP method are similar to those used for collecting resistivity data in shallow water environments (e.g., Amidu and Dunbar 2008).

In the shallow-water case, the array is towed on the surface of the water directly from the survey vessel. The profile heading is maintained until the array is straight behind the boat, and then resistivity data acquisition is started. The GPS track of the survey vessel is used to reconstruct the locations of the electrode during the survey, assuming that electrodes along the array follow the track of the survey vessel.

For the seafloor resistivity data-acquisition case, first the electrode array is lowered to the bottom, with the ship moving slowly ahead (Figure 3.4c). The ROV is attached to the front of the array and is lowered after the array. Once the ROV is near the bottom, it is towed for at least one array before starting to record data to ensure that the array is relatively straight. Enough cable lead-in is used between the ROV and the active part of the array to ensure that the electrodes were towed along the seafloor. CRP data acquisition is conducted by towing the ROV about 5 to 20 m above the seafloor, with the array trailing behind on the seafloor, while continuously collecting resistivity data. The survey track of the ROV is used to reconstruct the locations of the electrodes during the survey in the same way the vessel track is used in shallow-water surveys.

The example CRP survey at MC118 was collected using consecutive reads of three gradient arrays with source-electrode separations of 220, 440, and 660 m, with eight pairs of receiver electrodes distributed evenly among the source electrodes.

### *Static 2D Seafloor Resistivity Survey*

The field procedure for collecting 2D static seafloor resistivity is similar to that used in collecting CRP data. However, instead of the system being deep-towed above the seafloor while collecting data, the ROV is towed above the seafloor, with the DCR system in standby mode until the array is straight and positioned along the intended profile, with its center location above the target. After the array is positioned, the ROV is lowered to the seafloor. Once the instrument is on the seafloor, communication with the surface vessel is used to start the measurement process, monitor data quality, and retrieve data from the instrument after data acquisition is completed.

For the example survey, four 2D static-resistivity lines were collected over Woolsey Mound in early April 2014, closer to the active vents than in the 2009 survey (Figure 3.4b). Lines 2 and 3 of the 2014 survey were collected in the same areas covered in 2009; however, lines 1 and 4 crossed the east side of the site, between the two most active gas vents.

### *Time-lapse Seafloor Resistivity Survey*

For the time-lapse survey mode, we deploy the instrument attached to a seafloor lander platform so that the array is centered on the predetermined monitoring target. During the monitoring period, the timing unit powers up the control computer and DCR instrument at a designated time interval, sends commands to collect profiles, downloads the resulting data files, erases the DCR instrument's onboard memory, and powers down the instrument and control computer until the next recording cycle. At the end of the monitoring period, the survey vessel retrieves the seafloor DCR system, and the time-

lapse data are downloaded for further processing. This method was used to collect an example two-week time-lapse data set across Woolsey Mound in April 2014.

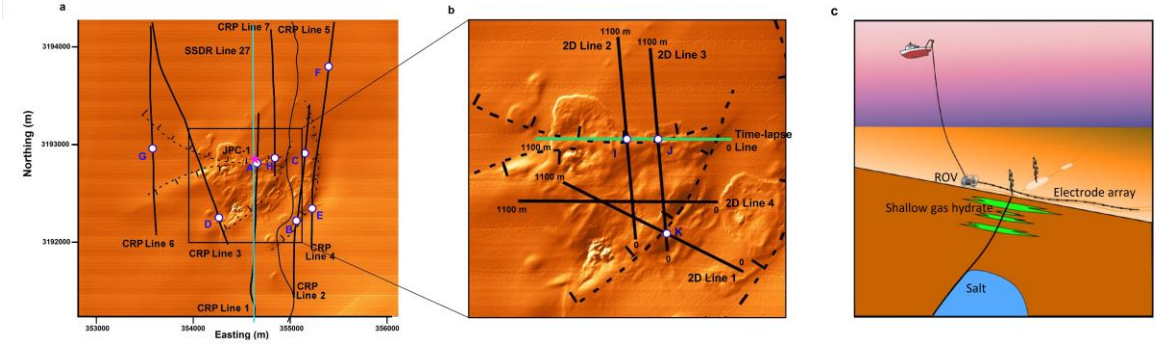


Figure 3.4 Seafloor resistivity profiles collected in MC 118, Gulf of Mexico. Easting and northing coordinates are Universal Transverse Mercator (UTM) zone 16 R. (a) Seafloor CRP survey in 2009. Black curves represent the tracks of seven CRP lines. Blue circles indicate the locations of features on inverted profiles shown in Figure 3.5. The cyan line indicates the SSDR line 27 collected by Macelloni et al. (2012). Dashed lines indicate the approximate traces of faults previously mapped from industry seismic data. (b) 2D static and time-lapse surveys in 2014. Black lines are the tracks of four 2D lines. The red line is the track of the time-lapse line. Blue circles indicate the locations of features on inverted profiles shown in Figure 3.8. Dashed lines indicate the approximate traces of faults previously mapped from industry seismic data. (c) Schematic diagram of the seafloor CRP survey. First the electrode array is lowered to the bottom, with the ship pulling slowly ahead. Then the ROV attached to the front of the array is lowered. Resistivity data acquisition is conducted by deep-towing the ROV about 5 to 20 m above the seafloor with the array trailing behind on the seafloor and continuously collecting resistivity data.

*Data Processing*

A significant amount of preconditioning is performed before the resistivity data are inverted. This is particularly important in the seafloor case, for which the measured voltage levels are lower than for land surveys. First we compute statistics on the average and standard deviation of the raw data for each channel in each array configuration for each line. All readings from channels that do not meet the average apparent-resistivity and standard deviation criteria are removed. Then a second pass is made to filter sporadic outlier readings from otherwise good channels.

The next step is to calculate the geographic coordinates of each electrode during the survey. For the 2D static and time-lapse seafloor resistivity survey, x-, y-coordinates for each electrode are interpolated from the geographic coordinates of the seafloor lander and the last electrode. For the CRP data, we make the assumption that during acquisition, with relatively straight ship tracks, the electrode array follows the path of the ROV along the bottom. Thus the x-, y-coordinates for each electrode are projected onto best-fit straight lines through the profile track line and are exported in terms of 2D distance along the profiles and seafloor topography. The bottom z-coordinate for each x-, y-position along the line then is extracted from an independently collected high-resolution, AUV-based, multibeam bathymetric map of the survey area.

The 2D inversion of CRP and 2D static-resistivity data is carried out by a finite-element inversion program, EarthImager 2D™. The earth model is parameterized as a mesh of rectangular elements. The inversion algorithm attempts to determine the resistivity of the elements that produces agreement between calculated and measured apparent-resistivity values within a specified level of misfit by an iterative forward-

modeling and correction scheme. Because the inverse problem is significantly underconstrained, a smoothness condition is applied so that in eight to 12 iterations, the algorithm seeks the smoothest possible model that explains the data to within a specified misfit.

The methodology adopted for inverting time-lapse resistivity data is similar to that for CRP and 2D static-resistivity data. First, the resistivity data collected at the beginning of the monitoring period, which serve as the reference for the change over time, are inverted by the standard 2D inversion method. Then a difference-inversion algorithm, based on the Occam's inversion technique, is applied to the time-lapse data to minimize the inverted section's difference with respect to the inverted reference model separately at each time step (LaBrecque and Yang, 2001).

### *Results*

Figure 3.5 shows the 2D inverted profiles of the CRP survey. High resistivity anomalies of more than 100 Ωm are observed at two areas on CRP line 1 and line 2 (labeled as A and B in Figure 3.4a), both of which are tens of meters in width and thickness. Both anomalies occur in small pockets near the seafloor, where previously mapped deep-seated normal faults intersect the seafloor. To validate the results of the CRP survey, DCR line 1 is compared with a subparallel shallow-source deep-receiver seismic survey line (Macelloni et al., 2012; Simonetti et al., 2013). The seismic data lack coherent reflection and are dominated by scattered energy from beneath the mound.

The average energy seismic attribute is used to identify zones of high and low scatter beneath Woolsey Mound (Figure 3.6a). Figure 3.6b shows that the broad zone of high scatters beneath the mound corresponds to a zone of intermediate resistivity (1 to 3

Ωm), and the high-resistivity zone (as much as 100 Ωm) corresponds to a small pocket of low scatter within the larger zone of high scatter.

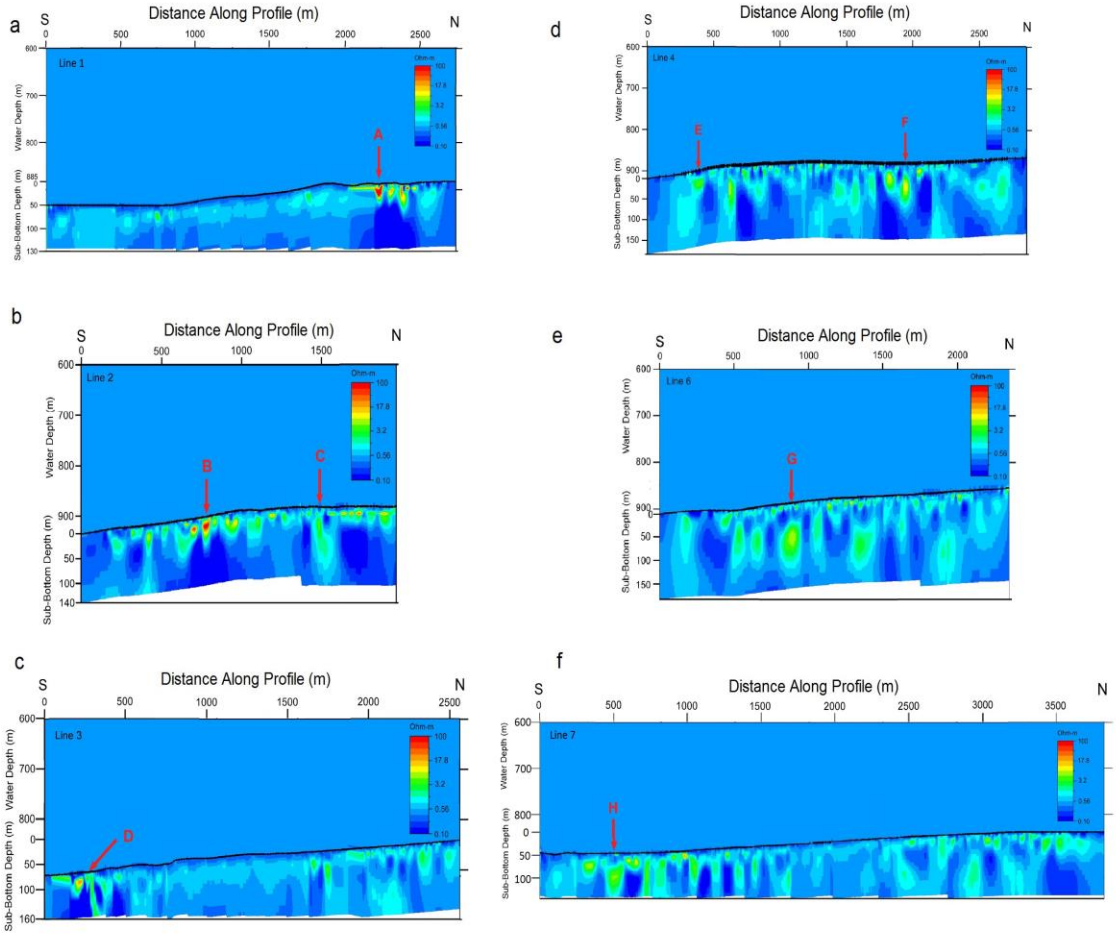


Figure 3.5 Inverted resistivity models for CRP survey in 2009. Figure 3.4 shows the tracks and locations of anomalies.

Jumbo piston cores (Figures 3.7c and 3.7d) collected by Simonetti et al. (2013) also provide ground truth for the resistivity survey interpretation by sampling the sediment in the high-scatter zone on the seismic profile. The sample from Core JPC-1 (Figure 3.4a) at 17-m depth is fine-grained sediment containing free gas and centimeter-

scale angular clasts of hydrate (Figures 3.7c and 3.7d). This sample came from the zone of high scatter on the seismic line and intermediate resistivity on the resistivity line.

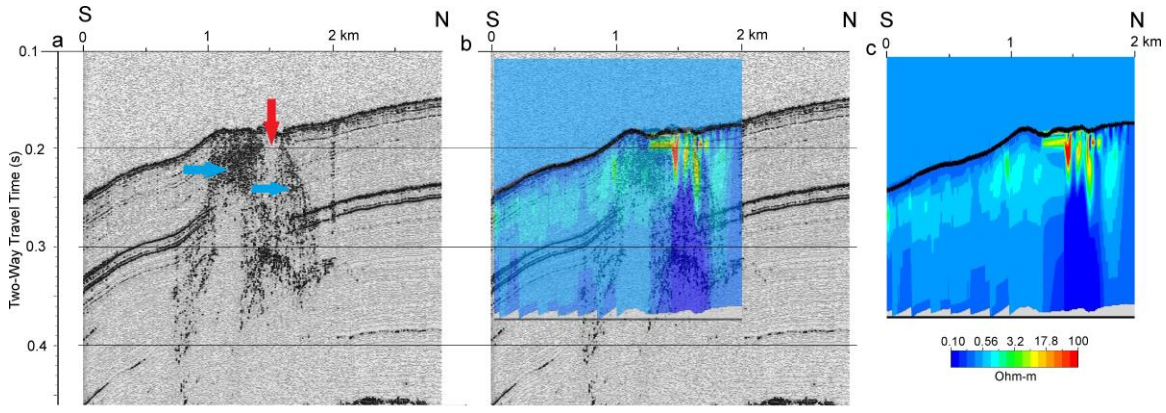


Figure 3.6 Correlation between CRP line 1 and SSDR line 27. (a) Average energy seismic-attribute inline view of SSDR line 27. Blue arrows indicate the high-scatter zone. The red arrow indicates the low-scatter zone. (b)SSDR line 27 average energy attribute line overlaid by the inverted resistivity model of CRP line 1. (c) Inverted resistivity model of CRP line 1.

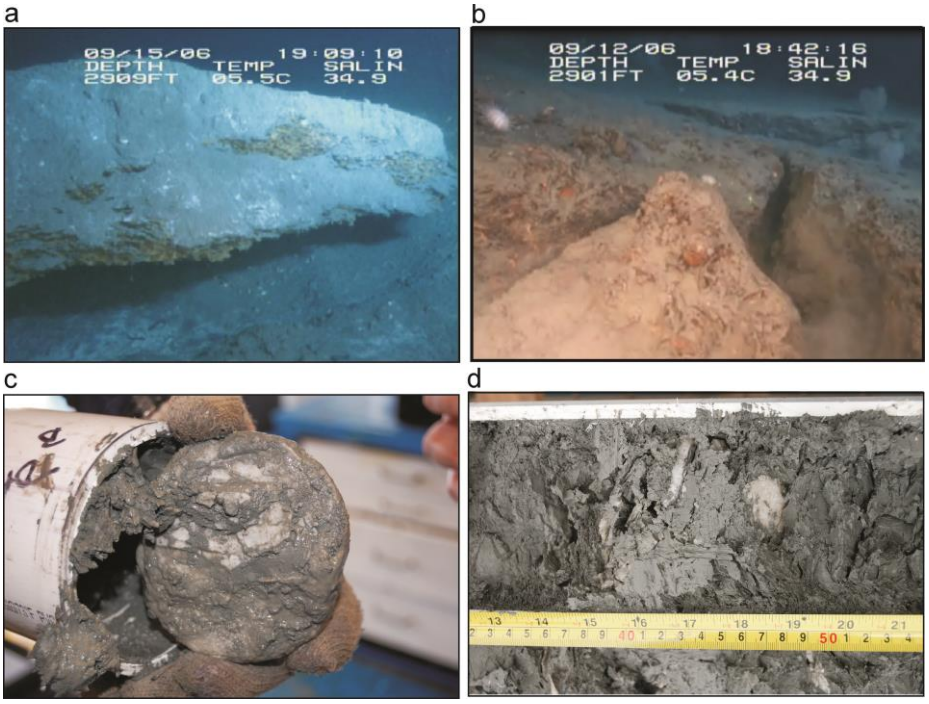


Figure 3.7 Observed materials on the seafloor and shallow subbottom at Woolsey Mound, MC118, Gulf of Mexico. (a) Block of massive hydrate, approximately 1.5 m thick and 5 m long, exposed on the seafloor. (b) Jumble of antigenic carbonate blocks that cap most of the mound. (c and d) Piston-core sample (JPC-1) from areas of high scatter.

In contrast, the small pockets of low scatter correspond to the high-resistivity zone on the resistivity profile. Low-scatter levels within this zone suggest a lack of free gas, whereas high resistivity suggests a high concentration of hydrate. However, the areas of low scatter surrounded by areas of high scatter have not been cored because they occur beneath areas where the bottom is covered by consolidated carbonate that cannot be penetrated by piston cores.

At places where the same fault scarps are crossed at different locations by other CRP lines, the anomalies are also present, but with lower resistivity values. For example, anomalies near the south end of line 7 (labeled as H in Figure 3.4a) and the south end of line 4 (labeled as E in Figure 3.4a) occur along the same fault scarp on which anomalies A and B occur, respectively, but with resistivity values of only as much as 10 Ωm. This indicates that the high-resistivity anomalies indicative of high concentrations of hydrate are distributed along the fault traces. However, there are also anomalies with elevated resistivity values ranging from 3 to 12 Ωm that are not associated with previously mapped faults, such as C, D, G, and F on lines 2, 3, 6, and 4, respectively (Figure 3.4a).

Anomalies with resistivity values ranging from 3 to 12 Ωm have relative high resistivity compared with an average resistivity of 0.66 Ωm for sediments adjacent to the mound. Rather than resulting from high concentrations of hydrate, they most likely are caused in part by the limestone cap (Figure 3.7b), in part by free gas in the sediment, and in part by sediment that contains lower concentrations of hydrate, such as that found in core samples.

Figures 3.8a through 3.8d show the 2D inverted profiles of the 2014 static seafloor resistivity survey. Two of the four lines (lines 2 and 3) collected in the same

areas covered in 2009 show the same pattern of larger and deeper high-resistivity anomalies in the fault zones (labeled as I and J in Figure 3.4b) and a scattering of smaller anomalies in the adjacent shallow subbottom. However, lines 1 and 4, which crossed the east side of the site between the two most active gas vents, contain much larger anomalies.

Line 1 contains a 100-Ωm anomaly 20 m wide and 50 m thick (labeled as K in Figure 3.4b), starting at the 621-m point along the profile. This is the same anomaly as anomaly B along line 2 of the 2009 survey (Figure 3.5b), which occurs along the major down-to-the-north fault along the southern edge of the mound. Line 1 also contains a larger 100-Ωm anomaly, which extends 200 m laterally, from the 320-m point to the 520-m point along the line. The top of the anomaly is 10 to 20 m below the bottom and is as much as 20 m thick in the middle.

Interestingly, the overall shape of this anomaly is concave upward rather than the convex upward shape expected for hydrate pingos (Seri éet al., 2012). Just to the north of this anomaly on line 1, the same anomaly has about the same length but has lower amplitude (5 to 50 Ωm). Hence, the anomaly appears to die out to the north and might be sourced from the gas vent south of line 1. This anomaly occurs beneath a bathymetric bulge, from 5 to 10 m in height on line 1, but does not have a bathymetric expression on line 4. Although this feature is significantly smaller and has a different shape than hydrate pingos observed in other locations, it occurs in the same geologic setting and has all the other hallmarks of hydrate pingos.

Figures 3.8e through 3.8g show the results of time-lapse inversion. Both of the two data sets show the high-resistivity anomaly starting at the 300-m point along the profile, which is the same anomaly as anomaly I along line 2 of the 2014 survey (Figure

3.8b) on the fault zone. In addition, an anomaly with concave shape appears, starting at the 60-m point, which also might be an extension of the anomaly observed on lines 1 and 4. From the percentage-difference profile, we conclude that most of the changes occurred in the fault zone and the apparent hydrate pingos, with changes of as much as 200% in some places.

### *Future Directions*

The work during the last five years at Woolsey Mound, MC 118, demonstrates that the DCR method provides valid data to image resistivity anomalies, characterizing the distribution of shallow gas hydrate and the temporal change of the hydrate system within 100 m of the seafloor, beneath seafloor mounds. Hydrate mounds are inherently 3D features, but the resistivity data collected to date over Woolsey Mound consist of sparse 2D profiles because of limitations in site accessibility and ship time.

These data are sufficient to detect hydrate but are not sufficient to quantify the amount present or to identify the style of hydrate deposit. More closely spaced resistivity lines will be needed to allow 3D inversion of the data to image the geometry of hydrate deposits. Deep piston-core samples will be needed to verify the occurrence of hydrate and to calibrate the resistivity data to allow hydrate volume estimates to be made. Furthermore, a longer-period time-lapse survey will need to be conducted to detect short-term changes in the hydrate system, to understand hydrate formation mechanism in seafloor mounds, and to monitor seafloor instability and fluid/hydrate motion that these changes might produce.

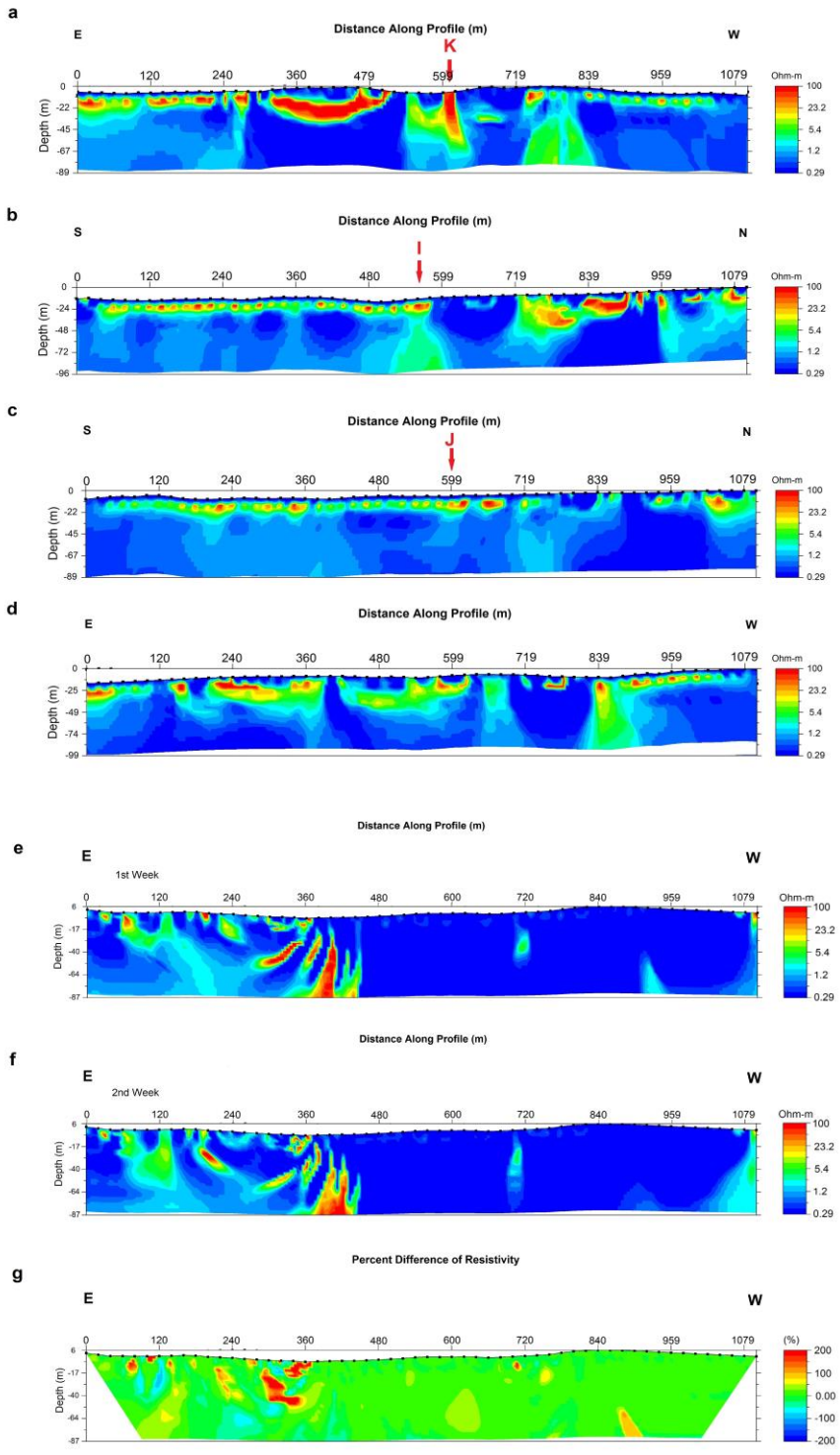


Figure 3.8 Inverted resistivity models for 2D static and time-lapse surveys in 2014. (a) 2D line 1. (b) 2D line 2. (c) 2D line 3. (d) 2D line 4. (e) Time-lapse line for the first week. (f) Time-lapse line for the second week. (g) The percentage of change in resistivity for the time-lapse survey.

One of the geophysical challenges of the DCR system is the low signal level during data acquisition. With seawater resistivity value of about 0.33 Ωm and average near-surface sediment resistivity value of about 1.0 Ωm, voltages measured between potential electrodes are an order of magnitude lower than for land surveys at comparable offsets. However, on the positive side, achieving good electrical contact with the medium, which is the bane of land resistivity work, is not a problem in the marine environment. In addition, electrical noise in the deep-marine environment at frequencies higher than 1 hertz is low because high-frequency electromagnetic noise in the atmosphere is attenuated by the thick seawater layer.

Therefore, boosting the signal level and lowering the noise level from instrument and electrode are important during data acquisition. A low-noise preamplifier could be added to the front end of the array to boost the single level before the signal enters the main housing, where the onboard computer generates radiofrequency noise. A more sophisticated array with replaceable copper source electrodes and titanium or silver–silver chloride receiver electrodes could provide better results.

Together, the preamplifier and improved electrodes should dramatically increase the signal-to-noise ratio and shallow resolution. Moreover, a high-resolution multibeam profiler could be added to the system to record bathymetric information during DCR data acquisition.

## *Conclusion*

Our study at Woolsey Mounds, MC 118, in the Gulf of Mexico can be considered a pilot study of the utility of the DCR method for investigating the deep-marine, near-bottom environment. The results of our study demonstrate that it is possible to collect valid DCR data on the deep-marine environment to detect shallow resistivity anomalies and to map their distribution within 100 m of the seafloor. The results from Woolsey Mound illustrate how seafloor DCR data can be used as a complementary data set to shallow-seismic data to better constrain the near-bottom hydrate distribution. The experimental time-lapse resistivity survey also proves that it can be an effective tool for monitoring long-term changes of near-bottom sediment.

More field trials and laboratory studies will indicate how well this technique will work for problems such as assessment of 3D distribution and temporal changes of near-bottom resistivity anomalies

## *Acknowledgments*

This work has been carried out with the support of Department of Energy. The authors wish to thank the captains and crew of the R/V Pelican, whose skills and effort made for productive cruises.

## *References*

Amidu, S. A., & Dunbar, J. A., 2008, An evaluation of the electrical-resistivity method for water-reservoir salinity studies. *Geophysics*, *73*(4), G39-G49.

LaBrecque, D. J., and X. Yang, 2001, Difference inversion of ERT data: A fast inversion method for 3-D in situ monitoring. *Journal of Environmental and Engineering Geophysics*, 6, no. 2

Macelloni, L., A. Simonetti, J. H. Knapp, C. C. Knapp, C. B. Lutken, and L. L. Lapham, 2012, Multiple resolution seismic imaging of a shallow hydrocarbon plumbing system, Woolsey Mound, northern Gulf of Mexico. *Marine and Petroleum Geology*, 38, no. 1, 128–142

Roy, K. K., 2008, *Potential theory in applied geophysics*. Springer.

Serié, C., M. Huuse, and N. H. Schødt, 2012, Gas hydrate pingoes: Deep seafloor evidence of focused fluid flow on continental margins. *Geology*, 40, no. 3, 207–210,

Simonetti, A., J. H. Knapp, K. Sleeper, C. B. Lutken, L. Macelloni, and C. C. Knapp, 2013, Spatial distribution of gas hydrates from high-resolution seismic and core data, Woolsey Mound, northern Gulf of Mexico. *Marine and Petroleum Geology*, 44, 21–33

# CHAPTER FOUR

## Evaluation of Bedrock Fracture and Soil Cracking on a Vertisol-shale Terrain Using Time-lapse Azimuthal Resistivity Survey

This chapter submitted as: Xu, T., Dunbar, J., & Allen, P. (in review). Evaluation of Bedrock Fracture and Soil Cracking on a Vertisol-shale Terrain Using Time-lapse Azimuthal Resistivity Survey, *Vadose Zone Journal.*

*Abstract*

Cracks within Vertisols soils and joints in underlying bedrock play a crucial role in the water budget of Vertisols-shale terrains. Subvertical joint sets within the bedrock with preferred orientation also result in an anisotropic distribution of electrical resistivity. Cracked soil, on the other hand, exhibits the anisotropy as well as heterogeneous electrical resistivity. Better knowledge of seasonal soil cracking as well as the joints within the bedrock allow better estimates of runoff, storage and recharge, and better agricultural and engineering practices in the expansive soil terrains. We evaluate the time-lapse azimuthal resistivity surveying for characterizing soil cracking and bedrock joint density within a Vertisols-shale terrain. This study demonstrates that surface azimuthal resistivity surveys are an efficient method for quantifying shallow bedrock joints and for monitoring seasonal change in soil cracking. A positive relationship between the measured crack volume and the coefficient of anisotropy in the soil layer area is observed during drying and wetting periods. This indicates the potential of using azimuthal DC resistivity surveys to quantify the soil crack volume. Corroborating information for existence and vertical extent of soil cracks is provided by the homogeneity index, which has previously been used only as an indicator of azimuthal resistivity data quality.

## *Introduction*

Vertisols are a group of soils with high clay content (>30%) that cover about 308 million ha of the global land surface and approximately 12 million ha of the US (Coulombe et al. 1996). Due to their shrink-swell behavior, Vertisols exhibit pronounced change in volume seasonally, develop microtopographical features known as gilgai, and by definition form cracks extending at least 0.5 m deep with apertures of at least 1 cm during the dry seasons. Allen et al. (2005) demonstrated that the water budget in Vertisol-shale terrains is controlled by a complex interaction between the Vertisol soil layer, the underlying jointed bedrock, land use, topography and seasonal change of rainfall and evapotranspiration. More recently the role that soil cracking plays in the exchange of gases between the atmosphere and solid Earth has also been recognized (Weisbrod et al. 2009). Given the important roles that soil cracking and joints within underlying bedrock playing in the water and gas budgets of a Vertisol-shale terrains, there is a need to develop a better understanding of soil cracking during the seasonal wetting and drying cycles and to joints within the underlying bedrock.

Amidu and Dunbar 2007 studied spatial patterns of seasonal moisture changes in Vertisol soil using time-lapse DC electrical resistivity profiling at the USDA-ARS Grassland, Soil and Water Research Laboratory experimental watershed facility, near Riesel, TX. A key finding of this study was that in terms of average moisture distribution the Vertisol soils at the Blackland site can be divided into three distinct layers. There is a surficial layer extending from the surface to a depth of 0.5 m that has relatively low average moisture continent, a middle layer (horizon) from 0.5 to 1.1 m that is relatively saturated, and a deeper layer from 1.1 to at least 1.4 m within the soil that is less saturated

than the middle layer. The upper layer acts as the interface between the atmosphere and deeper soil layers and undergoes the most dramatic seasonal wetting and drying. The saturation of the middle layer is enhanced by bypass flow through cracks that form in the upper layer and end at the top of the middle layer. Amidu and Dunbar (2007) speculated that the preferential wetting of the middle soil layer via cracks through the upper layer cause the middle layer to swell more than the dryer layers above and below and that it is this differential swelling that drives the dynamic processes that ultimately produce the complex internal structure and microtopography associated with Vertisol soils.

The 2007 study by Amidu and Dunbar had two important limitations. First, the continuum electrical resistivity tomography method they used was not suited to imaging discrete cracks. Hence, the presence of open cracks and the depth to which they extend in different parts of the soil profile at different times was indirectly inferred from the regions of abnormally high resistivity and the time rate of change of resistivity of parts of the soil profile in response to rainfall. Second, the recording geometry used to collect their resistivity profiles was designed for maximum resolution with the upper most 1.4 m of the soil profile. However, the soil at the site is approximately 2 m thick. As a result, they had no information about the lower-most part of the soil profile and the underlying bedrock, which play a key role in recharge. In the current study we fill this information gap by conducting a 10-month, time-lapse azimuthal resistivity survey at the same site studied by Amidu and Dunbar (2007). Azimuthal resistivity surveys are conducted by collecting directional resistivity data around the compass rose, centered at a single surface point. These surveys are used to infer the vertical change in the electrical resistivity anisotropy, which occurs in response to fractures and other linear features in

the vertical plane. The results allow us to indirectly monitor the vertical opening and closing of soil cracks throughout the soil profile and to verify the presence and orientation of joints in the underlying bedrock. This demonstrates for the first time a way to connect the complex soil zone to the underlying bedrock aquifer, thereby enhancing our understanding of how and when recharge occurs.

### *Background: Azimuthal Resistivity Method*

An azimuthal DC resistivity survey is a modified 2D resistivity survey used to measure the azimuthal variation of electrical resistivity. Azimuthal surveys are conducted by rotating a linear electrode array through 180 degree (or 360 degree), typically in constant angular increments and taking measurements in each position (Taylor & Fleming 1988). For the past few decades, the azimuthal DC resistivity method has been applied to different subsurface problems, such as determining fracture orientation (Boadu et al. 2005; Busby & Jackson 2006), characterize jointed systems (Taylor & Fleming 1988), and estimating hydraulic transmissivity (Ritzi & Andolsek 1992).

Many different electrode-array configurations have been used to collect azimuthal resistivity data. Collinear, four-electrode arrays, such as the Wenner and Schlumberger arrays, have been used to measure anisotropy in various studies (Taylor & Fleming 1988; Leonard-Mayer 1984; Ritzi & Andolsek 1992). A number of non-linear arrays have also been used to increase the sensitivity to anisotropy, such as the square array (Habberjam & Watkins 1967), the equatorial dipole array (Semenov 1975), and the arrow-type array (Bolshakov et al. 1998). Electrode offsets within collinear arrays are changed in order to achieve different effective depth of investigation (Edwards 1977). Also, the difference between measurements of the same collinear array at different location is related to the

inhomogeneity and can be used to differentiate the heterogeneity and anisotropy (Watson & Barker 1999; Busby 2000).

For a homogenous medium, the apparent resistivity is the same for two measurements of electrode arrays of the same type and length, centered at different locations along a given azimulathal line. However, the two measurements tend to differ in a heterogeneous medium (Watson & Barker, 1999). Busby (2000) developed a quantitative measure of heterogeneity in azimuthal resistivity surveys based on the difference between apparent resistivity measurements from arrays with centers shifted one-half of an electrode spacing to either size of the survey axis. Following Busby (2000), a homogeneity index *H* was calculated by

$$H = \frac{\sigma(\rho_{e1,}\rho_{e2})}{\sigma(|\rho_{e1} - \rho_{e2}|)}, \qquad (4.1)$$

where $\rho_{e1}$ and $\rho_{e2}$ are the apparent resistivities measured with the same array center at symmetric locations to either side of the survey axis, e1 and e2, $\sigma(\rho_{e1}, \rho_{e2})$ is the standard deviation of the measurements for all of the azimuthal orientations, and $\sigma(|\rho_{e1} - \rho_{e2}|)$ is the standard deviation of the absolute difference between the measurements for all the azimuthal orientations. A value of *H* larger than unity suggests that the azimuthal variation of apparent resistivity due to anisotropy is greater than that due to spatial heterogeneity and vice versa. Busby (2000) suggested that azimuthal surveys for which $H<1$ should be interpreted with caution, if at all.

Habberjam (1972) and Lane et al. (1995) used polar plots of azimuthal apparent resistivity data to estimate the direction and degree of anisotropy graphically. In their analysis, if there was a distinct ellipsoidal shape of the polar plot, it was interpreted to

indicate the present of transverse anisotropy. For cases involving fractures, the major axis of the ellipse was interpreted to be coincident with the direction of the fractures, due to the paradox of anisotropy (Keller & Frischknecht 1966). Separate, best-fitting ellipses of apparent resistivity have also been calculated for each depth of investigation based on a least square fitting method (Figure 4.1; Gander et al. 1994). This approach provides a quantitative assessment of the direction as well as the strength of anisotropy. To determine if statistically significant transverse anisotropy was present, Hart & Rudman (1997) used a measure of the goodness-of-fit to an elliptical model to the azimuthal data. The $R^2$ for the elliptical fit is defined by

$$R^2 = \frac{\sigma_{data}^2 - \sigma_{residual}^2}{\sigma_{data}^2}, \qquad (4.2)$$

where $\sigma_{data}^2$ is the variance of the azimuthal apparent resistivity and $\sigma_{residual}^2$ is the variance of the residuals between the data and the constructed best-fitting ellipse from the previous step. A $R^2$ value near unity indicates a good fit to the elliptical model, whereas a $R^2$ value significantly less than unity suggests otherwise.

In a transversely anisotropic medium, the apparent resistivity depends on the orientation of the measurement relative to the axis of anisotropy. The apparent resistivity measurements made longitudinal to the plane of anisotropy (parallel to bedding), are always the largest, whereas transverse measurements made in the plane of anisotropy (normal to bedding), are always the smallest. Because this is counter to intuition, it is referred to as the paradox of anisotropy (Keller & Frischknecht 1966). Two fracture parameters are extracted directly from best-fitting ellipses. The orientation $\theta$ of the major axes of the best-fitting ellipses are calculated and interpreted as the orientation of the

fractures. The ratio of the length of the two major axes is assumed to be related to fracture density. This parameter, referred to as the coefficient of anisotropy $\lambda$, is defined by

$$\lambda = \frac{\rho_{x_{app}}}{\rho_{y_{app}}}, \tag{4.3}$$

where $\rho_{x_{app}}$ and $\rho_{y_{app}}$ are the apparent resistivities along the major and minor axes of the best-fitting ellipse of apparent resistivity, respectively.

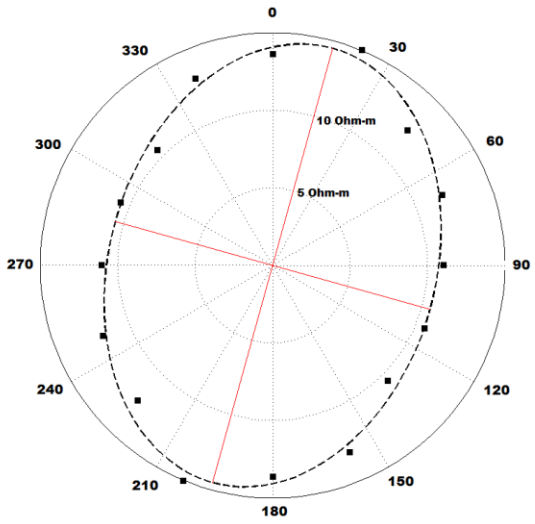


Figure 4.1 An example of the best-fitting ellipse of the azimuthal resistivity data from Site A. Radial axis is in Ohm-meters. Square is the collected azimuthal resistivity data and dash line is the best-fitting ellipse to the data. Two red lines is the major axis and minor axis of the best-fitting ellipse.

*Synthetic Model Study*

We conduct an initial synthetic model study to evaluate the effectiveness of the azimuthal resistivity method for determine anisotropy in both cracked soil and jointed bedrock. Synthetic data over models containing virtual cracks and joints are generated to simulate surface azimuthal DC resistivity surveys. A 3D finite element forward model is used to solve Poisson's equation for voltage at receiver electrode locations in response to current injected between source electrode locations. Synthetic apparent resistivity data for the 3D model are generated for groups of virtual source and receiver electrodes to simulate a range of dipole-dipole array lengths, centered on the axis of the virtual survey. The electrode locations are rotated in constant angular increments around the axis to simulate azimuthal surveys.

The meshed volume of the synthetic models is 73 m×73 m×20 m in the X, Y, and Z directions, respectively (Figure 4.2). To simulate intact soil and bedrock, the background resistivity is set to 10 ohm-meters. The mesh design is tested to insure numerical error of no more than 1%, by comparing the results for a homogenous finite element model without cracks or fractures to that of the analytical solution for the same electrode configuration on a homogenous half space. Vertical, non-conductive fractures are created in the synthetic model by breaking the electrical continuity between elements within the finite element mesh over the extent of the fracture surfaces in the XZ or YZ planes. Because fractures in the near surface are normally filled with air, which is essentially non-conductivity, no specific fracture aperture can be assigned. For air-filled fractures, the impedance to electrical current increases with the surface area of the fracture, but is independent of the fracture aperture. To simulate a heterogeneous cracked

soil, an orthogonal fracture set is inserted into the part of the model. Elements within the mesh are also divided along parallel surfaces in the lower part of the model to simulate jointed bedrock (Figure 4.3).

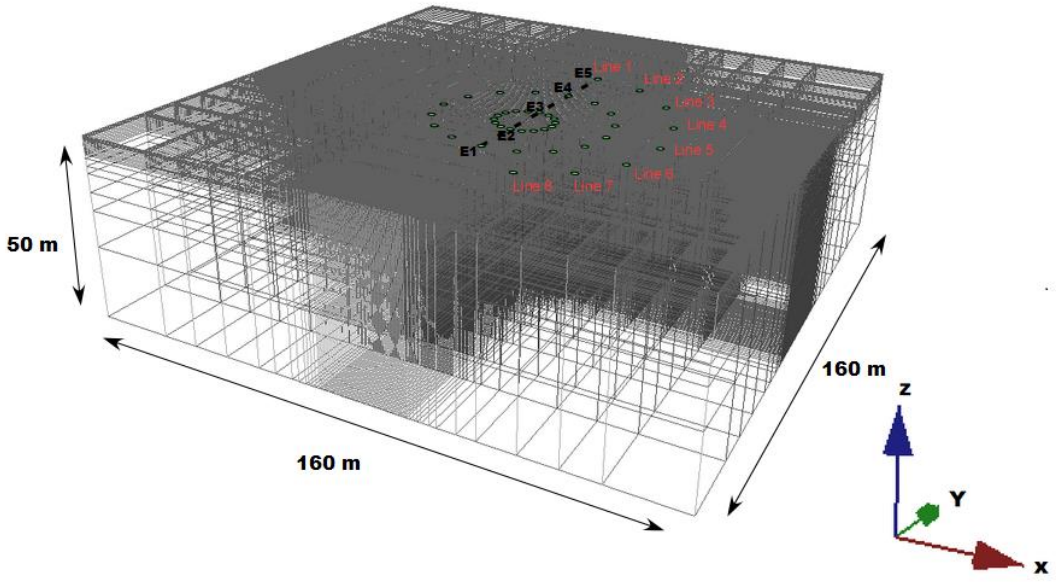


Figure 4.2 Synthetic model. The meshed volume of synthetic model was 73 m ×73 m ×20 m in the X, Y, and Z direction respectively. The surrounding background was set as 10 ohm-meters. Five-electrode collinear arrays were placed in the center of the model to calculate the homogeneity index H. The virtual survey line was progressively rotated at 22.5 degree increments around a common center point between electrode E2 and E3.

To simulate azimuthal surveys, five-electrode arrays are initially placed in the center of the model to calculate the apparent resistivity in an initial orientation that would be measured in response to the assigned fracture distribution. Electrode offsets are varied from 4 m to 9 m to achieve effective depths of investigation from 1.7 m to 3.7 m within the model. The virtual survey line is then progressively rotated in 22.5 degree increments around a common center point. The modeled apparent resistivity values are perturbed by adding 2% random noise to each virtual measurement, to simulate realistic field results.

Values of the homogeneity index H, and the coefficient of anisotropy $\lambda$, are calculated for each array length from the simulated apparent resistivity measurements.

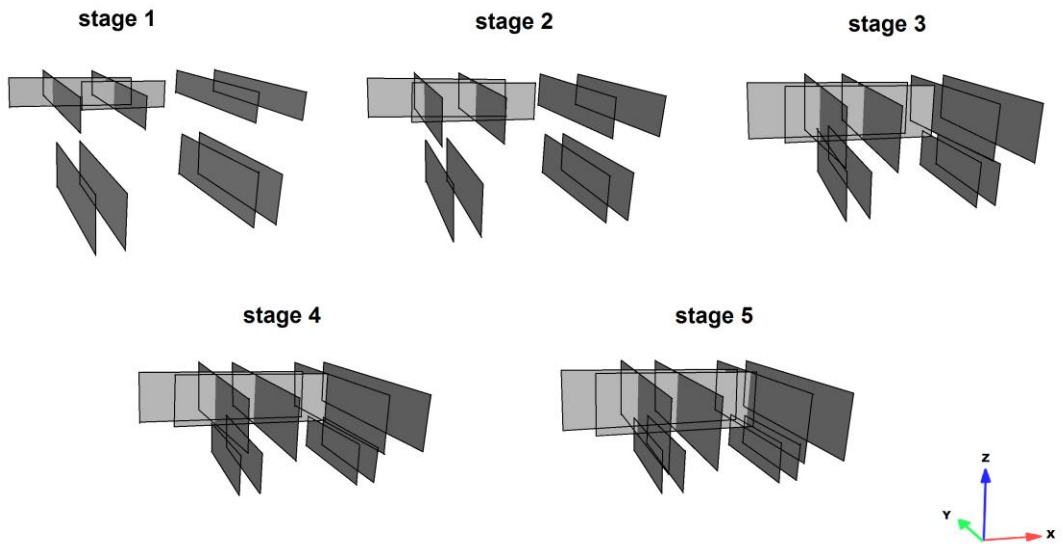


Figure 4.3 Synthetic study. Non-conductive fractures were created in the middle of synthetic model in the XZ and YZ planes (Figure 4.2). Fracture surface area increases from 165 $m^2$ for stage 1 to 492 $m^2$ for stage 5

A time-lapse azimuthal resistivity survey is simulated in this study by changing the length and vertical extent of the cracks in 5 stages. In Stage 1, 6 soil cracks are present in the crack-affected zone, each with the length of 6.5 m and extend from the surface to a depth of 1 m. The combined surface area of the cracks is 165 $m^2$. In order to simulate the seasonal growth of soil cracks, both the length and depth of the cracks is increased from Stage 1 through 5, simulating an increase in the combined crack surface area from 165 $m^2$ to 492 $m^2$. Four parallel fractures are present in the joint-affected zone with the length of 6 m and depth of 2 m. Since bedrock joints are less affected by seasonal change, their geometry is kept the same for the joint-affected zone. A vertical profile of homogeneity index *H* is calculated for each effective depth of investigation in

the 5 stages to evaluate the vertical variation between anisotropy and heterogeneity over time. Separate best-fitting ellipses of apparent resistivity are calculated for each depth of investigation to extract the apparent fracture orientation and coefficient of anisotropy.

## *Field Study*

### *Study Site*

The field study site is at the USDA-ARS Grassland, Soil and Water Research Laboratory experimental watershed facility, near Riesel, TX (Figure 4.4). This research site is located in the Texas Blackland Prairie. The 340 ha site is divided into several sub-watersheds, ranging from 0.1 to 125 ha, which are under mixed pasture and cropland management. The dominant soil is Houston Black clay soil; fine, montmorillonitic, thermic Udic-Ustic Haplusters (Miller & Greenwade 2001). The typical particle size distribution of Houston Black soil is 17% sand, 28% silt and 55% clay. It exhibits shrink-swell behavior on a seasonal basis. The soil layer ranges from a thickness of 0.9 m on the hill slope to 3.0 m on the valley bottom. Microtopographical gilgai features are well developed on the study site. Intense cracking occurs during summers, with the depth of cracks reaching up to 4 m.

The top stratum at the site is a layer of chalk belonging to the Pecan Gap Member of the Taylor Group of the Gulfian series, with the thickness about 4.0 m. Underlying the Pecan Gap chalk is the Wolfe City Member of the Taylor Group, which locally consists of silty marl grading into sandy marl. In the study site, the uplands and upper slopes are underlain by the Pecan Gap Member, whereas the lower slopes and valley bottoms are underlain by the Wolfe City Member. The bedrock in the study area can be generally

divided into three depth zones: there is an uppermost oxidized zone, a transition zone, and an unoxidized zone. In the oxidized zone, the bedrock is highly weathered, ranging from 1.2 to 1.5 m thick on the hillslope to more than 6.1 m on the valley bottom. Core and outcrop data indicate that the oxidized zone has a relatively high joint density, ranging from approximately 5 to 17 joints per meter (Alexander 1998).

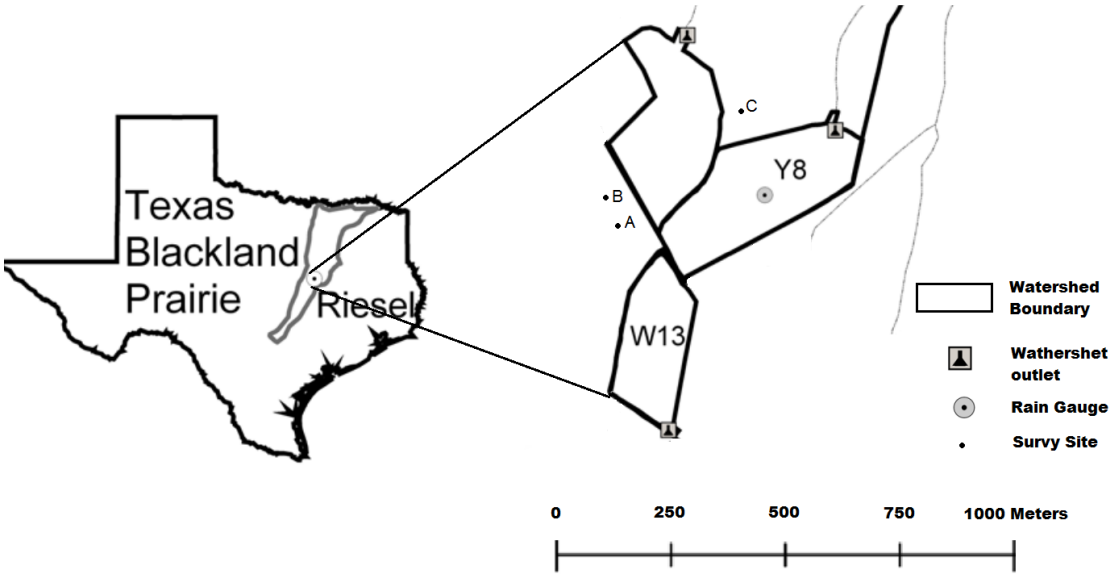


Figure 4.4 Study sites on Grassland, Soil and Water Research Laboratory Watersheds, Riesel, TX

*Field Data Acquisition*

Azimuthal DC resistivity surveys are conducted at sites A, B and C within the USDA-ARS Grassland, Soil and Water Research site (Figure 4.4). Site A was the location of the study conducted by Amidu and Dunbar (2007). All three sites are in areas under pasture management. Sites A, and B, are located on the drainage divide and have not undergone cultivation in historic times (Figure 4.5). Site C is on the valley slope, also in an area currently under pasture management, but has historically been cultivated. Sites A

and B, exhibit well developed micro-low and micro-high gilgai structures as well as deep soil cracks during dry periods. However neither gilgai nor deep cracks are observed at Site C. The Pecan Gap Chalk forms the underlying bedrock at sites A and B, which has a higher joint density than the underlying bedrock Wolf City silty marl (Blank et al. 1952). Therefore, Site C serves as a control group since it has low predicted soil heterogeneity and bedrock anisotropy. A 10-month time lapse survey is conducted to monitor soil anisotropy over a cycle of wet to dry and back to wet conditions.

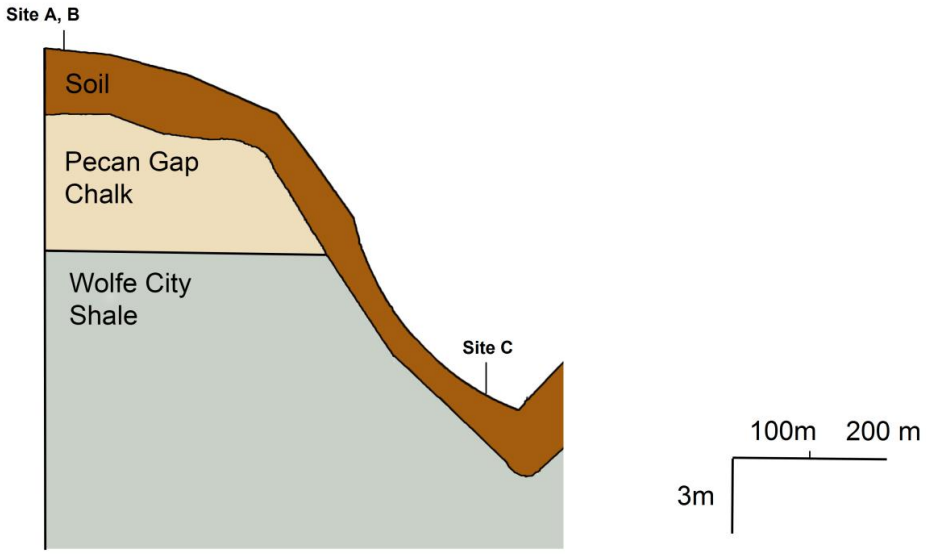


Figure 4.5. Geologic cross section for study sites.

A SuperSting R8, multi-channel resistivity meter is used to carry out the azimuthal surveys (Advanced Geosciences 2011). The system consists of a portable, eight-channel meter, 28 stainless steel electrodes connected to a multi-conductor cable. During the surveys, the 28-electrodes are placed on a collinear array with 1-m electrode spacing. The cable is progressively rotated at 22.5 degree increments around a common

center point, to collect 8 2D lines. The dipole–dipole array is used due to its low electromagnetic coupling and high sensitivity to horizontal changes (Dahlin & Zhou 2004). Individual readings are made with four-cycle stacking, with a 2% max error threshold to ensure data quality. A collinear azimuthal seismic refraction survey is also acquired at Site A to provide supplementary information of bedrock depth. A 24 channel, seismograph is used to record the data, with 24 geophones spaced 1 m apart along the same 22.5 degree azimuthal lines. Reverse profiles are collected at each orientation, to account for any dip in the bedrock surface.

*Data Processing*

For each rotation of the DC resistivity azimuthal surveys, 237 apparent resistivity readings are collected. Resistivity profiles are inverted by the finite element method in order to estimate the depth to bedrock. The results are validated by the seismic refraction survey. Among the 237 apparent resistivity readings, 16 pairs of readings have dipoles positioned symmetrically about the common center point. These 32 symmetrical readings are analyzed to produce the vertical anisotropy profiles. The effective depth of investigation for each azimuthal resistivity survey is estimated using the method of Edwards (1977). At each location, different electrode spacings vary the median depth of investigation from 0.42 m to 5.94 m. The homogeneity index H, the statistic $R^2$, orientation $\theta$, and the coefficient of anisotropy $\lambda$, are calculated for each effective depth interval.

## *Results*

### *Synthetic Model Results*

Figure 4.6 shows the vertical profiles of the homogeneity index, anisotropy orientation and coefficients of anisotropy from Stage 1 to 5, for the combined soil crack and bedrock joint models. The responses from crack-affected zone (surface to 3 m effective depth) and joint-affected zone (3 to 5 m effective depth) differ significantly. The crack-affected zone is less homogenous, with the homogeneity index smaller than 1 (Figure 4.6a). However, the joint-affected zone is more homogenous, with the homogeneity index larger than 1. The growth of crack surface area is produced by increasing crack density, depth and length, resulting in f a more extensive crack network. This further reduces the homogeneity index from Stage 1 to 5. The simulated orthogonal crack network in the crack-affected zone also shows a positive relationship between the change of coefficients of anisotropy and the crack surface area change from Stage 1 to 5 (Figure 4.6b). However, for the joint-affected zone, the coefficients of anisotropy for all the effective depth intervals are almost constant. The growth of crack area creates a large deviation of best-fitting ellipses, resulting in calculated anisotropy orientations pointing in markedly different directions (Figure 4.6c). However, the calculated anisotropy orientations in the joint-affected zone are relative constant, ranging from -6.0 ° to 6.4 °, which is close to initial direction of 0 °, as expected.

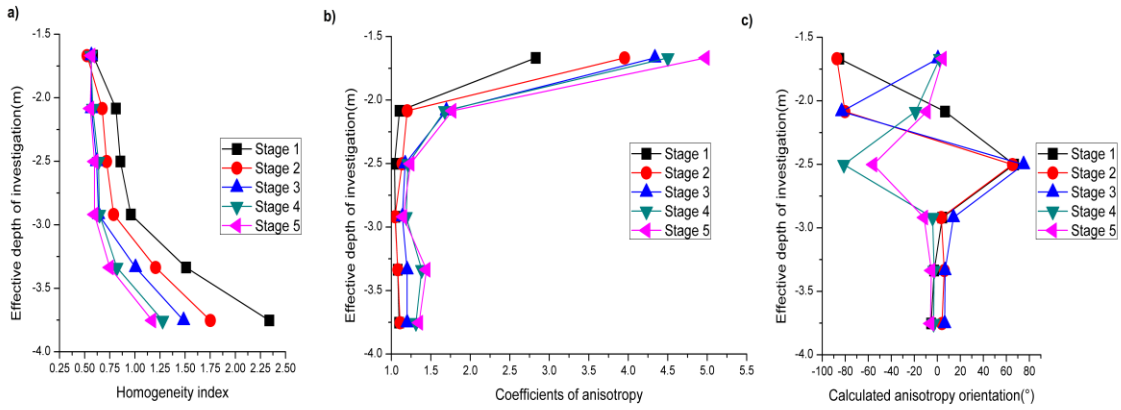


Figure 4.6 Results of the synthetic study. a) Change of the homogeneity index from stage 1 to 5. b) Change of coefficients of anisotropy from stage 1 to 5. c) Calculated anisotropy orientation from stage 1 to 5.

*Field Study Results*

*Data quality control.* Calculated vertical homogeneity indices for Site A, B and C are tabulated in Table 1. The seismic refraction survey confirmed that the depth of bedrock is about 2.3 m at the survey site. Therefore, for effective depth from surface to 2.4 m, the anisotropy is interpreted to be the result of cracks within the soil layer and for effective depth below 2.4 m as the result of joints within the bedrock. For effective depths of investigation from 3.0 to 5.2 m, all the data have homogeneity indices larger than 1, with an average value of 1.66. The bedrock is then classified as anisotropic and homogeneous, by the method of Busby (2000), since the anisotropic azimuthal variation exceeds the dispersion introduced by inhomogeneity. We interpret this to be the result of joints within the bedrock that have lengths and consistent orientations over distances that are long, relative to the array lengths. However, for the investigation depth interval from 0.7 to 2.4 m, more than 90 % of data have homogeneity indices smaller than 1, with an average value of 0.60. Homogeneity indices this low indicate that the anisotropic

homogenous effect is significantly less than influences from heterogeneity within the soil layer. This is in accordance with the explanation by Samouelian et al. (2004) that cracked soil as a whole is heterogeneous, due to the irregular geometry of soil crack networks. However, over the time-lapse study the homogeneity index rises and falls within the soil layer and has different values at different depths within the soil over time. Rather than being a sign of poor data quality, we interpret the seasonal variations in the homogeneity index to be the result of changing saturation levels and associated opening and closing of cracks at different depths within the soil in different seasons.

For all the resistivity data, the calculated $R^2$ of for the elliptical fit ranges from 0.45 to 0.96 with an average of 0.78. For about 90% of data, the $R^2$ is larger than 0.6. $R^2$ generally increases with increasing depth of investigation, reflecting the overall tendency of increasing electrical anisotropic in the bedrock. Only the data with $R^2$ greater than 0.6 are used for further evaluation of transverse anisotropic properties.

*Soil layer.* The orientation of greatest resistivity varies significantly for different depth intervals within the soil and with season for the same depth intervals. The uppermost interval of the soil (from the surface to 0.7 m) has the highest standard deviation of the coefficient of anisotropy, with a maximum standard deviation of 0.345 (Figure 4.7b). Also, the uppermost interval has the highest coefficient of anisotropy, with the highest value up to 2.07 in the driest month, August 2015 (Figure 4.7a). At this same time, the homogeneity index is low throughout the soil layer, suggesting that open soil cracks extend from the surface to the base of the soil at this time (Figure 4.8a). This contrasts with virtually no anisotropy, with the lowest coefficient of anisotropy of 1.02, in the wettest month, June, 2015 (Figure 4.8b, Figure 4.9). At this same time, the

homogeneity index reaches a peak value greater than 1.0 in the middle of the soil layer, which suggests that the soil cracks are closes in the middle of the soil layer at this time (Figure 4.9).

Table 4.1 Seasonal and spatial variation of homogeneity index for Site A, B and C.

| Homogeneity Index | | | | | | | | | |
|---|---|---|---|---|---|---|---|---|---|
| | Site A | | | | | | Site B | Site C | Anisotropic response |
| Effective depth(m) | Mar-15 | Apr-15 | Jun-15 | Aug-15 | Nov-15 | Jan-16 | June-15 | June-15 | Heterogeneous |
| -0.417 | 0.75 | 0.67 | 0.54 | 0.47 | 0.77 | 0.62 | 0.77 | 0.57 | |
| -0.696 | 0.72 | 0.46 | 0.47 | 0.33 | 0.65 | 0.43 | 0.63 | 0.46 | |
| -1.218 | 1.07 | 0.99 | 1.17 | 0.24 | 0.58 | 0.74 | 0.48 | 0.99 | |
| -1.728 | 0.67 | 0.43 | 0.32 | 0.51 | 0.58 | 0.51 | 0.31 | 0.43 | |
| -2.24 | 0.59 | 0.77 | 0.30 | 0.34 | 0.31 | 0.39 | 0.91 | 0.77 | |
| -2.436 | 1.33 | 1.28 | 1.02 | 0.70 | 1.22 | 1.64 | 3.52 | 0.78 | |
| -2.954 | 1.59 | 1.89 | 1.50 | 1.38 | 1.74 | 1.23 | 2.13 | 1.89 | |
| -3.456 | 1.15 | 2.00 | 1.08 | 1.59 | 1.66 | 1.62 | 1.21 | 2.00 | |
| -3.96 | 1.35 | 1.00 | 1.67 | 1.82 | 1.55 | 1.56 | 3.08 | 1.00 | Homogeneous |
| -4.48 | 1.12 | 1.61 | 2.72 | 2.04 | 1.60 | 2.03 | 2.12 | 1.61 | |
| -5.184 | 1.65 | 1.07 | 1.82 | 1.17 | 1.85 | 1.32 | 3.06 | 1.07 | |

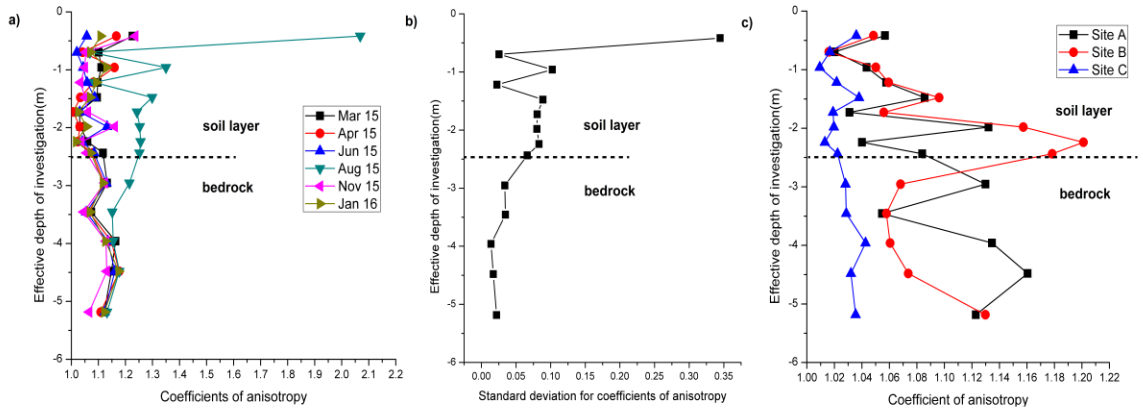


Figure 4.7 Vertical variations of coefficients of anisotropy in study sites. a) Seasonal change of coefficients of anisotropy on Site A. b) Standard deviation of coefficient of anisotropy for the seasonal change of the coefficient of anisotropy on Site A. c) The coefficient of anisotropy on Site A, B and Site C at June 2015.

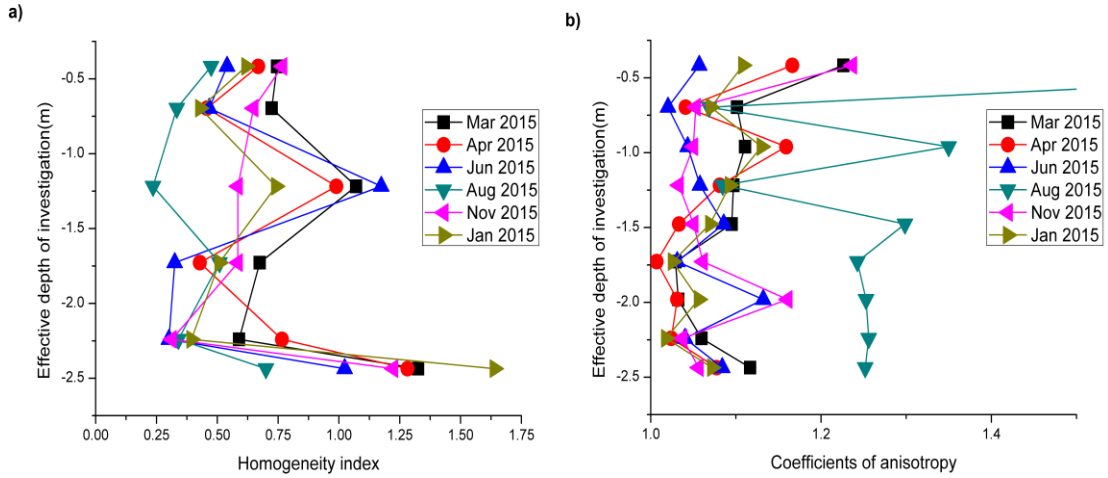


Figure 4.8 Seasonal change of anisotropy parameters in soil layer of Site A. a) Seasonal change of homogeneity indices in the soil layer of Site A. b) Seasonal change of coefficients of anisotropy in the soil layer of Site A.

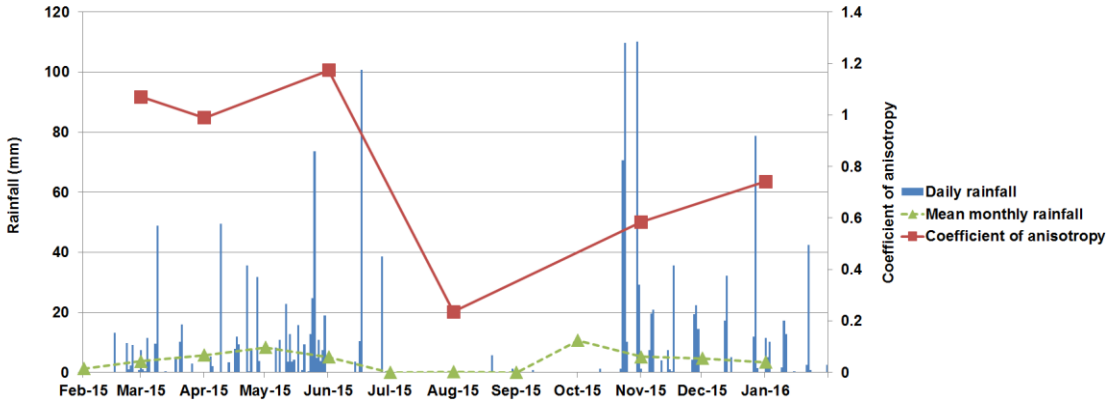


Figure 4.9 Relationship between rainfall distribution during the period of study and calculated homogeneity indices of a middle layer of the soil layer from 0.5 to 1.1 m.

*Bedrock.* Polar plots of azimuthal apparent resistivity data of Site A, B, and C for the bedrock are shown in Figure 4.10. For the control group Site C, anisotropy ellipses are not observed for the bedrock, with only homogenous resistivities (circular azimuthal patterns) observed. This may indicate that the underlying Wolfe City shale is isotropic due to the lack of joints. It is also possible that the soil layer is sufficiently thick beneath Site C that the resistivity survey did not penetrate to the bedrock in this location. For the Site A and B, anisotropy ellipses are observed for almost all the effective depth intervals within the bedrock. The directions of the major axes of the ellipses indicate the anisotropy orientation and the ratio of axes lengths indicate the degree of anisotropy. It is apparent that the anisotropic responses are variably dependent on the effective depth of investigation within the bedrock. For the shallow bedrock, the maximum anisotropic response trends E-W direction. However, the anisotropy ellipses rotate clockwise with increasing depth. At the deepest depth of investigation, the orientation of major axis is N-S. Also, the same pattern, in which the orientation of greatest resistivity gradually rotates from E-W direction to N-S direction with increasing depth, is repeated in the

time-lapse azimuthal resistivity surveys for Site A. Spatial variability of anisotropy can be observed by comparing results from Site A and Site B on June 15. Both the orientation and degree of anisotropy are different between the two sites; however the differences are relatively small. Figure 4.11a summarizes the temporal variation of anisotropy orientation for Site A from best-fitting ellipses. For the same effective depth of investigation, the seasonal change in orientation is relative low. However, the orientation has a large variation with depth, rotating from NW to NE direction, ranging from an average of 276 °, at effective depth of 2.4 m, to an average of 5.53 ° at 5.2 m. Figure 4.11b indicates that the orientation of greatest resistivity varies from about 280 ° to 13 °, with increasing depth at Site B.

The seasonal variation of the coefficient of anisotropy for the bedrock at Site A is shown in Figure 4.7a. The standard deviation for coefficient of anisotropy ranges from 0.014 to 0.034, indicating a relative small seasonal variation of anisotropy during the wetting and drying cycle in the Pecan Gap formation (Figure 4.7b). By comparison to the isotropic control group Site C, Site A and Site B have significant higher coefficients of anisotropy for the bedrock depth interval (Figure 4.7c).

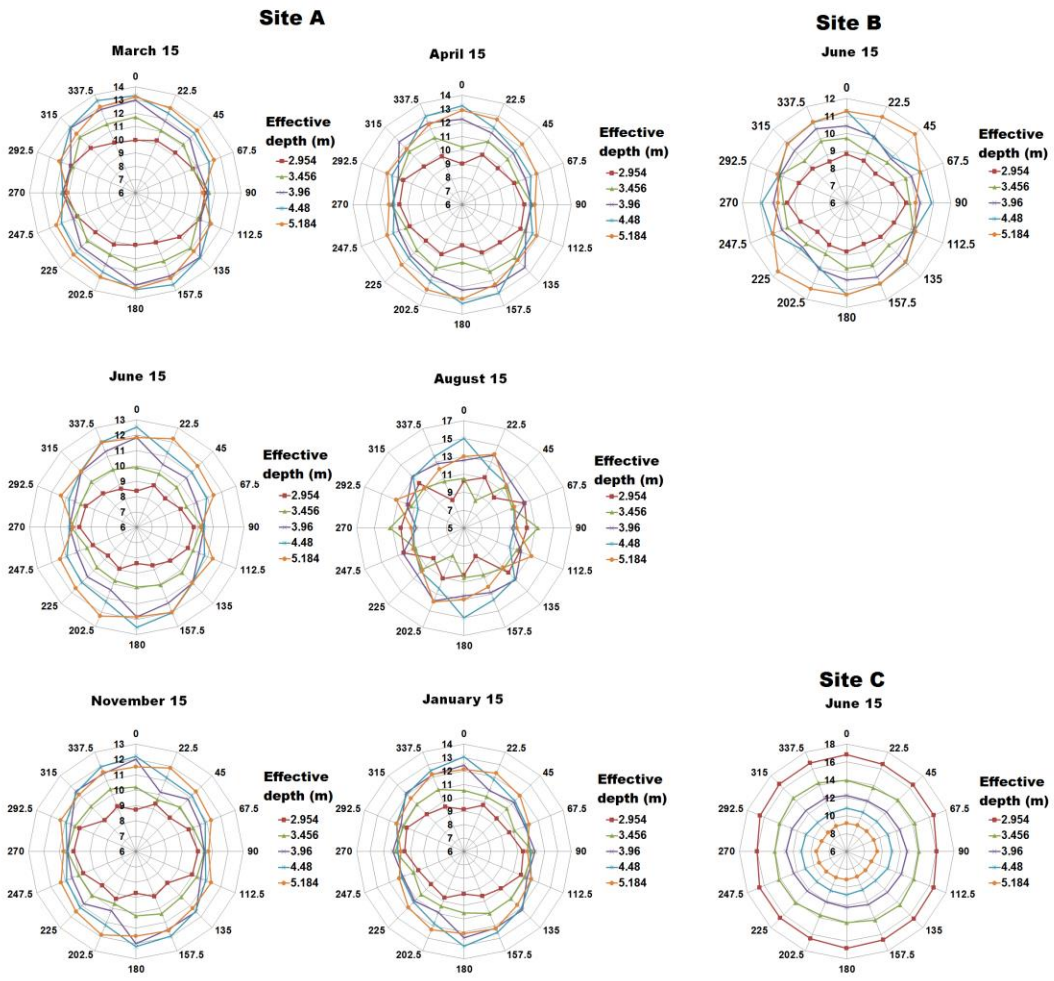


Figure 4.10 Polar plots of azimuthal resistivity measurements for bedrock layer collected at Site A, Site B and Site C (control group).

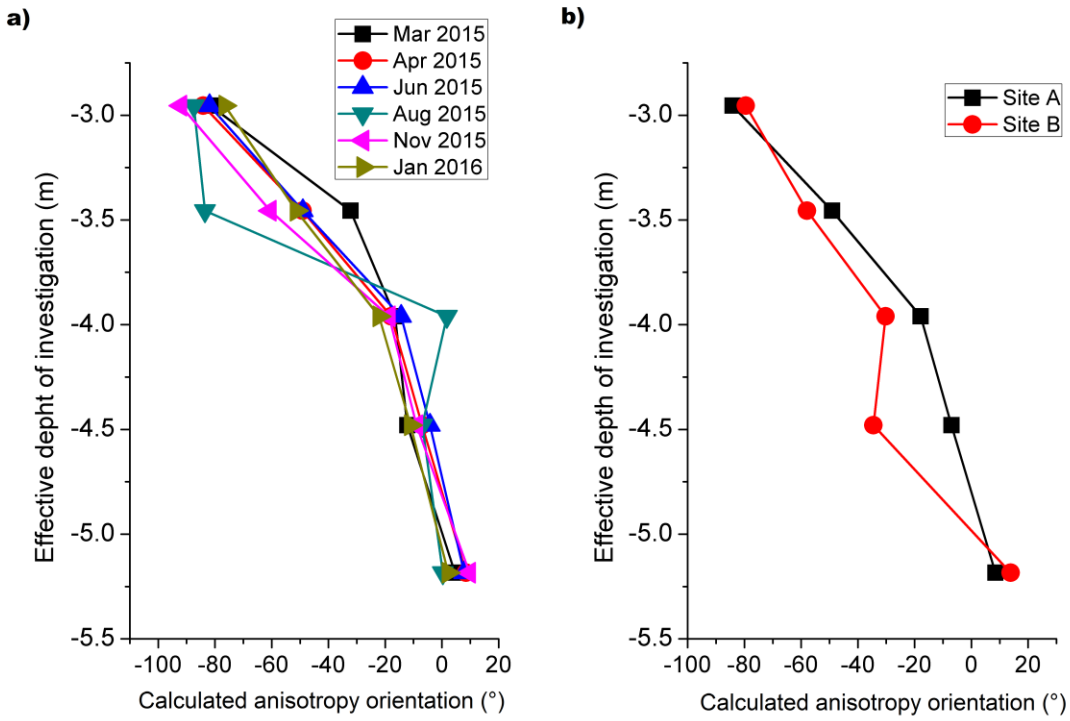


Figure 4.11 Seasonal change of calculated degree of greatest anisotropy for Site A. b) Spatial difference of calculated degree of greatest anisotropy between Site A and Site B

*Discussion*

The results of the model and field studies both indicate the collinear DC resistivity azimuthal surveying is a useful method to evaluate both soil cracks and bedrock joints in a Vertisol-shale terrains. Temporal, spatial and vertical variation of anisotropy parameters can be obtained from collinear azimuthal surveys. The model study shows that changing fracture surface area causes significant change in the coefficient of anisotropy of the fractured medium. Although cracked soil is heterogeneous due to its irregular crack network, soil cracks still cause a directional dependence of resistivity. Therefore, a positive relationship between crack surface area and the coefficient of anisotropy is expected. One of the surprising results of this study is the that the homogeneity index *H*, which is normally used as check on data quality, is

shown to correlate to changes in the density of complex crack networks as well as the anisotropy. In the model study we find that as the surface area increases within a complex crack network, the anisotropy coefficient increases and the homogeneity index decreases. The two parameters are computed from different aspects of the resistivity data. The anisotropy coefficient is a function of the variation of with resistivity direction, whereas the homogeneity index is a function of the spatial rate of change of resistivity. The fact that these two parameters are based on different properties of the subsurface resistivity and yet both change systematically with crack density means that their agreement provides corroborating evidence for the presence or absence of open soil cracks.

Results from the field study also show that there are consistent relationships between soil cracking and coefficient of anisotropy and the homogeneity index. The seasonal variation of the coefficient of anisotropy for the entire soil profile is obtained by averaging the value of $\lambda$ for the effective depth of investigation interval 0.4 m to 2.4 m. It is compared with prior results of crack volume at the same site, measured by the soil anchor method (Arnold et al. 2005; Allen et al. 2005). Figure 4.12a shows the relationship between the calculated coefficient of anisotropy and measured crack volume and it clearly shows a positive relationship between them during the drying and wetting periods. An inverse relationship between the coefficient of anisotropy and rainfall is observed in Figure 4.12b. Based on the rainfall distribution during the period of study, there are two wetting cycle and one drying cycle from March 2015 to January 2016. From the first wetting cycle February 2015 to May 2015, the rainfall water flowing down the cracks and causes swelling of the soil, closing the soil cracks gradually until the beginning of the dry cycle. This period corresponds to a decrease of the coefficient of

anisotropy. From the drying cycle July 25 to October 15, 2015, surface soils are observed extensively cracked in the study site with the depth more than 4 m. Previous data shows the maximum crack volume approaches 120 mm and over 90% of the crack volume occurred in the upper 1.2 m (Arnold et al. 2005). The increased coefficient of anisotropy indicates the soil crack volume dramatically increases during the drying period. From the second wetting cycle November 2015 to January 2016, the low evapotranspiration and continued rainfall close the soil crack gradually again, corresponding to the drop of coefficient anisotropy. The fact that there is virtually no anisotropy when the cracks are closed in the wettest months indicates that all of this anisotropy is attributable to the development of cracks.

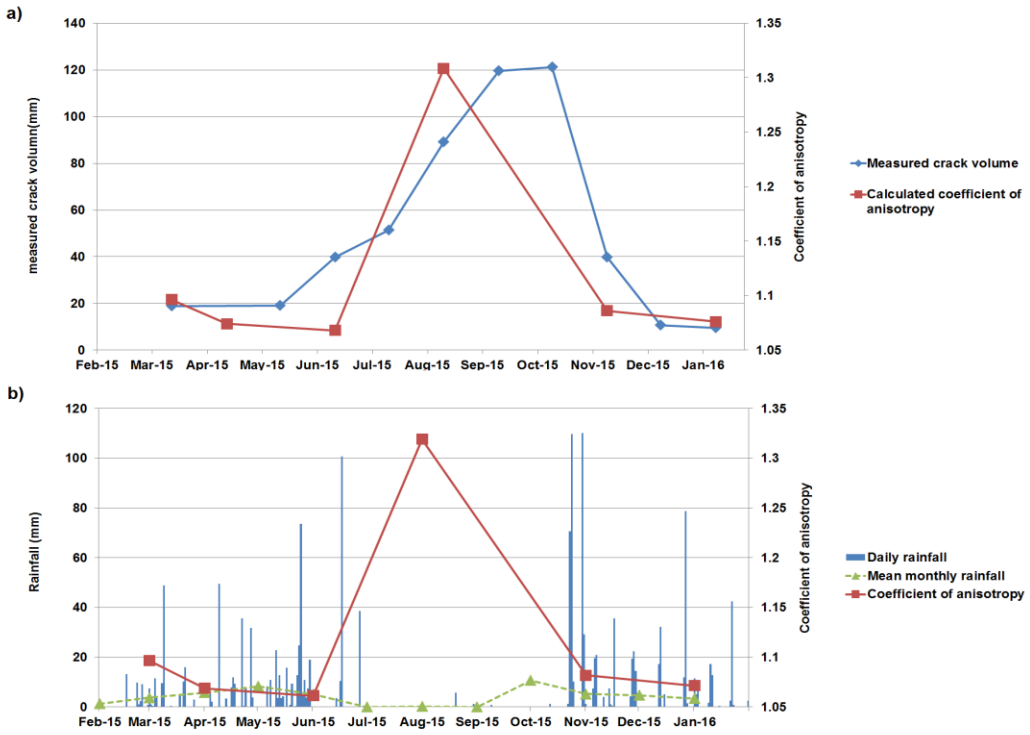


Figure 4.12 a) Relationship between measured crack volume and calculated coefficient of anisotropy for the soil layer. b) Relationship between rainfall distribution during the period of study and calculated coefficient of anisotropy.

Opposite correlation occur between rainfall and homogeneity index. Figure 4.9 shows the relationship between the seasonal change in the homogeneity index at the mid-soil depth and rainfall. The seasonal variation of the homogeneity index within the soil shows high homogeneity throughout the soil during wet months, with the highest value reached in the wettest month of June, 2015, and low homogeneity during dry months, with the lowest value reached in driest month of August, 2015.

The details of the seasonal variation of anisotropy and homogeneity with depth in the soil suggest that during dry seasons the soil develops cracks that extend from the surface to at least the middle of the soil layer and perhaps to base of the soil (Figure 4.8a and 4.8b). At the onset of the subsequent wet season, water flows rapidly through these open cracks, some of which likely passes directly through the soil cracks and into joints in the underlying bedrock to recharge the ground water. With continued precipitation, the mid-soil interval wets preferentially until the cracks in the mid-soil close, forming a hydraulic barrier that prevents further rapid recharge. In this sense, the mid-soil layer acts as a valve that opens during dry seasons, allowing recharge to occur, and then progressively closes during the subsequent wet season. This conceptual model of recharge through Vertisol soils is consistent with that proposed by Allen et al. (2005), which was based on observations of the water level response to rainfall in different seasons. Allen et al. (2005) observed that the most rapid water level rise typically occurred on the second significant rainfall event after a prolonged dry interval. Allen et al. (2005) speculated that the rapid recharge event was due in part to the existence of open, deep cracks through the soil layer. Their explanation for the most rapid recharge occur in response to the second rainfall was that the rainfall from the first event was largely

absorbed by the dry soil lining the crack wall and only after this initial wetting could further rainfall flow through the cracks unabated. The results of the current study support their hypothesis with evidence that the soil cracks open and close as suggested.

In this study, results are sufficient to qualitatively evaluate the seasonal change of soil cracking but not sufficient to quantify the soil crack density over time. This limitation is due to the fact that the electrical properties of non-conductive cracks correlated directly to crack surface area, rather than to crack volume. Once an air-filled crack opens, its electrical properties do not chance significantly with increasing aperture, but only change with surface area. Given knowledge of the mechanical properties of the soils involved, it could be possible to correlate crack area with crack volume. Such a calibration was not attempted in the current study.

The synthetic study demonstrates that the observed anisotropy orientation can accurately predict the joint orientation in bedrock. From the vertical profile of calculated anisotropy, the model study showed a relative constant orientation for different depth intervals with the joint-affected zone that agreed with the orientation of the synthetic fractures. However, for the field survey, the anisotropy orientation rotates from E-W direction to N-S direction with increasing depth into the bedrock. The regional joint study of Bell county, TX by Alexander (1998) indicates subvertical joints with a general N-S trend. The anisotropy orientation for deeper effective depth in the current study agrees with Alexander's results. However there is a large discrepancy between the results for shallow effective depths within the bedrock and the mapped joint strikes. The rotating anisotropy orientation is possibly due to the joints in the uppermost Pecan Gap, which is a highly weathered zone. It is possible that clay-filled joints within this highly weather

zone cause the shift of the anisotropy orientation. Another, more likely possibility, is that the measurement of the orientation of joints in the uppermost interval of the bedrock is influenced by anisotropy due to the soil cracks directly on top of the bedrock. The smearing of the two orientations is a result of the fact that the apparent resistivity for an effective depth of investigation is a weighted average of ground resistivities above that depth. One possible way to avoid or at least limit this smearing of anisotropy results over depth intervals would be to perform a 2D inversion of the resistivity data for each orientation in the azimuthal survey, prior to azimuthal interpretation.

### *Conclusion*

Vertisols soil cracks and underlying bedrock joints play an important role in the water budget of Vertisols-shale terrain. In this study, collinear azimuthal DC resistivity is used to characterize the anisotropy in the Vertisols-shale terrain. It is demonstrated that vertical profiles of anisotropy have the potential to verify the existence and orientation of both soil cracks and bedrock joints. A positive relationship between the measured crack volume and coefficient of anisotropy in the soil layer area observed during the drying and wetting periods. The results indicate a potential of using azimuthal DC resistivity survey to quantify the soil crack volume. Corroborating information for existence and vertical extent of soil cracks is provided by the homogeneity index, which has previously been used only as an indicator of azimuthal resistivity data quality.

The time-lapse azimuthal DC resistivity survey conducted in this study provided evidence that, during prolonged dry periods soil cracks open and extend at least to mid-soil depths and perhaps to the soil base and then progressively close during the following wet period. This suggests that recharge is more efficient for precipitation events that

closely follow prolonged dry intervals, as apposed those that occur during prolonged wet intervals.

## *References*


Advanced Geosciences, 2011. Instruction Manual for SuperSting Earth Resistivity, IP & SP system & Powersting External High Power Transmitters.

Alexander, R., 1998. *Shallow fracture characteristics of the Ozan Formation, Bell County, Texas*. Baylor University, Waco, TX.

Allen, P.M. et al., 2005. Field data and flow system response in clay (vertisol) shale terrain, north central Texas, USA. *Hydrological Processes*, 19(14), pp.2719–2736.

Amidu, S. a. & Dunbar, J. a., 2007. Geoelectric Studies of Seasonal Wetting and Drying of a Texas Vertisol. *Vadose Zone Journal*, 6(3), p.511.

Arnold, J.G. et al., 2005. Estimation of soil cracking and the effect on surface runoff in a Texas Blackland Prairie watershed. *Hydrological Processes*, 19(3), pp.589–603.

Blank, H.R., Stoltenberg, N.L. & Emmerich, H.H., 1952. *Geology of the Blacklands Experimental Watershed , Near Waco , Texas*,

Boadu, F.K., Gyamfi, J. & Owusu, E., 2005. Determining subsurface fracture characteristics from azimuthal resistivity surveys: A case study at Nsawam, Ghana. *Geophysics*, 70(5), p.B35.

Bolshakov, D.K. et al., 1998. New Step in Anisotropy Studies : Arrow-Type Array . In *4th EEGS*.

Busby, J. & Jackson, P., 2006. The application of time-lapse azimuthal apparent resistivity measurements for the prediction of coastal cliff failure. *Journal of Applied Geophysics*, 59(4), pp.261–272.

Busby, J.P., 2000. The effectiveness of azimuthal apparent-resistivity measurements as a method for determining fracture strike orientations. *Geophysical Prospecting*, 48(4), pp.677–695.

Coulombe, C.E., Dixon, J.B. & Wilding, L.P., 1996. Mineralogy and chemistry of Vertisols. *Developments in Soil Science*, 24, pp.115–200.

Dahlin, T. & Zhou, B., 2004. A numerical comparison of 2D resistivity imaging with 10 electrode arrays. *Geophysical Prospecting*, 52(5), pp.379–398.

Dudal, R. & Eswaran, H., 1988. Distribution, properties and classification of Vertisols. *Vertisols: Their distribution, properties, classification and management*, pp.1–22.

Edwards, L.S., 1977. A modified pseudosection for resistivity and IP. *Geophysics*, 42(5), pp.1020–1036.

Gander, W., Golub, G.H. & Strebel, R., 1994. Least-squares fitting of circles and ellipses. *BIT Numerical Mathematics*, 34(4), pp.558–578.

Habberjam, G.M., 1972. The Effects of Anisotropy on Square Array Resistivity Measurements. *Geophysical prospecting*, 20(2), pp.249–266.

Habberjam, G.M. & Watkins, G.E., 1967. The use of a square configuration in resistivity prospecting. *Geophysical prospecting*, 15(3), pp.445–467.

Hart, D. & Rudman, A.J., 1997. Least-squares fit of an ellipse to anisotropic polar data: Application to azimuthal resistivity surveys in karst regions. *Computers & Geosciences*, 23(2), pp.189–194.

Keller, G.V. & Frischknecht, F.C., 1966. Electrical methods in geophysical prospecting.

Lane, J.W., Haeni, F.P. & Watson, W.M., 1995. Use of a Square-Array Direct-Current Resistivity Method to Detect Fractures in Crystalline Bedrock in New Hampshire. *Ground Water*, 33(3), pp.476–485.

Leonard-Mayer, P.J., 1984. *A surface resistivity method for measuring hydrologic characteristics of jointed formations*, US Dept. of the Interior, Bureau of Mines.

Miller, G.B. & Greenwade, J.M., 2001. Soil Survey of McLennan County, Texas.

Ritzi, R.W. & Andolsek, R.H., 1992. Relation between anisotropic transmissivity and azimuthal resistivity surveys in shallow, fractured, carbonate flow systems. *Ground Water*, 30(5), pp.774–780.

Samouelian, A. et al., 2004. Three-dimensional crack monitoring by electrical resistivity measurement. *European Journal of Soil Science*, 55(4), pp.751–762.

Semenov, A.S., 1975. Rock anisotropy and electrical fields peculiarities in anisotropic media. *Vestnik of Leningrad university*, pp.40–47.

Taylor, R.W. & Fleming, A.H., 1988. Characterizing Jointed Systems by Azimuthal Resistivity Surveys. *Ground Water*, 26(4), pp.464–474.

Watson, K.A. & Barker, R.D., 1999. Differentiating anisotropy and lateral effects using azimuthal resistivity offset Wenner soundings. *Geophysics*, 64(3), pp.739–745.

Weisbrod, N. et al., 2009. Falling through the cracks: The role of fractures in Earth-atmosphere gas exchange. *Geophysical Research Letters*, 36(2), pp.1–5.

# CHAPTER FIVE

## Conclusion

This research project explores the effectiveness of the DCR method on three different challenging geological settings. Results of the DCR applied to water reservoir, deep marine and anisotropic ground are presented. In the first study, we propose a binning method for irregularly spaced CRP data, based on the inverse-distance weighted interpolation method. The binning method provides a 2-D interpolator for the irregularly distributed data sets and combines multiple 2D CRP profiles to produce a data set suitable for 3D inversion using widely available programs. Compared to the traditional sparse-profile 2D CRP survey, the 3D inversion with the help of binning technique has clear advantages, gleaning more information about the water body and sub-bottom.

The deep-marine, near bottom represents a relatively more challenging environment for DCR method. In the second study, we adapt a conventional engineering-scale DCR survey system for use on the deep seafloor. The new DCR system is used first in CRP mode to conduct a reconnaissance survey of the mound and its surroundings. Next, the system is used in the static-array mode to identify targets for long-term monitoring. The results of our study demonstrate that it is possible to collect valid DCR data on the deep-marine environment to detect shallow resistivity anomalies and to map their distribution within 100 m of the seafloor. More field trials and laboratory studies will indicate how well this technique will work for problems such as assessment of 3D distribution and temporal changes of near-bottom resistivity anomalies.

The DCR method is applied to an anisotropic ground in the third study. In this study, we evaluate the time-lapse azimuthal resistivity surveying for characterizing soil cracking and bedrock joint density within a Vertisols-shale terrain. This study demonstrates that surface azimuthal resistivity surveys are an efficient method for quantifying shallow bedrock joints and for monitoring seasonal change in soil cracking. A positive relationship between the measured crack volume and the coefficient of anisotropy in the soil layer area is observed during drying and wetting periods. Corroborating information for existence and vertical extent of soil cracks is provided by the homogeneity index, which has previously been used only as an indicator of azimuthal resistivity data quality. This indicates the potential of using azimuthal DC resistivity surveys to quantify the soil crack volume.

# REFERENCES


Advanced Geosciences Incorporated, 2006, *Instruction manual for EarthImager 2D*. Advanced Geosciences, Inc., Austin, Texas.

Advanced Geosciences Incorporated, 2006, *Instruction manual for EarthImager 3DCL*. Advanced Geosciences, Inc., Austin, Texas.

Advanced Geosciences, 2011. Instruction Manual for SuperSting Earth Resistivity, IP & SP system & Powersting External High Power Transmitters.

Alexander, R., 1998. *Shallow fracture characteristics of the Ozan Formation, Bell County, Texas*. Baylor University, Waco, TX.

Allen, P.M. et al., 2005. Field data and flow system response in clay (vertisol) shale terrain, north central Texas, USA. *Hydrological Processes*, 19(14), pp.2719–2736.

Amidu, S. a. & Dunbar, J. a., 2007. Geoelectric Studies of Seasonal Wetting and Drying of a Texas Vertisol. *Vadose Zone Journal*, 6(3), p.511.

Amidu, S., and Dunbar, J., 2008, An evaluation of the electrical-resistivity method for water-reservoir salinity studies. *Geophysics*, 73(4), G39-G49.

Arnold, J.G. et al., 2005. Estimation of soil cracking and the effect on surface runoff in a Texas Blackland Prairie watershed. *Hydrological Processes*, 19(3), pp.589–603.

Ball, L. B., W. H. Kress, and J. C. Cannia., 2006, Determination of canal leakage potential using continuous resistivity profiling techniques in western Nebraska and eastern Wyoming. In *Proceedings of SAGEEP*, Seattle.

Bartier, P. M., and Keller, C. P., 1996, Multivariate interpolation to incorporate thematic surface data using inverse distance weighting (IDW). *Computers & Geosciences*, 22(7), 795-799.

Becker, E. B., Carey, G. F., and Oden, J. T., 1981, *Finite Elements, An Introduction, Volume 1*. Prentice Hall, Englewood Cliffs, New Jersey, 107-109.

Belaval, M., Lane Jr, J. W., Lesmes, D. P., and Kineke, G. C., 2003, Continuous-resistivity profiling for coastal groundwater investigations: three case studies. In *Proceedings of SAGEEP,* San Antonio, 397-410.

Blank, H.R., Stoltenberg, N.L. & Emmerich, H.H., 1952. *Geology of the Blacklands Experimental Watershed , Near Waco , Texas*,

Boadu, F.K., Gyamfi, J. & Owusu, E., 2005. Determining subsurface fracture characteristics from azimuthal resistivity surveys: A case study at Nsawam, Ghana. *Geophysics*, 70(5), p.B35.

Bolshakov, D.K. et al., 1998. New Step in Anisotropy Studies : Arrow-Type Array . In *4th EEGS*.

Briggs, I. C. 1974, Machine contouring using minimum curvature. *Geophysics*, 39(1), 39-48.

Busby, J.P., 2000. The effectiveness of azimuthal apparent-resistivity measurements as a method for determining fracture strike orientations. *Geophysical Prospecting*, 48(4), pp.677–695.

Busby, J. & Jackson, P., 2006. The application of time-lapse azimuthal apparent resistivity measurements for the prediction of coastal cliff failure. *Journal of Applied Geophysics*, 59(4), pp.261–272.

Cordell, Lindrith E., 1992, A scattered equivalent-source methods for interpolation and gridding of potential-field data in three dimensions. *Geophysics*, 57(4), 629-636.

Coulombe, C.E., Dixon, J.B. & Wilding, L.P., 1996. Mineralogy and chemistry of Vertisols. *Developments in Soil Science*, 24, pp.115–200.

Dahlin, T. & Zhou, B., 2004. A numerical comparison of 2D resistivity imaging with 10 electrode arrays. *Geophysical Prospecting*, 52(5), pp.379–398.

Dahlin, T., and Loke, M. H., 1997, Quasi-3D resistivity imaging-mapping of three dimensional structures using two dimensional DC resistivity techniques. *3rd EEGS Meeting*.

Dampney, C. N. G., 1969, The equivalent source technique. *Geophysics*, 34(1), 39-53.

Day-Lewis, F. D., White, E. A., Johnson, C. D., Lane Jr, J. W., and Belaval, M., 2006, Continuous resistivity profiling to delineate submarine groundwater discharge—Examples and limitations. *The Leading Edge*, 25(6), 724-728.

Dey, A., and Morrison, H. F., 1979, Resistivity modeling for arbitrarily shaped three-dimensional structures. *Geophysics*, 44(4), 753-780.

Dudal, R. & Eswaran, H., 1988. Distribution, properties and classification of Vertisols. *Vertisols: Their distribution, properties, classification and management*, pp.1–22.

Dunbar, J. A., S. A. Amidu, and P. M. Allen., 2008, A Study of Seasonal Salinity Variation in Lake Whitney, Texas using Continuous Resistivity Profiling. In *Proceedings of SAGEEP*, Philadelphia.

Edwards, L.S., 1977. A modified pseudosection for resistivity and IP. *Geophysics*, 42(5), pp.1020–1036.

Fomel, S., 2001, *Three-dimensional seismic data regularization*. Stanford University, Stanford, California.

Gander, W., Golub, G.H. & Strebel, R., 1994. Least-squares fitting of circles and ellipses. *BIT Numerical Mathematics*, 34(4), pp.558–578.

Goto, T. N., Kasaya, T., Machiyama, H., Takagi, R., Matsumoto, R., Okuda, Y., Satoh, M., Watanabe, T., Seama, N., Mikada, H., Sanada, Y., Kinoshita, M., 2008, A marine deep-towed DC resistivity survey in a methane hydrate area, Japan Sea. *Exploration Geophysics*, 39(1), 52-59.

Guo, L., Meng, X., and Shi, L., 2012, Gridding aeromagnetic data using inverse interpolation. *Geophysical Journal International*, 189(3), 1352-1360.

Habberjam, G.M. & Watkins, G.E., 1967. The use of a square configuration in resistivity prospecting. *Geophysical prospecting*, 15(3), pp.445–467.

Habberjam, G.M., 1972. The Effects of Anisotropy on Square Array Resistivity Measurements. *Geophysical prospecting*, 20(2), pp.249–266.

Hart, D. & Rudman, A.J., 1997. Least-squares fit of an ellipse to anisotropic polar data: Application to azimuthal resistivity surveys in karst regions. *Computers & Geosciences*, 23(2), pp.189–194.

Jerri, A. J., 1977, The Shannon sampling theorem—Its various extensions and applications: A tutorial review. *Proceedings of the IEEE*, 65(11), 1565-1596.

Keller, G.V. & Frischknecht, F.C., 1966. Electrical methods in geophysical prospecting.

Krige, D. G., 1951, *A statistical approach to some mine valuation and allied problems on the Witwatersrand*, University of the Witwatersrand, South Africa.

LaBrecque, D. J., and X. Yang, 2001, Difference inversion of ERT data: A fast inversion method for 3-D in situ monitoring. *Journal of Environmental and Engineering Geophysics*, 6, no. 2

Lam, N. S. N., 1983, Spatial interpolation methods: a review. *Cartography and Geographic Information Science,* 10(2), 129-150.

Lane, J.W., Haeni, F.P. & Watson, W.M., 1995. Use of a Square-Array Direct-Current Resistivity Method to Detect Fractures in Crystalline Bedrock in New Hampshire. *Ground Water*, 33(3), pp.476–485.

Leonard-Mayer, P.J., 1984. *A surface resistivity method for measuring hydrologic characteristics of jointed formations*, US Dept. of the Interior, Bureau of Mines.

Li, X., and Goetze, H.J., 1999, Comparison of some gridding methods. *The Leading Edge*, 18(8), 898-900.

Li, Y., and Spitzer, K., 2002, Three-dimensional DC resistivity forward modeling using finite elements in comparison with finite-difference solutions. *Geophysical Journal International*, 151(3), 924-934.

Loke, M. H., and Barker, R. D., 1996, Practical techniques for 3D resistivity surveys and data inversion. *Geophysical Prospecting*, 44(3), 499-523.

Macelloni, L., A. Simonetti, J. H. Knapp, C. C. Knapp, C. B. Lutken, and L. L. Lapham, 2012, Multiple resolution seismic imaging of a shallow hydrocarbon plumbing system, Woolsey Mound, northern Gulf of Mexico. *Marine and Petroleum Geology*, 38, no. 1, 128–142

Matheron, G., 1971, *The theory of regionalized variables and its applications*. École national supérieure des mines, 211.

Miller, G.B. & Greenwade, J.M., 2001. Soil Survey of McLennan County, Texas.

Mitas, L., and Mitasova, H., 1999. Spatial interpolation, *Geographical Information Systems: Principles, Techniques, Management and Applications, vol. 1*., Wiley, London, 481– 492.

Nyquist, J. E., Freyer, P. A., and Toran, L., 2008, Stream bottom resistivity tomography to map ground water discharge, *Groundwater*, 46(4), 561-569.

Pidlisecky, A., Haber, E., and Knight, R., 2007, RESINVM3D: A 3D resistivity inversion package. *Geophysics*, 72(2), H1-H10.

Ritzi, R.W. & Andolsek, R.H., 1992. Relation between anisotropic transmissivity and azimuthal resistivity surveys in shallow, fractured, carbonate flow systems. *Ground Water*, 30(5), pp.774–780.

Roy, K. K., 2008, *Potential theory in applied geophysics*. Springer.

Rucker, D. F., Levitt, M. T., and Greenwood, W. J., 2009, Three-dimensional electrical resistivity model of a nuclear waste disposal site. *Journal of Applied Geophysics*, 69(3), 150-164.

Rucker, D. F., Noonan, G. E., & Greenwood, W. J., 2011, Electrical resistivity in support of geological mapping along the Panama Canal. *Engineering Geology*, 117(1), 121-133.

Samouelian, A. et al., 2004. Three-dimensional crack monitoring by electrical resistivity measurement. *European Journal of Soil Science*, 55(4), pp.751–762.

Semenov, A.S., 1975. Rock anisotropy and electrical fields peculiarities in anisotropic media. *Vestnik of Leningrad university*, pp.40–47.

Serié, C., M. Huuse, and N. H. Schødt, 2012, Gas hydrate pingoes: Deep seafloor evidence of focused fluid flow on continental margins. *Geology*, 40, no. 3, 207–210,

Shepard, D., 1968, A two-dimensional interpolation function for irregularly-spaced data. *Proceedings of the 23rd ACM national conference*, 517-524.

Simonetti, A., J. H. Knapp, K. Sleeper, C. B. Lutken, L. Macelloni, and C. C. Knapp, 2013, Spatial distribution of gas hydrates from high-resolution seismic and core data, Woolsey Mound, northern Gulf of Mexico. *Marine and Petroleum Geology*, 44, 21–33

Snyder, D. D., and Wightman, E., 2002, Application of continuous resistivity profiling to aquifer characterization. In *Proceedings of the SAGEEP*, Las Vegas, Nevada

Spitzer, K., 1995, A 3-D finite-difference algorithm for DC resistivity modelling using conjugate gradient methods. *Geophysical Journal International*, 123(3), 903-914.

Taylor, R.W. & Fleming, A.H., 1988. Characterizing Jointed Systems by Azimuthal Resistivity Surveys. *Ground Water*, 26(4), pp.464–474.

Tomczak, M., 1998, Spatial interpolation and its uncertainty using automated anisotropic inverse distance weighting (IDW)-cross-validation/jackknife approach. *Journal of Geographic Information and Decision Analysis*, 2(2), 18-30.

Watson, D. F., and Philip, G. M., 1985, A refinement of inverse distance weighted interpolation. *Geo-Processing*, 4(2), 315-327.

Watson, K.A. & Barker, R.D., 1999. Differentiating anisotropy and lateral effects using azimuthal resistivity offset Wenner soundings. *Geophysics*, 64(3), pp.739–745.

Weisbrod, N. et al., 2009. Falling through the cracks: The role of fractures in Earth-atmosphere gas exchange. *Geophysical Research Letters*, 36(2), pp.1–5.

Xu, S., Y. Zhang, D. Pham, and G. Lambare, 2005, Antileakage Fourier transform for seismic data regularization. *Geophysics*, 70(4), 87-95.

Xu, T., & Dunbar, J. A., 2015. Binning Method for Mapping Irregularly Distributed Continuous Resistivity Profiling Data onto a Regular Grid for 3-D Inversion. *Journal of Environmental and Engineering Geophysics*, *20*(1), 1-17.

Xu, T., Dunbar, J., Gunnell, A., Lutken, C., Higley, P., & Lagmanson, M., 2015. Seafloor direct-current resistivity techniques for deep-marine, near-bottom gas-hydrate investigation. *The Leading Edge*, *34*(2), 180-188.

Zhang, J., Mackie, R. L., & Madden, T. R., 1995, 3-D resistivity forward modeling and inversion using conjugate gradients. *Geophysics*, 60(5), 1313-1325.